NIELS BOHR INSTITUTE
UNIVERSITY OF COPENHAGEN

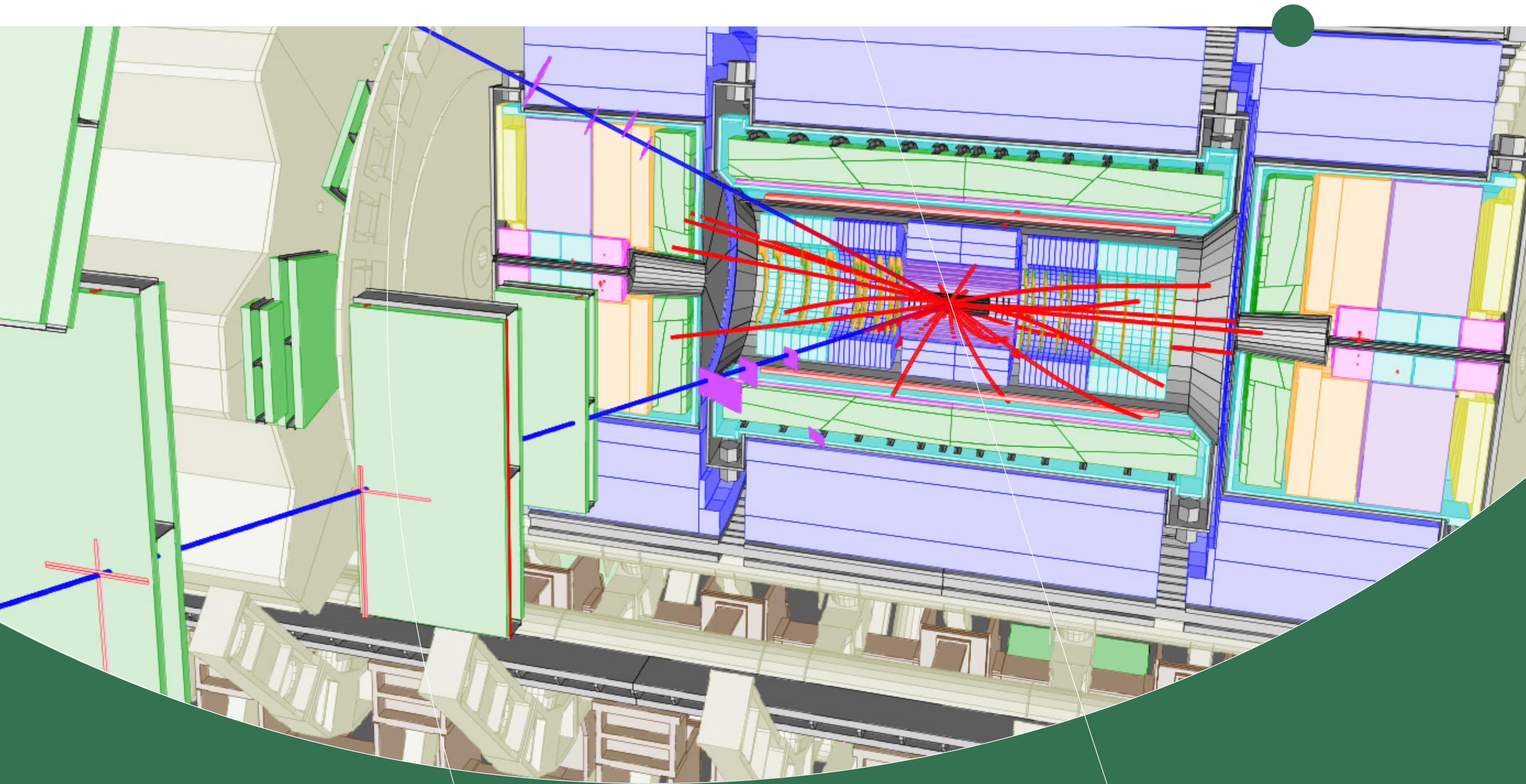

Search for long lived massive particles with the ATLAS detector at the LHC

Morten Dam Jørgensen

Master Thesis

Studies presented in this thesis are part of the following papers/notes:

- D. Casadei et al. *Search for Stable Hadronising Squarks and Gluinos at the ATLAS Experiment at the LHC*, CERN, Geneva, Dec 2010, Internal Note (ATL-COM-PHYS-2010-1065) [8].
- ATLAS Collaboration: G. Aad et al. *Search for Stable Hadronising Squarks and Gluinos at the ATLAS Experiment at the LHC*, Physics Letters B, Volume 701, Issue 1, 27 June 2011, Pages 1-19 [11].

Cover illustration: ATLAS Candidate Z Decay with Large Missing E_T.

To see a world in a grain of sand
And a heaven in a wild flower,
Hold infinity in the palm of your hand
And eternity in an hour.

— William Blake,
Auguries of Innocence, 1803

Contents

List of Figures

List of Tables

Preface

An invitation

Dear reader, let this first chapter serve as an invitation to a journey that began ages ago — a journey that stretches from the outermost reaches of human imagination, to the innermost foundation of the Universe itself. A journey of such magnitude, is not to be taken lightly, and the tools needed are not wielded with ease, but in the end the gain might outweigh the burden, only time will tell.

The dream of understanding what we see around us, must be as old as mankind itself. While the search for truth have taken many detours through the millennia, we seem to have arrived at a form of knowledge that at least reflect the world around us with less bias than ever before. Science, as we call this tradition of gathering knowledge, has evolved into a system where by limiting our reach to measurable phenomena we can predict how nature at its most fundamental levels will act. With this limitation in mind, one might say that the truly important questions in life can only go unasserted, but with advances in modern science, we are today taking bold steps towards answering questions, that the world's religions have been fighting over for millennia.

Our journey starts in what is now the present. During the early winter of 2009, a giant machine located deep below the ground in the suburbs of Geneva, began its operation — creating cataclysmic collisions of matter. The goal of this machine is to probe the Universe at energies high enough to recreate events similar to those that happened at the time of the Big Bang.

The possible implications of the knowledge resulting from this experiment is truly profound, we might find that space have more than three dimensions, or why matter is more abundant than its counterpart; anti-matter or perhaps that symmetries in the laws of the Universe is more than just a coincidence but the governing principle of all forces and matter. The Large Hadron Collider, as this machine is called is possibly the largest machine built by humanity, and certainly the most complex. The branch of science dealing with these subjects is called elementary particle physics, it investigates energy, matter and forces – and how these relate to each other.

The study of particle physics is the search for the final answer, the final theory, a theoretical model that confines everything we know about the Universe at its deepest level, into one single idea. As of today, we are still far away from this goal. The theories in use are but approximations stitched together over the last century to try and give a coherent glimpse of what might be out there. Hopefully the Large Hadron Collider will help shed light on the bigger picture in years to come.

With the Large Hadron Collider as a looking glass, this work aims to discover new physics by searching for a type of long lived particle, that perhaps could change the way we understand the Universe and it's creation. The search for this new type of particle requires special detection methods as they behave in other ways than the known particles, methods, some of which will be developed in this thesis.

Elementary particle physics

Our understanding of what comprises the material seen around us, have evolved rapidly during the last hundred years. The discovery of electrons in 1897 by J. J. Thomson and the proton in 1919 by E. Rutherford was followed by the discovery of the neutron and few years later the Muon. During the 1960-70 a whole 'zoo' of particles was discovered, and the theories currently accepted where developed.

To understand particle physics, one must combine two great ideas of the twentieth century; Einstein's theory of Special Relativity and Quantum Mechanics pioneered by many, among others Niels Bohr and Werner Heisenberg.

The theory of Special Relativity concerns objects moving at velocities close to light speed and energies many times more than that which is bound in the masses of these objects. Quantum Mechanics on the other hand describes the world at the atomic level. When dimensions approach a certain size, the physical description changes, objects cannot be described in terms of precise locations or momenta, instead one must use a statistical definition where probability determines where a particle can be, or when. This combined idea of Relativity and Quantum Mechanics has come to be called Quantum Field Theory and basically describes the elements of the universe as fundamental fields that resonates to create the particles we see around us. With Quantum Field Theory, as a mathematical framework, the currently known particles and how they interact with each other can be modelled. The accepted description of particle physics is called the 'Standard Model', it is comprised of 12 types of matter particles called 'fermions' and 13 kinds of force particles, known as 'bosons'. Of all these particles, only one piece is missing; the 'Higgs' boson, responsible for generating the masses of the other particles. One crucial omission from the known physics of our universe is gravity. The gravitational interactions of matter particles in large groupings, as we find in on the macroscopic scale is simply lacking from the Standard Model. As the ultimate ambition of particle physics is the total unification of all forces and matter into one unified theory, the Standard Model simply fail. This limitation have induced an enormous production of theoretical models, squarely aimed at replacing the Standard Model and its gravitational counter part, the general theory of relativity.

Supersymmetry

Since the Standard Model cannot be the final theory of everything, we seek evidence of new theories, that might supplant it. One of these theories is called 'Supersymmetry'. It proposes a symmetry between matter and force particles in the sense that fermion matter particles and the force carrying bosons each have a counter part of the opposite type. For this theory to work, every particle in the Standard Model must have a 'super partner' - a sort of counter-particle; a force carrying particle's super partner must be a matter particle and vice versa. The super-symmetrical idea has certain ensnaring beauties, but it has yet to be discovered. If Supersymmetry exist it must be what is called a broken symmetry, broken in such a way that the masses of the supersymmetric particles must be much higher than those

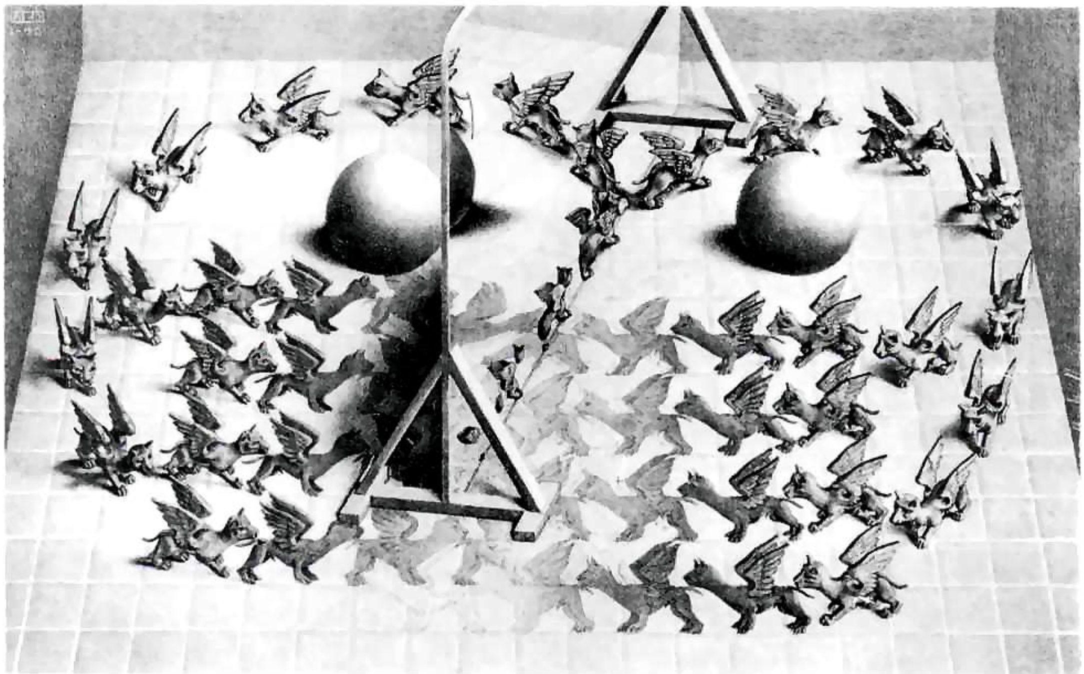

Figure 1: The Universe seem governed by symmetry (Escher's Magical Mirror).

of the Standard Model. The idea of superpartners, enables the unification of the electoweak and the strong nuclear forces, into a super force. This kind of unification is a major motivation for any kind of science as it uncovers a deeper connection between two previously thought disjunct areas of knowledge. The drive for unification have also led to even more ambitious ventures, namely the search for a final 'theory of everything', encompassing all forces of nature, including gravity. Supersymmetry in its original form does not automatically imply a connection with gravity, but most of these all encompassing theories requires supersymmetry in some form.

The new particles introduced by Supersymmetry and other theories should be confined by the current knowledge of their ordinary Standard Model partners. Certain properties of the Standard Model particles, such as lepton and baryon conservation would unlikely change dramatically. If that was not the case, protons would rapidly decay, causing widespread panic for a very very short while. A theoretical construction called 'R-parity' is introduced to stabilise the Standard Model particles, while allowing for supersymmetry. R-parity in turn lead to new stable supersymmetric particles, or at least one, the lightest supersymmetric partner of any Standard Model particle. The 'LSP' could be the much sought after 'Dark Matter' particle, if only one exists, as it would be massive and stable and potentially weakly interacting.

The title of this thesis is the search for long lived massive particles, and as such the lightest supersymmetric partner qualifies, but while profoundly interesting, it is another type of object related to R-parity that is the main focus in this work, the 'coloured' R-Hadron.

R-Hadrons: a model for Long lived massive particles

Some incarnations of Supersymmetry splits the masses of the super-symmetric particles into two groupings, a lighter set consisting of the boson's super partners and a heavier set with the fermion's super partners. In such a model the decay of a light particle through a heavy one is unlikely (but not impossible), the low probability of such an event to occur leaves the light particle meta-stable. If these meta-stable particles are affected by the strong nuclear force and thus carries colour, they would hadronise by binding with Standard Model quarks into colour neutral composite particles. The quarks bound with a supersymmetric particle would be stable as they are sustained 'colour' conservation with the supersymmetric particle. With a stable quark system, and a long lived superpartner, the composite itself could be long lived. This construction is called an 'R-Hadron'. While inspired by supersymmetric R-parity, this construction is necessarily true for any new theory predicting long lived coloured particles, not just Supersymmetry. So while Supersymmetry is the motivating model for this work, it should be considered a general search for new heavy long lived coloured objects.

The Large Hadron Collider

Experimental particle physics is 'big science', not many single nations could afford to build the needed machinery alone, and none possesses the human resources. Particle physics is an international collaborative effort between many nations and thousands of scientists and engineers. Currently the common playground for particle physicists is CERN with its enormous accelerator, the 'Large Hadron Collider', being commissioned as I write this. Hadron colliders are synonymous with discovery machines, as they can achieve peak collision energies much higher than lepton colliders, but in general with a larger uncertainty on the interaction energy, making them unsuitable for precision measurements. With the Large Hadron Collider there is a great hope that we might discover new physics, perhaps even supersymmetry. During the first year of data gathering $\mathcal{L} \sim 50\,\mathrm{pb}^{-1}$ of data have been accumulated. While this is an insignificant amount compared to the nominal $\mathcal{L} \sim 100$ (fb year)$^{-1}$ it is still an amazing achievement for the first year of running. Even with the moderate amount of data available, it is possible to impose limits on the theoretical expectations of many models. The result of this thesis is placing such limitations on predictions of the masses of long lived massive particles with some of the recorded data.

The author's contribution

Parts of the work represented in thesis is used in a common search for R-Hadrons at the ATLAS experiment. The overall thesis work consists of the following points, whereas the parts contributed to the main analysis are listed in the conclusion in chapter 10.

1. Development of calorimeter based dE/dx observables for R-Hadron searches in the ATLAS software framework called ATHENA (chapter 7).

2. Development of a mass estimation technique for dE/dx observables (chapter 8).

3. Application of the mass estimation technique on pixel and calorimeter dE/dx measurements (chapter 8.2).

4. R-Hadron analysis based on these and other observables (chapter 9).

5. Placing an upper limit on R-Hadron production at $\sqrt{s} = 7$ TeV with 15.3 pb^{-1} of data (chapter 9.6).

Acknowledgements

The work presented in this thesis not just represent the result of one year of study, but also the accumulated knowledge and experience by being around many friendly and inspiring people. I joined the experimental particle physics group at the Niels Bohr Institute not long after my defection to Zealand as an undergraduate student, and couldn't help but being taken by the friendly atmosphere in the group. Since then I have learned much and have most of the group to thank, but especially Jørgen Beck Hansen, my advisor in war and Jørn Dines Hansen my advisor in peace have been more than just good mentors, but also wonderful friends. It is Rasmus Mackeprang who introduced me to R-Hadrons, though we hadn't much time to get to know each other, as he had just returned from his fellowship at CERN when I went down there for hands-on training. I spent the first five months of my thesis year at CERN where I met many from the ATLAS team searching for R-Hadrons. Especially David Milstead and Christian Ohm whom I have enjoyed working with greatly deserves thanks for their incredible patience with the 'master student'. Being deeply involved with the ATLAS SMP group also meant getting to know other members of the NBI team better. When I returned to Denmark, both Troels Petersen and Esben Klinkby had joined the ranks, not to mention the second floor of the M-building. The transformative force did not go unnoticed and I have been very fond of the energetic climate at our floor. Troels deserves a second mentioning as we have frequently discussed the subtleness of statistics and why errors in quadrature is a wonderful thing, so I humbly declare you my advisor in matters of numbers, and conclude my acknowledgements with a big thanks to Anders, Björn, Daniel, Frederik, Hans-Henrik, Ingrid, Johan, John, Kristian, Lotte, Martin, Mogens, Morten, Pavel, Peter, Peter, Peter, Sascha, Silvia, Simon, Stefania, Sune, Troels, Ursula and to the rest of the group I have greatly appreciated being part of this for the last few years, and hope that where ever life takes me, the next many years will be just as exciting!

References

See the following references [38], [16], [22] [20] for in-depth information about the topics mentioned in this introduction.

Part I

Theory

1

The Standard Model

The Standard Model (SM) of particle physics is by all measures an eminently successful theory. It has survived in its current form for nearly 40 years. Its ample predictions have been verified, including the existence of the $W^{\pm}$ and the Z^0 bosons, as well as the charm and top quark. Indeed; the Standard Model does not fail due to wrong predictions, but rather to the lack of phenomenological coverage. Neutrino oscillations discovered recently are leading to the conclusion that neutrinos cannot be massless, as originally constructed into the Standard Model. Of the major predictions in the Standard Model, only the observation of the Higgs boson is truly lacking.

In section 1.4 I will describe the phenomena a more encompassing model should include, currently missing from the Standard Model. In chapter 2 an introduction to a candidate theory will be given, followed by section 2.3 where long lived massive particles will be motivated, concluding with their common phenomenology.

1.1 Quantum Field Theory

The mathematical framework used in designing the Standard Model of particle physics, is called Quantum Field Theory (QFT). It is the unification of the concepts of Quantum Mechanics and the special theory of relativity. The phenomenological reach of such theories is mostly very small length and time scales and interactions involving high energies. QFT's are modelled using Lagrangian density functions. I will give no attempt at explaining the mathematical structure of the Standard Model as it is beyond the scope of this thesis, and only motivate the basic concepts enabling a comparison between the Standard Model itself and the new theories exemplified later in this chapter.

1.2 Symmetries

The concept of gauge invariance is of crucial importance in the description of forces in Nature. For a given Lagrangian description of a system, gauge invariance implies that the Lagrangian density is conserved under local symmetry transformations. This translates into requiring no 'preferred' frame of reference, in which the theory is viable. Most field theories (including the constituents of the SM) are from the onset constructed to be Lorentz invariant, meaning that they remain true under Lorentzian transformations.

[0]Natural units are assumed throughout the thesis: $\hbar = c = k_B = G = 1$, implying: mass = momentum = energy = GeV.

	Mass (GeV)	Electric charge	Weak isospin, I_z	Colour
Quarks				
u	5×10^{-3}	$+\frac{2}{3}$	$+\frac{1}{2}$	3
d	10×10^{-3}	$-\frac{1}{3}$	$-\frac{1}{2}$	3
c	1.5	$+\frac{2}{3}$	$+\frac{1}{2}$	3
s	0.2	$-\frac{1}{3}$	$-\frac{1}{2}$	3
t	172	$+\frac{2}{3}$	$+\frac{1}{2}$	3
b	4.7	$-\frac{1}{3}$	$-\frac{1}{2}$	3
Leptons				
ν_e	$< 2.2 \times 10^{-9}$	0	$+\frac{1}{2}$	—
e	5.11×10^{-4}	-1	$-\frac{1}{2}$	—
ν_μ	$< 1.7 \times 10^{-4}$	0	$+\frac{1}{2}$	—
μ	0.106	-1	$-\frac{1}{2}$	—
ν_τ	< 0.0155	0	$+\frac{1}{2}$	—
τ	1.777	-1	$-\frac{1}{2}$	—

Table 1.1: The quarks and leptons of the Standard Model with quantum numbers. The quoted neutrino masses indicates the the current upper limits [16].

These symmetries are said to be *global*, as they should be the same at any point in the Universe. Any such symmetry corresponds to a conservation law[1], for instance if we require temporal translation (independence of time) invariance,

$$t \to t + \Delta t, \tag{1.1}$$

we get conservation of energy, where spatial translation invariance implies conservation of momentum.

In the Standard Model *local* gauge symmetries are imposed as well as the global symmetries. These stricter requirements, essentially imply that certain local (position dependent) transformations should leave all physical quantities conserved in the local space, apart from the globally preserved ones.

In mathematical terms, we call space-time the base-space $\mathcal{M}$. At every position in $\mathcal{M}$ we have a disjunct space called a fibre $\mathcal{V}$, all the fibres corresponding to the points in $\mathcal{M}$ are combined called a fibre-bundle $\mathcal{B}$. Symmetries defined on the base space $\mathcal{M}$ are global, and symmetries defined on the fibres in the bundle $\mathcal{B}$ are called local. A local symmetry is thus some operation done on a single instance in space-time that leaves the internal structure of that instance unperturbed.

The gauge symmetries constituting the Standard Model can be formulated by the symmetry group,

$$\mathrm{SU}(3) \times \mathrm{SU}(2) \times \mathrm{U}(1) \tag{1.2}$$

with each part outlined in the next section.

[1]**Noether's theorem** In the Lagrangian formulation, we find that every symmetry in a system corresponds to a conservation law, by applying Noether's theorem, discovered by Emma Noether in 1915.

	Mass (GeV)	spin	Electric charge	Colour
Electroweak				
γ	0	1	0	—
Z^0	91.2	1	0	—
W^+	80.4	1	+1	—
W^-	80.4	1	−1	—
QCD				
g	0	1	0	8
Higgs (unobserved at the time of writing)				
H	?	0	0	—

Table 1.2: The fundamental interactions in the Standard Model.

1.3 Particles and Forces

The general idea behind the Standard Model is greatly inspired by Quantum Electrodynamics (QED) in that it is a renormalisable field theory with local symmetries where quantised gauge fields give rise to gauge bosons that mediates interactions between spin-half fermions, and gauge invariance is extended to encompass a larger set of charges and currents than just the electric case.

Two main classes of charges/symmetries exists, the eight strong charges, called ‘colour’ charges, and four electroweak charges, including the electric charge.

The first class is called Quantum Chromodynamics (QCD) and the latter is called the ElectroWeak theory (EW). QCD and EW are generated independently, but quarks possesses both colour and electroweak charges, and the theories are thus linked through the hadrons. In equation (1.2) QCD is the first part: SU(3) with its 8 generators. The EW part consists of the product of Quantum Electrodynamics U(1) with just one generator and the Weak interaction theory SU(2) with three generators.

All matter is defined by spin-half fermionic fields, where quarks, the constituents of protons, neutrons and other hadrons interacts both strongly and weakly, while the leptons (electrons, muons, tauons and their associated neutrinos ν_e, ν_μ, ν_τ) only interacts weakly. The Standard Model fermions and their properties are listed in table 1.1. The fermions comes in three families or generations with identical quantum numbers, but different masses. In each family we find three weakly charged doublets of quarks, each doublet with a unique colour charge. The family also contains a weakly charged but colourless doublet with one neutrino and a corresponding lepton.

We currently have no understanding of why exactly three families exists, but by measuring the Z^0 boson decay-width at high precision, the LEP experiments determined that a *light* fourth neutrino generation was excluded.

The force carriers mediating the interactions between the fermionic particles are represented by spin-1 particles: The photon γ, the weak force gauge bosons $W^{\pm}$, Z^0 and the eight gluons g, that mediates the strong force.

The photon and the gluons are all massless particles, due to complete conservation of their internal symmetry. The weak bosons on the other hand are quite massive ($m_{W^{\pm}} = 80.4$ GeV and $m_Z = 91.2$ GeV), this is explained in the Standard Model by spontaneous breaking of the weak gauge symmetry, due the the Higgs Mechanism. The Higgs Mechanism predicts the existence of at least one spin-0 boson — yet to be observed. The Higgs field is also responsible for giving mass to all the other massive particles, including itself. The Standard Model bosons are listed in table 1.2.

1.4 Shortcomings of the Standard Model

So far no experimental data from particle accelerators have been able to refute the Standard Model predictions, yet the model itself has proven unsatisfactory as a complete theory of particle physics, and even more so as a Theory of Everything (TOE). Many of the elements in the Standard Model are constructed 'ad-hoc' to account for observed phenomena; the number of particles, their quantum numbers and deeper problems such as the generation of charge quantisation and the generation of fermion masses. These problems underlie the goal of the theory, it is not constructed to provide a deeper philosophical description of particle physics, but rather to serve as a predictive phenomenological framework with which the observed properties of particle interactions and decays can be calculated. It can be discussed whether deeper reasoning should be pursued, but even as a phenomenological framework, it lacks an integrated description of recent observations, such as the aforementioned neutrino masses.

The unsatisfactory shortcomings of the Standard Model can be summarised into three main categories:

Unification

1. *The Hierarchy problem.* Why do we see the large difference between the Planck mass scale and the electroweak mass scale? The mass of the Higgs boson should be close to the Planck mass[2] due to radiative corrections, but also close to the W and Z masses. As the Higgs boson is a scalar particle we would expect quadratic divergences in the one-loop corrections, (rather than logarithmic divergences). Since we observe the Z and the W masses at around 10^2 GeV, we are forced to conclude that something is cancelling the radiative contributions at high energies to a very high precision. Given the quadratic nature of these terms, small variations would lead to large fluctuations, it seems unnatural that something at high energy is perfectly aligned in such a way that it cancels such that we see the low Z and W masses. This is referred to as the *fine-tuning problem.*

2. *Unification.* The three forces described by the Standard Model gauge group (eq. 1.2) each have a coupling constant α_i. The size of each 'constant' is varying with the energy scale (and are thus said to be 'running'). The relative strength of these

[2]**Planck mass**: $m_p = \sqrt{\hbar c/G} = 10^{19}$ GeV

constants seems to be converging at high energies ($\sim 10^{15}$ GeV)[3], but not quite (fig. 1.1).

3. A description of *Gravity* is lacking from the Standard Model. The 'final' theory of everything should account for gravity as well as all the other forces.

4. *Dark matter.* Astronomical observations indicates that the matter flow in the Universe is not fully accounted for by Gravity alone, it looks like there is more matter in the Universe than directly observed. Currently no cosmological model agrees with Standard Model particles alone.

Flavour

1. *The problem of Flavour.* Why are there exactly three generations of quarks and leptons? As mentioned in section 1.3; LEP showed that the number of light neutrinos could only be three.

2. *The electric charge quanta.* Why are quarks charges 1/3's of the lepton charges?

Mass

1. The *fermion masses* are an ad-hoc addition to the Standard Model. The masses, and the *mass-hierarchy* between each generation is not understood, a new theory generating these masses from a fundamental condition would yield a more complete model.

2. *Neutrino masses.* As mentioned previously; the existence of non-zero neutrino masses is discovered recently, and was originally not added to the Standard Model. Neutrino oscillations, responsible for the mass differences have been added to the Standard Model, but at the cost of numerous new parameters and no new-won predictive power.

These and other dysfunctions of the current model have prompted the development of many new theories, where some (if not all) of the above problems have been remedied. Currently no new theory have proven more correct than the Standard Model, and some of the most promising (i.e. Superstring theory, Loop Quantum Gravity) are still untestable at the energies currently available at the worlds particle accelerators. As this thesis focuses on physics at the LHC, I will only be discussing theories testable at the low-TeV scale.

[3]**Unification scale.** The energies required for unification are equivalent to those at 10^{-39} seconds after Big Bang, where the temperature was about 10^{28} K [38].

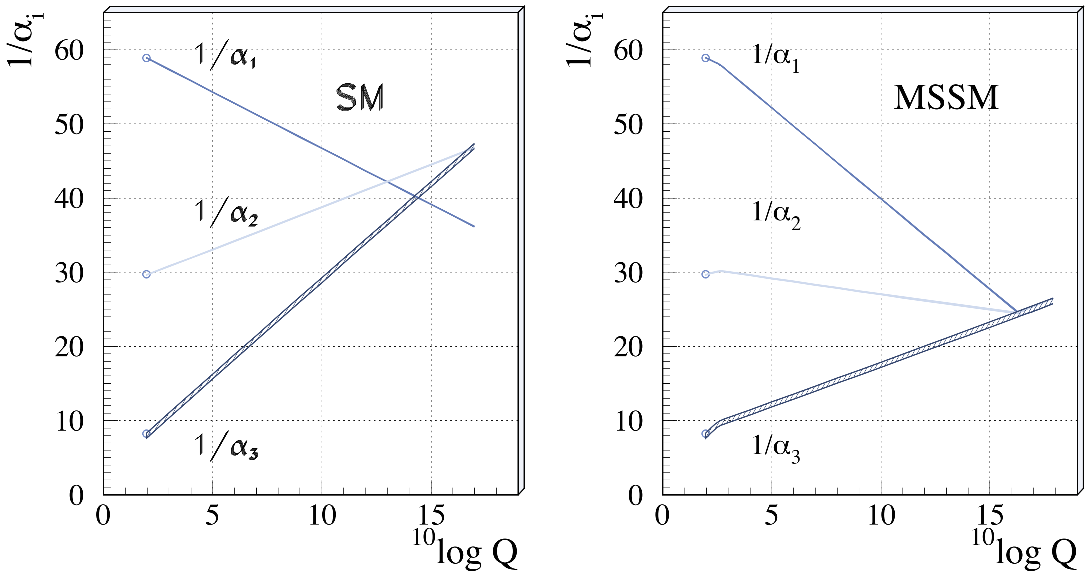

Figure 1.1: The running coupling constants. $\alpha_i, (i = 1, 2, 3)$ represents EM, Weak and Strong couplings respectively. The Standard model couplings (left) converges but do not seem meet and unify at the same point. In supersymmetry (right, MSSM in this example, see chapter 2.2) it is expected that the three couplings merge at some energy defining the SUSY scale [26].

Force	Carrier	Relative strength (at $10^{-15}m$)	Range
Strong force	g	1	$10^{-15}m$
Electromagnetic	γ	10^{-2}	long range
Weak force	$W^{\pm},\ Z_0$	10^{-13}	$<\ 10^{-18}m$
Gravitational	Space time geometry	10^{-38}	infinite

Table 1.3: The relative strength of the fundamental forces.

2

Theories beyond the Standard Model

The popular description of high energy physics is that as the energy increases we move closer to the starting point of the universe in terms of energy-density. An observation in that regard is that physics seems to simplify as we get closer to t_0. The electro-weak unification is such a phenomenon, where at high energy electro-magnetism and the weak force unifies into a single super-force. The complication is that in reality, we observe two distinct forces, at the energy scale observed in our everyday life. So the overall symmetry must be broken by some mechanism (leading to the construction of the Higgs mechanism by spontaneous symmetry breaking).

Historically the physical understanding of the Universe have entered into a new 'era' at every unification of two major ideas (fig. 2.1); the earthly and the heavenly movements [27, 37], the electric and the magnetic forces [35], space, time, matter and energy [14] and the weak forces and electromagnetism [43]. Given these past successes, the next step would be the unification of the strong and the weak forces intro a Grand Unified Theory (GUT), and lastly the unification of all forces, including gravity, into a Theory of Everything (TOE).

While no such unification is guaranteed to be possible, it is nevertheless an idea of some 'beauty' in the mathematical sense, and it seems only reasonable to assume that if we observe a system at an advanced evolutionary stage[1], it should simplify asymptotically the further back in time we observe. If the Universe would fold back into a simple state with one 'proto-force' as the initial condition, the physical intuition of many theorists would be well founded.

2.1 The Hierarchy problem revisited

In the quest for unification, the hierarchy problem constitutes a barrier on the Standard Model description, it has therefore motivated many new theories, which can be divided into three overall themes:

1. One solution to the hierarchy problem is found in *supersymmetrical* models, where the Standard Model fermions receives a boson 'super'-partner, and the bosons receives a fermionic partner. In such a model the quadratic fermion loops would cancel the scalar loop divergences [26].

[1]The Universe have been 'evolving' over roughly 4.32×10^{17} seconds, and the unification between the electromagnetic and the weak force broke after only 10^{-12} seconds.

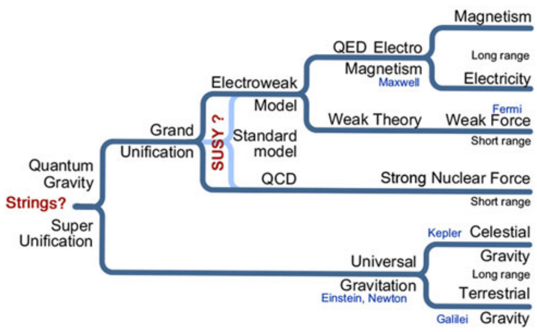

Figure 2.1: Unifications in physics.

Field Content of the MSSM					
Super-Multiplets	Boson Fields	Fermionic Partners	SU(3)	SU(2)	U(1)
gluon/gluino	g	$\widetilde{g}$	8	1	0
gauge/	$W^{\pm}, W^0$	$\widetilde{W}^{\pm}, \widetilde{W}^0$	1	3	0
gaugino	B	$\widetilde{B}$	1	1	0
slepton/	$(\widetilde{\nu}, \widetilde{e}^-)_L$	$(\nu, e^-)_L$	1	2	-1
lepton	$\tilde{e}^-_R$	e^-_R	1	1	-2
squark/	$(\widetilde{u}_L, \widetilde{d}_L)$	$(u, d)_L$	3	2	1/3
quark	$\widetilde{u}_R$	u_R	3	1	4/3
	$\widetilde{d}_R$	d_R	3	1	$-2/3$
Higgs/	(H^0_d, H^-_d)	$(\widetilde{H}^0_d, \widetilde{H}^-_d)$	1	2	-1
higgsino	(H^+_u, H^0_u)	$(\widetilde{H}^+_u, \widetilde{H}^0_u)$	1	2	1

Table 2.1: MSSM. All superpartners are marked by a tilde (source [16, p. 1293]).

2. Another solution could be to require a *composite Higgs particle* [20], where the substructure is defined at a new mass scale Λ. Any virtual process coupling to the Higgs boson would in that case be unable to have a virtual momentum above Λ. At energies above Λ the Higgs particle would then be described by it constituents. If $\Lambda \leq \mathcal{O}(1\text{ TeV})$ we would have agreement with the observed Z and W masses.

3. A recent development [2] solves the hierarchy problem by introducing *extra spatial dimensions*. By allowing gravity to propagate in more than $3+1$ dimensions, the Planck scale would move down, and at the right number of extra (finite sized) dimensions the Planck scale would approach the observed electro-weak scale.

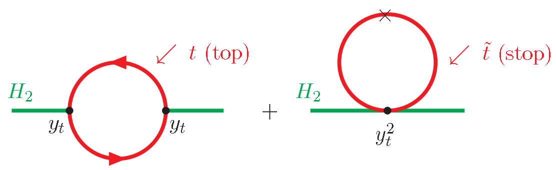

Figure 2.2: Higgs boson self-energy cancelation by particle-sparticle loops (illustrated by a top and stop loop).

2.2 Supersymmetry

A concept that promises to solve many of the problems mentioned in the previous section, especially the hierarchy problem, is called supersymmetry (SUSY). In the Standard Model, forces and matter particles are differentiated by their spin content. Forces carries integer spin, and obey Bose-statistics, while matter carries half-integer spin obey fermi-statistics. Supersymmetry breaks with this matter-force distinction by introducing a mirror-particle of opposite spin to each boson and fermion in the Standard Model.

Supersymmetry is the only non-trivial expansion of the Poincaré symmetry group[2], it is realised by introducing fermionic generators rather than the bosonic generators of the Standard Model [9]. A bosonic generator transforms a bosonic (fermionic) state into another bosonic (fermionic) state. A fermionic generator is on the contrary capable of changing the spin of a given state by 1/2, transforming a bosonic state into a fermionic state and vice versa,

$$
\begin{aligned}
Q|\text{boson}\rangle &= |\text{fermion}\rangle \\
Q|\text{fermion}\rangle &= |\text{boson}\rangle
\end{aligned}
$$

The consequences of the new supersymmetric algebra are quite profound, and well beyond the scope of this work, except for one central feature, the new fauna of particles.

With SUSY, every particle in the Standard Model will gain a ‘super-partner’. The quarks and leptons will have corresponding scalar partners; squarks and sleptons. The gauge bosons will have fermionic partners, gaugeinos, and the Higgs boson(s) will get fermionic higgsinos. The SUSY particles are summarised in table 2.1.

The masses and quantum numbers of the new ‘sparticles’ should be the same as their Standard Model partners, but no evidence of sparticles at the known Standard Model mass points have been found. Rather than abandoning SUSY, theorists have introduced the concept of ‘broken symmetries’, arguing that the mass scale of the supersymmetrical particles can be higher than their Standard Model counterparts, under certain circumstances.

As mentioned in section 2.1, SUSY is capable of cancelling the one-loop contributions to the Higgs by countering the quadratic terms. This is done by the introduced super-partner of a given particle as illustrated with the top quark in figure 2.2.

[2]Consisting of Lorentz transformations, translations and rotation.

Supersymmetrical extensions to the Standard Model

Supersymmetrical extensions of the Standard Model have been constructed in a variety of ways. One of the simpler schemes is called Minimal Supersymmetric Standard Model (MSSM) as it is the supersymmetrical representation of the Standard Model with the least amount of additional fields. More complicated models can be constructed, but MSSM is in general a popular choice as it simplifies the phenomenology to a manageable size.

Many of the working models being considered are derivatives of the MSSM, with various SUSY breaking schemes. The mechanisms behind the symmetry breaking can vary and I will refrain from deeper explanation (instead see [9]), except note that if SUSY is to solve the Hierarchy Problem, its breaking scale most be close to $\mathcal{O}(1\text{TeV})$.

R-parity

The new set of 'sparticles' having Standard Model charges, will lead to both lepton and baryon number violations. One consequence would be rapid proton decay. The current lower life-time limit for the proton is 6.6×10^{33} years [16], a clear indication that it is all but rapid if unstable at all. Many SUSY models construct a global symmetry called 'R-parity',

$$R = (-1)^{3B+L+2s} \tag{2.1}$$

where L is the lepton number, B is the baryon number and s is the particle spin. R will then be $+1$ for SM particles and -1 for SUSY sparticles.

R-parity conservation leads to at least one stable sparticle, namely the lightest of them all. In most SUSY scenarios the lightest super symmetric particle (LSP) is the lightest neutralino. The neutralino would be (largely) non-interacting as it traverses the detector, only detectable indirectly via momentum conservation.

2.3 Long Lived Coloured Massive Particles and split-supersymmetry

Many 'theories beyond the Standard Model', predict the existence of new long-lived massive particles (LLMP) beyond the LSP. Constructing full detector response models for

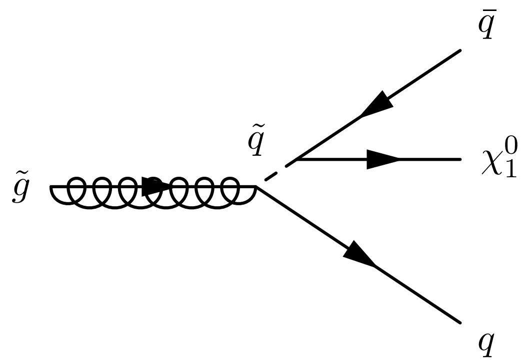

Figure 2.3: Gluino decay to χ_1^0 through a virtual squark.

	composition	notation
R-mesons	$R = \tilde{g}q\bar{q}, (\tilde{q}\bar{q})$	R^+, R^-, R^0
R-baryons	$R = \tilde{g}qqq, (\tilde{q}qq)$	R^{++}, R^+, R^-, R^0
R-gluinoballs	$R = \tilde{g}g$	R^0

Table 2.2: R-Hadrons. Gluino (squark) states. An exhaustive list of quark combinations can be found in [28, p. 60].

each hypothesis would be unfeasible. Rather than attempting a model-complete LLMP search, a representative 'probe' model have been chosen, the methodology described in later chapters can be applied to other models predicting electrically charged (and possibly coloured) long-lived massive particles with minor changes to the prior assumptions, but any such attempt will not be discussed further.

Split-supersymmetry

The specific scenario investigated is called *split-supersymmetry*, as it split the supersymmetry mass scale into a low and a high scale. The low scale containing gaugeinos and higgsinos and a (very) high scale ($m_S \gg 10$ TeV) supporting the scalar sfermion particles.

Because of the heavy sfermions, split-supersymmetry sacrifices MSSM's ability to cancel the quadratic corrections of the Higgs mass, and leaves the hierarchy problem to some other fine-tuning effect.

In the split-SUSY scenario the gluino can only decay meditated by a virtual squark, but given the large masses of the squarks, such a decay mode,

$$\tilde{g} \to \tilde{q}q \to q\bar{q}(q') + \chi_i^0(\chi_i^{\pm}) \tag{2.2}$$

is highly suppressed (see fig. 2.3). Even if the gluino is not the LSP, it will still be long-lived due this suppression.

Because of the high mass scale m_S in split-supersymmetry, the production of long-lived squarks is not (currently) possible at accelerators, but other scenarios predict the possibility of long-lived squarks, that could exhibit the same phenomenological features as long lived gluinos, namely colour charge.

R-Hadrons

Given the colour charge of gluinos (colour-octet C_8) and squarks (colour-triplet C_3), they will hadronise into bound states formed by the sparticle and a light quark system (LQS). Such composite states can be either electrically charged or neutral, given the quark composition [28]. These bound states are referred to as *R-Hadrons*, as the R-parity prevents direct decay to quarks or gluons, and the high mass scale suppresses the decay to squarks, keeping the bound state stabilised. The various bound states are noted in table 2.2. The term 'R-Hadron' is also commonly used to describe coloured massive particles with similar behaviour in non-SUSY models.

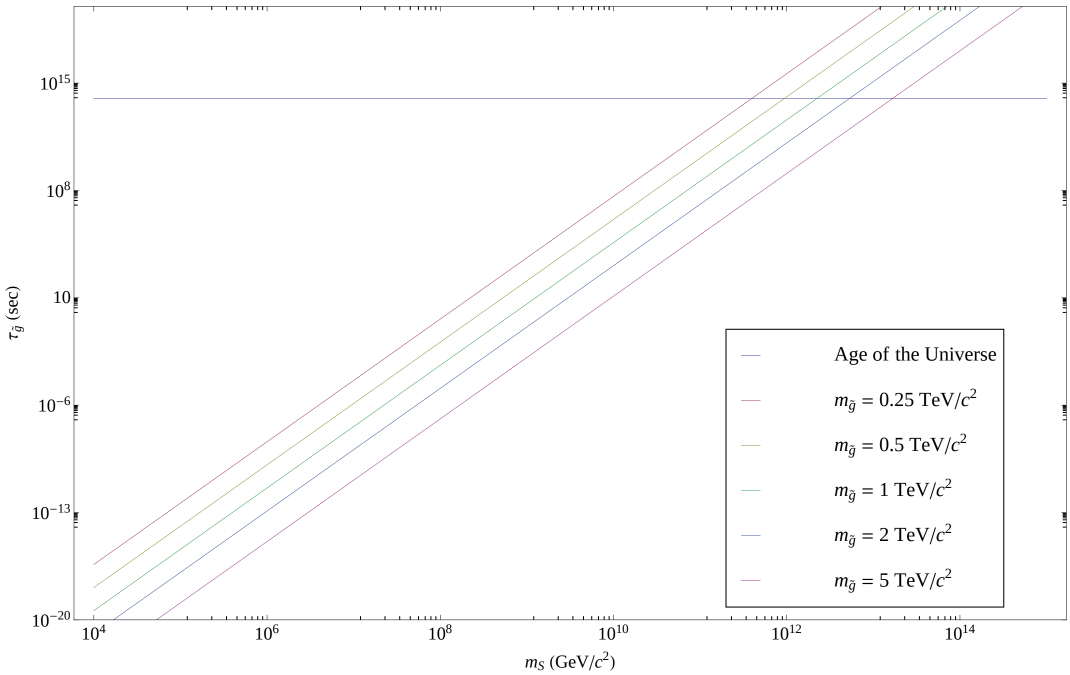

Figure 2.4: Lifetime of gluinos in Split-SUSY as a function of the mass scale m_S, described by equation 2.3.

The light quark system in R-Hadrons give rise to a rich set of interactions within the detector material, as both electromagnetic and nuclear interaction can occur, as will be described in the next chapters.

Cosmological implications and current limits

The lifetime of these long lived particles have potential implications for cosmology, as they would have been produced in the early universe. Depending on the lifetime, the relic long lived particles produced in the beginning of the universe would affect the mass-energy density, and hence the expansion of the universe as a whole. If the particles decayed after some relatively short time, it might contribute to unobserved changes to the cosmic microwave background.

The lifetime of gluinos in the split-supersymmetry model is largely dependent on the difference between the two mass scales. The lifetime can be approximated by [24],

$$\tau_{\tilde{g}} \approx 4 \times \left(\frac{m_S}{10^9 \text{ GeV}}\right)^4 \times \left(\frac{1 \text{ TeV}}{m_{\tilde{g}}}\right)^5 \text{ s.} \tag{2.3}$$

As illustrated in figure 2.4, the lifetime could be anything between picoseconds and the age of the universe.

While other types of long lived massive particles could be dark matter candidates, it is unlikely electrically or strongly charged objects such as R-Hadrons, based on cosmological arguments [18]. Also values of $m_S > 10^{12}$ GeV are ruled out as the decay of the gluinos would cause unobserved distortions in the CMB. Gluinos with short lifetimes will additionally cause nuclear synthesis of the light elements to be distorted. A rough constraint based on these arguments have been found, if $m_{\tilde{g}} < 300$ GeV then the high mass scale must be $m_S < 10^{12}$ GeV, and if $m_{\tilde{g}} > 300$ GeV then $m_S < 10^{10}$ GeV.

3

R-Hadron production at hadron colliders

The centre of mass energy at the LHC allow searches for LLMPs with masses in excess of several TeV. As the LHC is a hadron collider, the coloured gluinos could be produced in fair amounts (see fig. 3.4).

3.1 Parton distribution functions and physics at hadron colliders

Hadrons colliders like the LHC are complicated environments, as the colliding objects are nuclei rather than elementary particles, resembling more a bag of mixed objects than point particles. Figure 3.2 illustrate the interaction between two protons. i and j are the interacting partons, either gluons or quarks. $f_{i,j}(x_{1,2})$ are the Parton Density Functions (PDF) and x is the fraction of the hadron momentum,

$$x_{i,j} = \frac{P_{\text{parton}_{i,j}}}{P_{\text{hadron}}} \tag{3.1}$$

carried by the parton i, j. The effective energy available in a collision is then $\hat{E} = x_i x_j s$, where s is the centre of mass energy. The effective energy available to form new processes is thus always lower than the centre of mass energy in hadron colliders.

$\hat{\sigma}_{i,j}$ is the partonic cross section of the process we are interested in studying. The penetration into the nucleus requires the transverse momentum carried by the nuclei to be larger than the binding energy ($P_T \gg \Lambda_{QCD}$) [22]. In the collision, the partons inside the nuclei are considered 'free', in such a way that the cross section of interaction is defined as the probability of some constituent of one proton hitting some constituent in the other proton independently of the internal structure.

At the highly relativistic energies attainable at the LHC, the effective parton content is no longer dominated by the valance quarks in the proton ($p = u, u, d$) but also sea quarks and radiated gluons. The probability of observing a specific parton in the proton is described by the probability density function $f_i(x)$ where i is the specific parton. Parton density functions are parameterisations of experimental data, as QCD is not perturbatively calculable at this mass scale.

Numerous PDF models exist. The predominantly used is called CTEQ (The Coordinated Theoretical-Experimental Project on QCD) [36], in order to better understand the implications of a given PDF implementation on the theoretical prediction, a comparison with another model called MSTW (Martin-Stirling-Thorne-Watt Parton Distribution

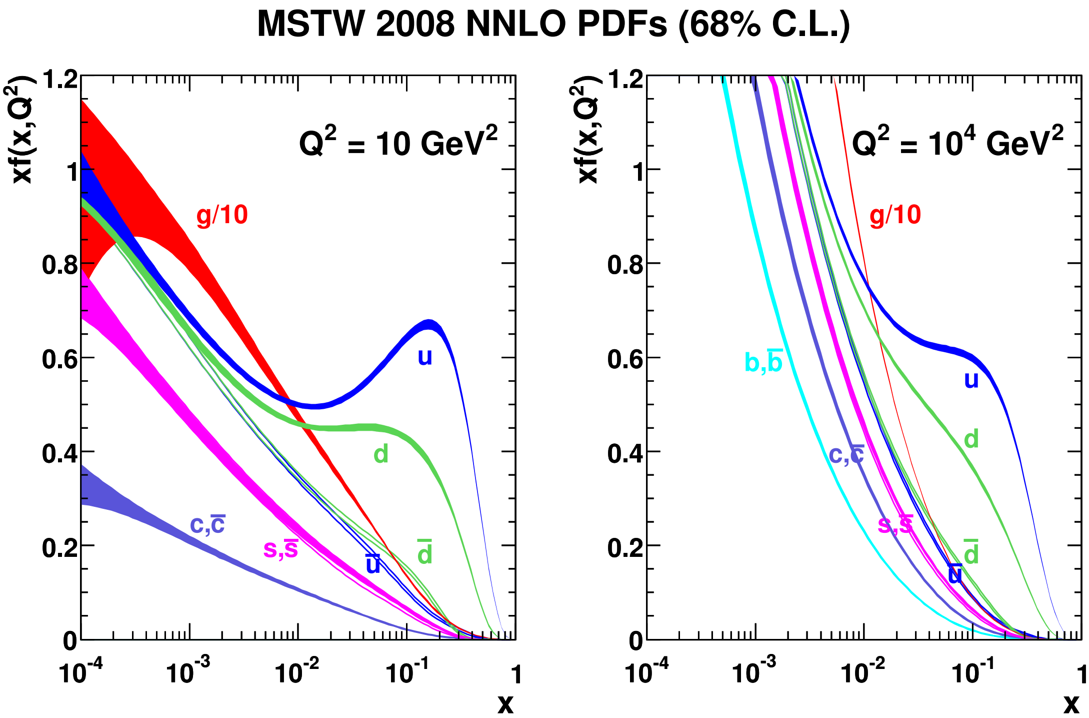

Figure 3.1: MSTW 2008 Parton Distribution Function.

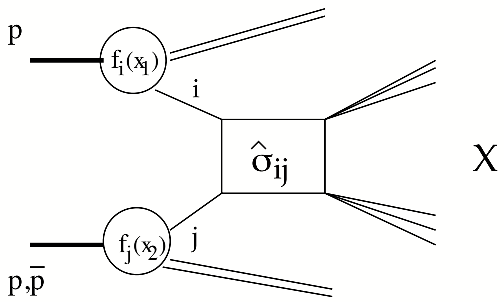

Figure 3.2: Parton interaction in proton-proton collisions.

Functions) [34] has been done as well. Both are used at Next-to-Leading Order (NLO) levels.

Because the constituent partons are free to interact during collisions, clean interactions of just one set of partons are seldom seen. There is always a high probability of additional interactions taking place, leading to Initial-State Radiation (ISR), polluting the event topology.

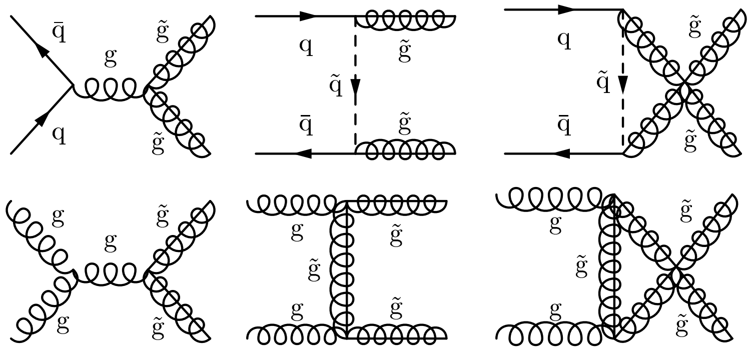

Figure 3.3: Gluino production at hadron colliders.

3.2 R-Hadron production

R-Hadrons will predominantly be produced in pairs at the LHC [18],

$$a + b \rightarrow X_c + X_d \tag{3.2}$$

where X_c and X_d could be a combination of new exotic states (i.e. gluinos and/or squarks). The production rate of these particles can be 'decoupled' from their decay-rates, by some suppression mechanism, like the split-SUSY example in section 2.3. This can lead to higher production rates than assumed for the currently known conservation laws.

In scenarios without R-parity single particle production might not be ruled out, but it must be extremely rare, as it production cross section is related to its decay width,

$$\sigma(a + b \rightarrow X) \propto \Gamma(X \rightarrow a + b) \tag{3.3}$$

If the particle is to survive throughout the detector while having a large mass, its production yield will be negligible.

At a hadron collider, the LO interactions leading to gluino states are,

$$q_i + \bar{q}_i \quad \rightarrow \quad \tilde{g} + \tilde{g} \tag{3.4}$$
$$g + g \quad \rightarrow \quad \tilde{g} + \tilde{g} \tag{3.5}$$

With the corresponding Feynman diagrams shown in fig. 3.3.

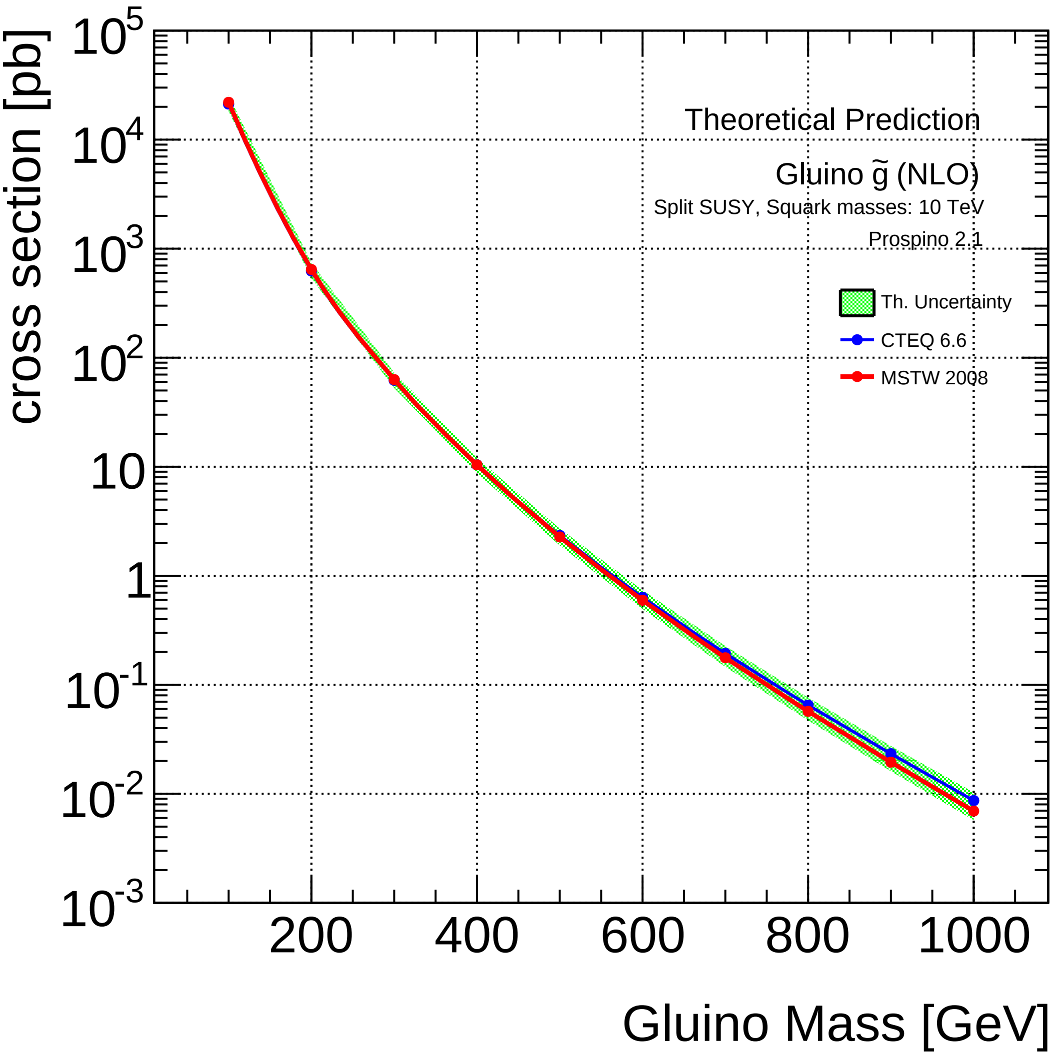

Figure 3.4: Cross sections for gluinos at various mass hypotheses between 100 GeV and 1000 GeV calculated with PROSPINO, utilising the MSTW 2008 and the CTEQ 6.6 PDFs.

3.3 Cross sections

A model-agnostic search for generic LLMPs is as mentioned in the preceding chapter the main motivation behind this analysis. In such a scenario we cannot compare with theory, only place an upper limit (or claim discovery of "something new") based on comparison between the expected background events, and the observed events. With a specific theory we are able to place exclusion limits as well, by comparing the observed data to both the expected background but also the expected signal. In the case of Split-SUSY, I have calculated the production cross sections for gluinos at current LHC energies ($\sqrt{s} = 7$ TeV) using PROSPINO [6]. The PROSPINO application is used to calculate NLO cross sections of supersymmetric particles at hadron colliders. Figure 3.4 show the cross sections for gluinos at various mass hypotheses between 100 GeV and 1000 GeV, where the high mass scale is set to $m_S = 10$ TeV. The use of NLO calculations in this scenario as opposed to leading order (LO), results in a slightly higher cross section estimate.

3.4 Event topologies

The basic assumption is that the event topology resembles two massive particles produced back-to-back. This is unlikely to be the full picture, as higher-order perturbative calculations allows for the inclusion of further partons doing collision,

$$a + b \to X_c + X_d + \text{additional partons} \tag{3.6}$$

Figure 3.5 illustrates the creation of initial-state radiation and final-state radiation (FSR). While both ISR and FSR is possible, FSR will be highly suppressed by the mass of the $X_{c,d}$ particles. ISR can pose a series of challenges to the analysis, as it allow for further jets in the event. These ISR induced jets eliminate the assumption that the transverse momenta of the two LLMPs is opposite. Another challenges arising from the additional jets, is 'noise' in the calorimeter, potentially affecting particle identification by the method described in later chapters.

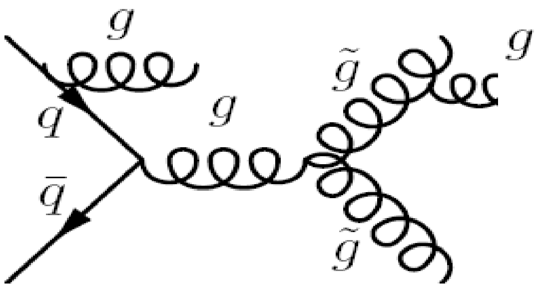

Figure 3.5: Initial and Final state radiation in gluino processes at hadron colliders.

3.5 Detection methods

The possibility of direct detection make searches for R-Hadrons distinct from other 'new physics' searches. Detectors at LHC and other colliders have been designed to discriminate standard model particles at the best possible resolution. Since R-Hadrons tend to be slow moving due to kinematic constraints, they distinguish themselves from other particles by not moving near light speed. Time of flight is thous an excellent method of observing R-Hadrons. Because the amount of ionisation as charged particles traverses matter, increases at low velocity, we also see a distinct energy deposition. Another characteristic effect is penetration. Like muons, R-Hadrons, because of their large energies are not expected to be stopped by the calorimeters, but propagate out of the detector. Lastly, nuclear interactions with the detector material can change the electric charge of the light quark system. Neutral R-Hadrons would cause a large amount of missing energy, but even R-Hadrons charged in some sub detectors and neutral in others will cause a distinct signature bot accounted for in the traditional detection scenario in ATLAS.

Environments like the LHC are built to sustain very high interaction rates, with detectors roughly 10 m in radius, and millions of collisions per second, the trigger system must be very fast. This is possible due to the assumption that particles always move very close to light speed[1]. Slow moving particles can potentially be difficult to trigger on, if they arrive out of time at the trigger stations, leaving the online reconstruction unable to match the trigger signal to the correct event. This is specifically a problem if the muon system is used for R-Hadron searches, as it is placed outermost and it takes 25 ns to reach the trigger station.

[1] Secondly by allowing events to overlap.

Part II

The Experiment

4

The Large Hadron Collider

The Large Hadron Collider (LHC) is a proton-proton collider located at CERN close to Geneva (Switzerland). The collider is placed in the old LEP tunnel, 26.7 km in circumference. The design energy of the LHC is 7 TeV per beam, and the nominal instantaneous luminosity is on the order of 10^{34} cm^{-2} s^{-1}. The LHC began operation in 2008, but due to an accident the first usable data where not delivered before november 2009, at 450 GeV beam energies. The proton run of 2010 ended in november, after accumulating roughly 45 pb^{-1} of integrated luminosity at a beam energy of 3.5 TeV. The search conducted in this thesis is based on a subset of the available 2010 data.

4.1 The CERN Facility

CERN is one of the largest laboratories dedicated to the study of fundamental science on the planet. It was conceived by the 'Conseil Européen pour la Recherche Nucléaire' (CERN) in the early fifties. The science conducted at CERN centres around the accelerator facilities that together forms an 'energy-ladder' delivering charged particles at energies ranging from 1.4GeV to 7TeV.

The LHC is the last part in a long chain of gradually more energetic accelerators (figure 4.1). During proton runs, hydrogen is ionised, than accelerated to 50 MeV by a linear accelerator (Linac 2[1]). The protons are then fed to the Proton Synchrotron Booster (PSB) accelerating the particles to 1.4 GeV. The particles are then injected into the Proton Synchrotron (PS) where they reach 25 GeV before ejection to the Super Proton Synchrotron (SPS), the second largest accelerator at CERN with a circumference of 6.9 km. The SPS accelerates the protons to 450 GeV before injection into the LHC. The remaining elements presented in figure 4.1 are related to other experiments, and heavy ion operation at the LHC.

4.2 The Large Hadron Collider

The LHC is a high energy, high luminosity collider, aimed at discovering new physics. The principal 'modus operandi' is delivering as high a luminosity as possible, expanding the statistical reach to very rare events, while delivering as high an energy as possible, enabling the production of rare physics at higher probability. Protons are selected as collision objects to enable both factors. The use of protons rather than electrons enables a higher

[1]Linac 4 is currently under construction and is planned to replace Linac 2 around 2013

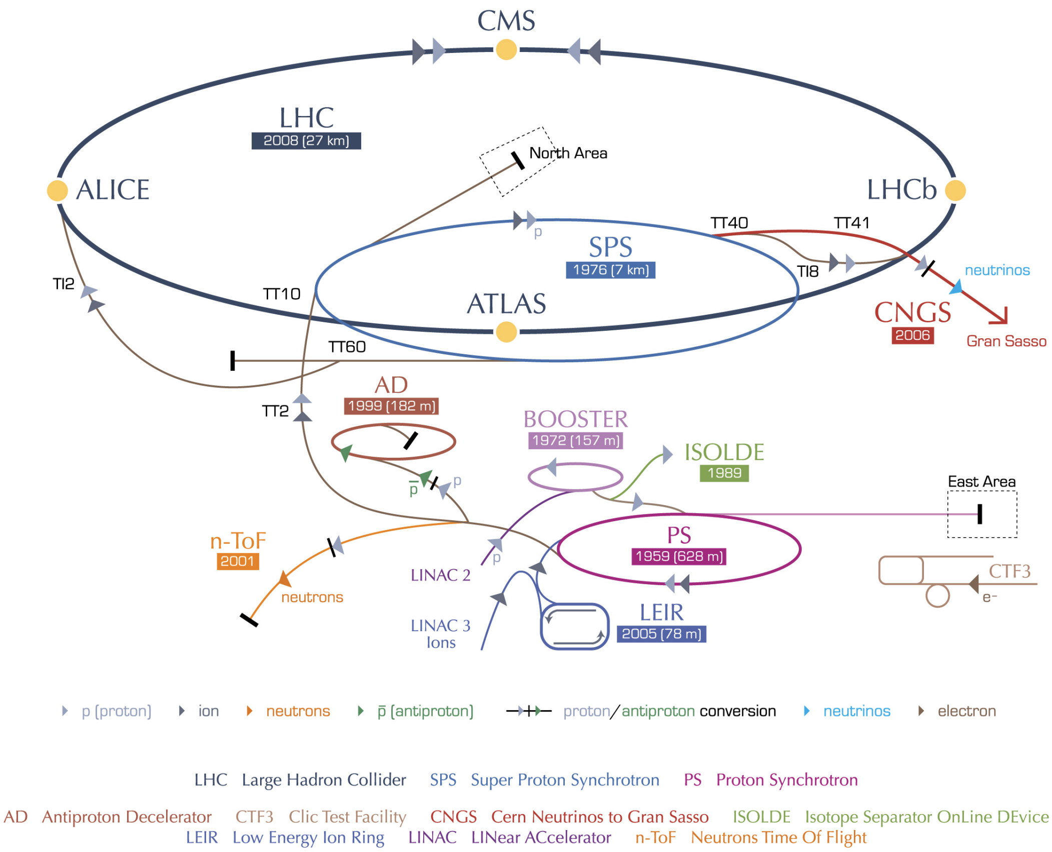

Figure 4.1: CERN Accelerator complex.

collision energy by avoiding large energy losses by synchrotron radiation. The choice of proton-proton instead of proton-anti-proton collisions is due to the limited production capability of anti-protons.

Architectural Overview

The LHC is built to fit into the preexisting LEP (Large Electron-Positron Collider) tunnel. The dimensions of the previous accelerator have been the primary limiting factor in the design of the LHC. The internal diameter of the LEP tunnel is 3.7 m, leaving little space for two separate proton rings. Instead the LHC is designed as a two-in-one accelerator where two beam pipes share a common cryostat.

The luminosity of a specific event type is given by,

$$N_{event} = L\sigma_{event}, \tag{4.1}$$

Where σ_{event} is the cross section of the specific event type and L is the machine luminosity. The luminosity is given by

$$L = \frac{N_b^2 n_b f_{rev} \gamma_r}{4\pi \epsilon_n \beta^*} F, \tag{4.2}$$

	Nominal	(late) 2010 Run
Bunch population	$N_b = 1.15 \times 10^{11}$	$N_b \geq 1.15 \times 10^{11}$
Colliding bunch pairs	$n_{bb} = 2808$	$n_{bb} = 348$
Number of bunches per beam	$n_b = 2808$	$n_b = 368$
Revolution frequency	$f_{rev} = 11245$ Hz	$f_{rev} = 11245$ Hz
Beam energy	$E = 7,000$ GeV	$3,500$ GeV
Beta function at collision	$\beta^* = 0.55$ m	$\beta^* = 3.5$ m
Normalised transverse emittance	$\epsilon_n = 3.75 \times 10^{-6}$ m	$\epsilon_n = 3.75 \times 10^{-6}$ m
Full crossing angle	$\alpha = 285$ μrad	$\alpha = 100$ μrad
Lorentz factor	$\gamma_r = 7463$	$\gamma_r = 3731$
Luminosity per bunch pair	$L_{bb} = 3.599 \times 10^{30}$ Hz/cm^2	$L_{bb} = 3.274 \times 10^{29}$ Hz/cm^2
Average number of processes per crossing	$\mu = 25.60$	$\mu = 2.33$
Luminosity (all bunches)	$L = 1.011 \times 10^{34}$ Hz/cm^2	$L = 1.139 \times 10^{32}$ Hz/cm^2
Stored beam energy	$E_{stored} = 361.7$ MJ	$E_{stored} = 23.5$ MJ

Table 4.1: LHC parameters at nominal operation and during the commissioning in 2010. (Ref. [17]).

where N_b is the number of particles per bunch, n_b is the number of bunches per beam, f_{rev} the revolution frequency, γ_r is the relativistic gamma factor, ϵ_n is the transverse beam emittance, $\beta*$ is the beta function at the collision point and F is is a geometrical reduction factor due to the introduced crossing angle at the interaction points.

The luminosity goal is $L = 10^{34}\text{cm}^{-2}\ \text{s}^{-1}$, with $n_b = 2808$ bunches of $N_b = 1.15 \times 10^{11}$ protons. The particle energy is mainly limited by the magnetic field of the bending solenoid keeping the beam in a circular orbit. The magnets can produce a magnetic dipole field of 8.33 T, required at a beam energy of 7 TeV. The specific parameters for LHC at at current and nominal operation is summarised in table 4.1.

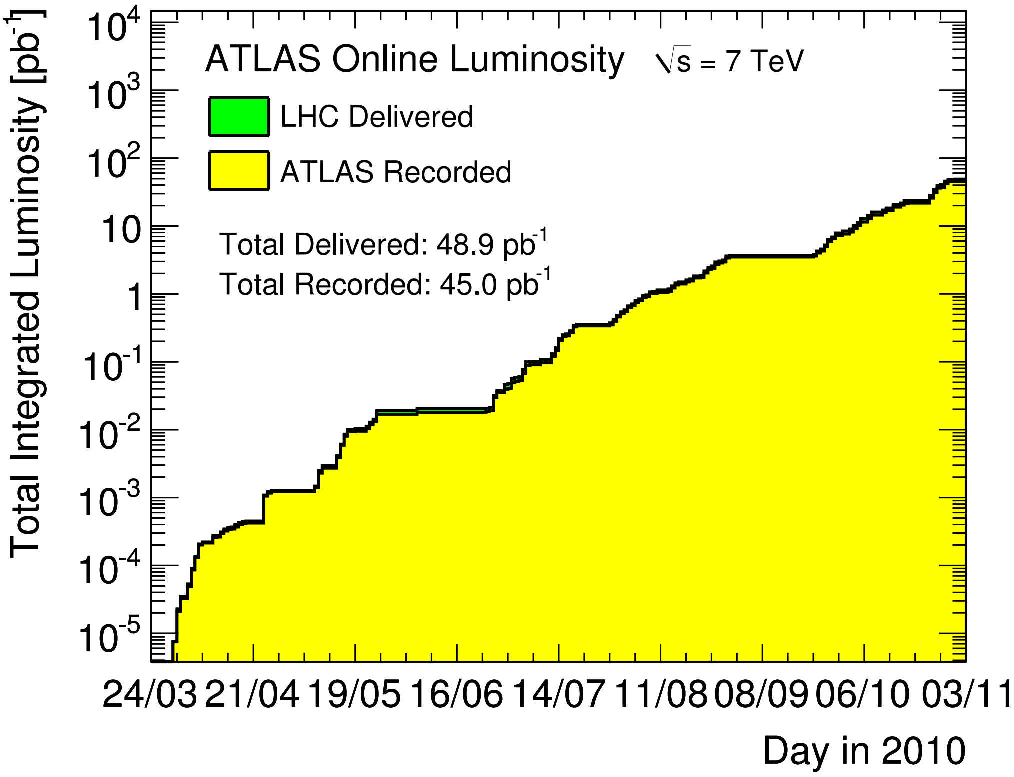

Figure 4.2: Integrated luminosity for the 2010 proton run, recorded by ATLAS.

5

The ATLAS experiment

ATLAS or 'A Toroidal LHC ApparatuS', is the name of a general purpose particle detector, constructed by a collaboration that currently numbers more than 3000 physicists from 38 countries to study a wide range of possible phenomena.

ATLAS together with its sister experiment CMS[1] are built to search for new physics at the energies available at the LHC. One of the driving design choices behind ATLAS is the search for the Higgs boson.

The minimal energy resolution, is designed to detect a narrow width of a low mass Higgs ($m_H < 2m_Z$). The LHC being a proton collider also puts specific requirements on the calorimeter systems, and the high production energies requires a strong magnetic field to bend the tracks of the resulting high-p_T particles, for momentum and charge measurements. The high luminosity of the LHC also puts strong bounds on the restitution rate of the detectors. At nominal luminosity roughly 10^9 inelastic collisions take place per second. Separating overlapping events, also requires good tracking. As mentioned in the earlier chapters, a likely SUSY signature will be missing energy (E_T^{miss}) from a weakly interacting LSP. Extensive coverage of the calorimeter systems are thus needed in order to provide a precise estimate of the missing energy from neutrinos or new types of particles escaping the detector undetected. The physical dimensions of the detector is motivated by the collision energies, as more material is required to stop highly energetic particles. The choice of a denser detector is also possible, but in that case the magnetic field must be correspondingly stronger if one is to acquire a momentum measurement as well. ATLAS compared to CMS is constructed as a physically larger but lighter detector, but both strategies are in use at the LHC.

Unless explicitly stated the source of the information in this chapter is [1].

5.1 Overview

The ATLAS experiment is divided into an onion-like structure of sub-detectors within each other. The inner-most detectors are responsible for tracking and momentum reconstruction. The intermediate calorimeters measures the total energy of all particles except neutrinos and muons. The outermost layer is the muon spectrometer, discriminating muons from other particles, while improving their momentum determination.

[1] The Compact Muon Solenoid detector (CMS).

5.2 Geometry and definitions

ATLAS is cylindrical, weighs $7,000$ tonne and is 44 m long and 25 m high. It is positioned at 'Point 1' the interaction point closest to the Meyrin site. In the following discussions, a right-handed cartesian coordinate system is defined by placing the origin at the interaction point (I.P.) in the middle of the detector. the z-axis is defined along the beam-pipe, the y-axis points vertically upwards and the $x-$axis points towards the centre of the LHC (roughy north from Point 1). Customarily a cylinder coordinate system is used as well, where R is the radial vector from interaction point and out, with an azimuthal angle $-\pi < \phi < \pi$ and a polar angle $0 < \theta < \pi$.

The initial momentum of the colliding partons in a hadron collision is effectively unknown (see section 3.1), but the transverse component is on the other hand well defined, consequently it is customary to express certain values in term of their transverse component, such as transverse energy, momentum and missing energy:

$$p_T = \sqrt{p_x^2 + p_y^2} = p \sin\theta, \tag{5.1}$$

$$E_T = \sqrt{m^2 + p_T^2} \cosh\eta, \tag{5.2}$$

$$E_T^{miss} = -\sum_i p_T(i). \tag{5.3}$$

The polar angle (θ) can be expressed in pseudo-rapidity, η, by:

$$\eta = -\log\left(\tan\frac{\theta}{2}\right), \tag{5.4}$$

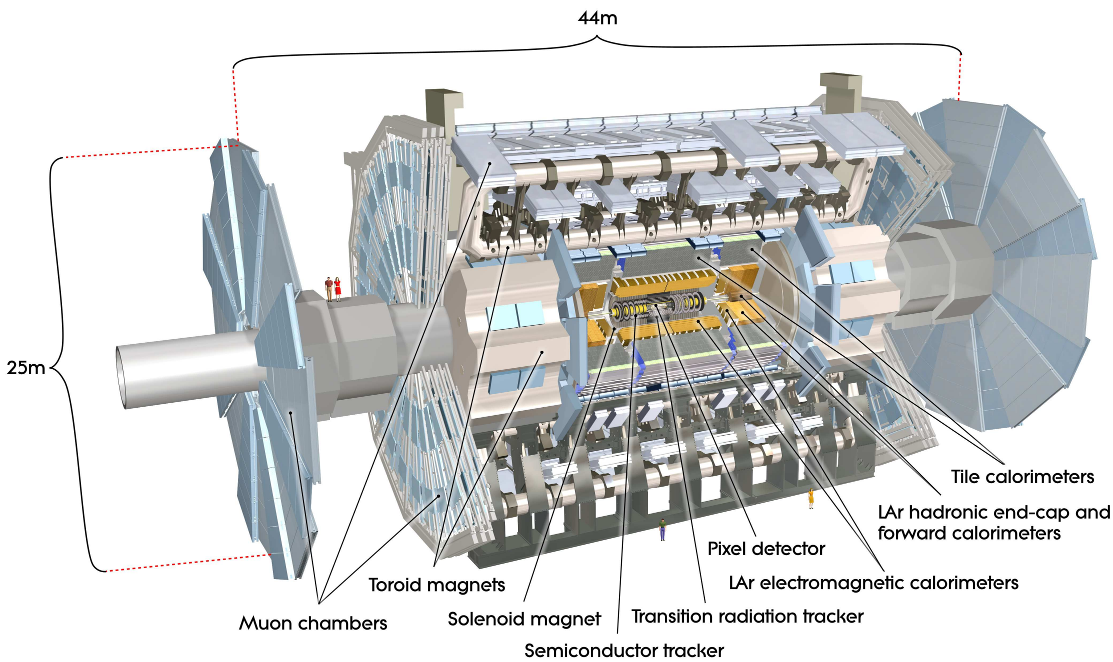

Figure 5.1: The ATLAS experiment.

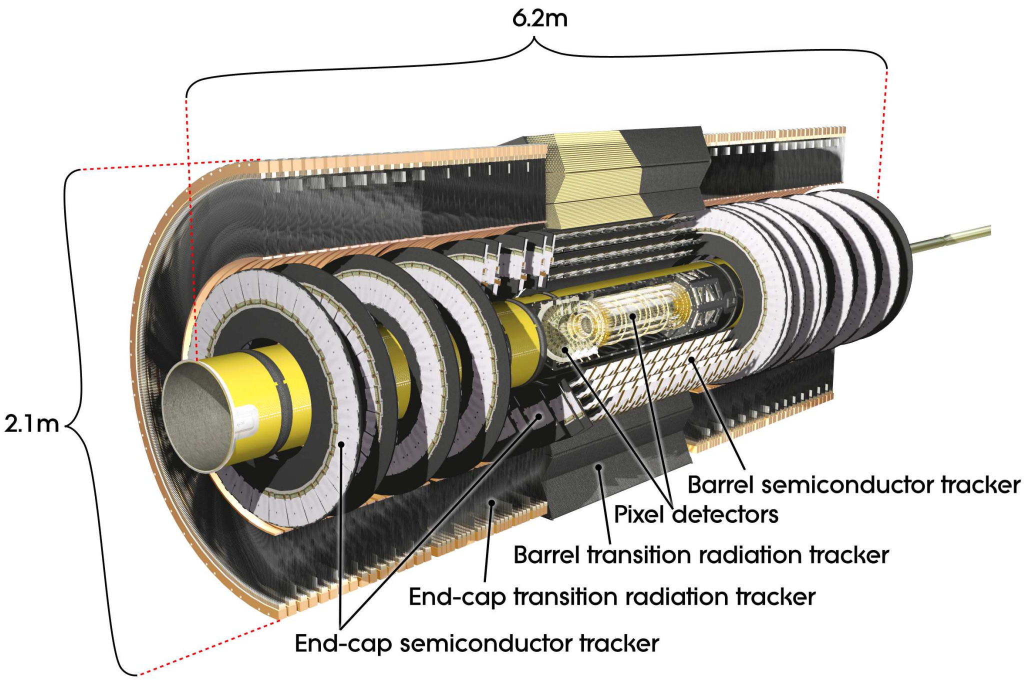

Figure 5.2: Cut-away of the inner detector.

where η is an approximation of the rapidity $y = \frac{1}{2} \ln \left[(E + p_z) / (E - p_z)\right]$, for highly relativistic particles. Rapidity transforms additively under boosts in the z direction.

Distances in the azimuthal - pseudo-rapidity plane are defined as,

$$\Delta R = \sqrt{(\Delta\eta)^2 + (\Delta\phi)^2}. \tag{5.5}$$

5.3 The Inner Detector

The inner detector is constructed to provide precise tracking capabilities: momentum reconstruction and vertex measurements as well as patten recognition. The inner detector is comprised of three independent systems that all provide excellent tracking, but using different technologies. The first two systems are silicon based, with a pixel tracker closest to the beam-pipe and a silicon-strip detector adjacent to the pixel tracker. The last system is a straw-tube tracker, with transition radiation capability for electron identification. In figure 5.2 the inner detector barrel and end-cap systems are visible.

The high collision rate expected at nominal LHC running causes the inner detector to be subjected to large doses of radiation. Radiation has therefore been a major concern in the design of the inner detector. The silicon detectors are cooled to around -10 °C to minimise dark current noise as radiation builds up in the detection material. Even so, the innermost layer of the pixel tracker is expected to be replaced after three years at nominal luminosity. The straw-tube detector in intrinsically radiation resilient, as the cycling of the gas mixture minimises charge build-up.

The material budget of the inner detector is kept as small as possible, to avoid excessive energy deposition as particles traverses the trackers, causing miss reconstruction of the

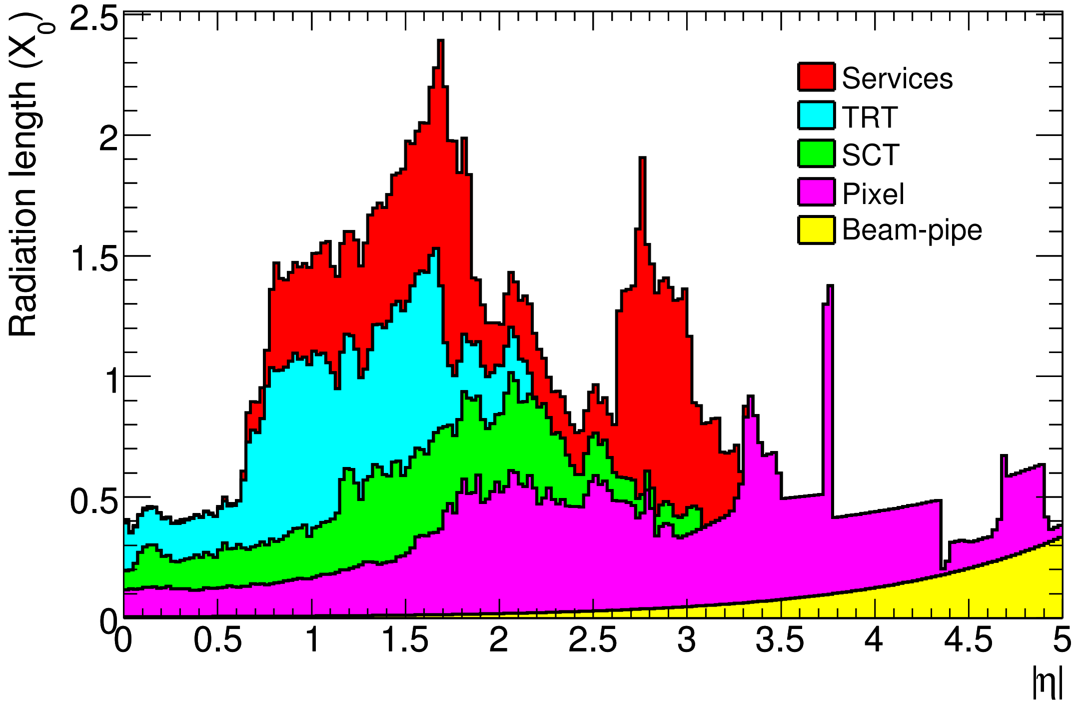

Figure 5.3: Inter detector material budget in radiation lengths X_0.

track trajectory, momentum and overall energy content, as the energy is deposited outside the calorimeters. Nevertheless photon conversion and energy loss from electrons due to bremsstrahlung is still quite high. The material distribution in the inner detector is illustrated in figure 5.3.

5.4 The Pixel detector

The inner most tracker is a silicon pixel detector, with high radiation resilience and resolution. The detector consists of 1744 modules (fig. 5.4) each with a detection area of 63×19 mm^2 and a thickness of 250 μm. The sensors have 46080 active pixels each.

The modules are placed in three layers around the beam pipe in the barrel region ($|\eta| < 1.7$), and three vertical disks at high pseudo-rapidity ($1.7 < |\eta| < 2.5$) on each side of the barrel. The total number of channels are thus 80.4×10^6.

Spatial resolution for a single module is $10(R - \phi)$ $115(z)$ μm

dE/dx estimation in the pixel detector

Please refer to section 7.1, for a detailed introduction to energy loss dE/dx. When triggered by an event, the pixel detector is requested an array of hits in the detector. This vector contains the physical coordinates, and a Time-over-Threshold (ToT) value. The ToT value is calculated by subtracting the trailing edge (TE) from the leading edge (LE). The threshold itself is defined by a voltage discriminator, and the counting cycle must

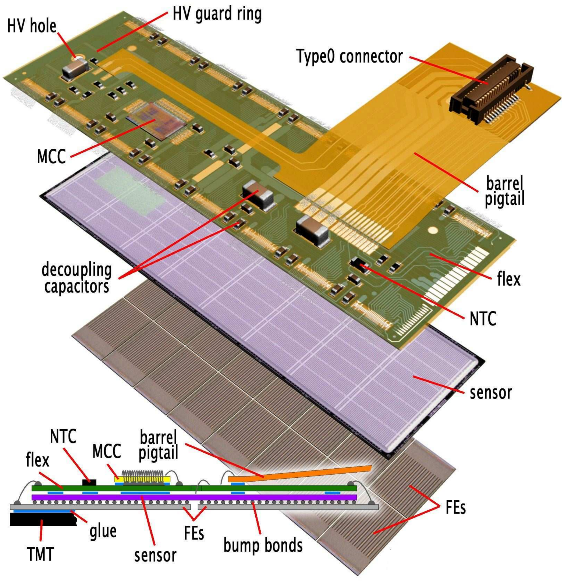

Figure 5.4: Pixel detector element.

occur within a time-frame set by the latency of the trigger system, figure 5.5 illustrates these quantities.

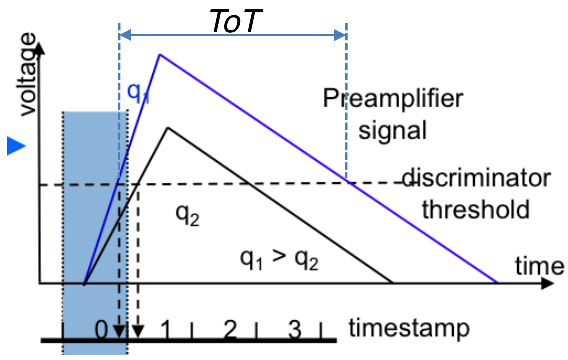

Figure 5.5: Time over Threshold definition.

The ToT value is calibrated in such a way that it respond with a value of 30 for a Minimum Ionising Particle (MIP) traversing the sensor pixel perpendicularly. The ToT is set to overflow at 255 limiting the maximum charge collected to 8.5 MIPs. Test beam studies with controlled charge injection into the pixel detector show a good linear relationship between charge deposition and Time-over-Threshold (ToT) response, as illustrated in figure 5.6.

The charged deposited by a particle crossing the pixel detector is rarely confined to a single pixel, and neighbouring pixels are clustered together based on the energy deposition gradient around the track. The charge of a cluster is calculated by summing the pixel charges after calibration corrections.

A series of quality cuts are applied to the clusters, to ensure a sensible dE/dx estimate.

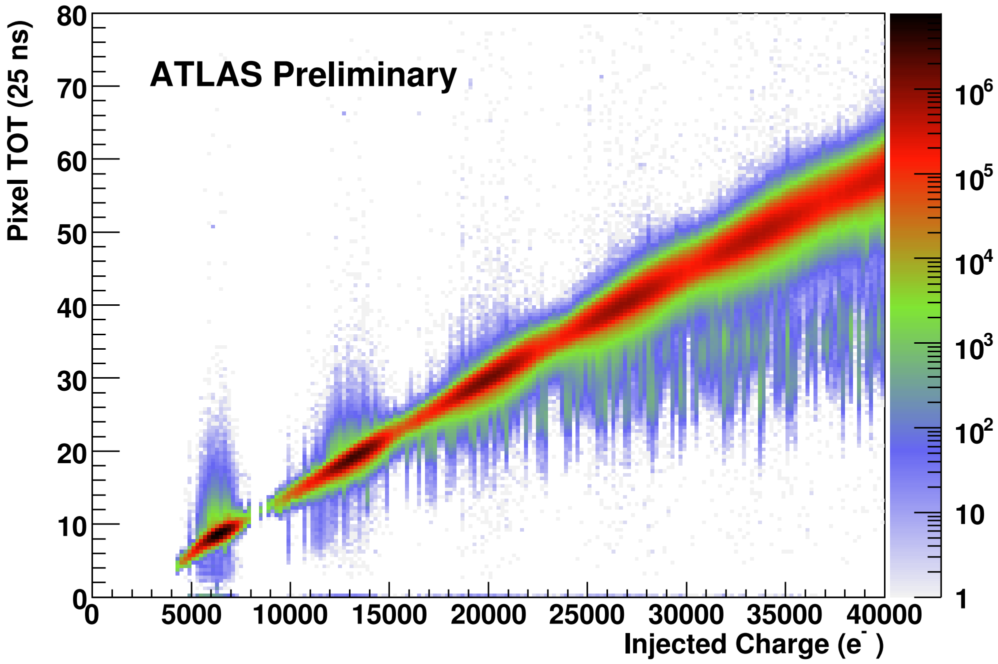

Figure 5.6: Time over Threshold vs collected charge in the Pixel tracker. Notice the linear relationship.

Specifically the physical location in the detector is of importance, as including the edges and gaps would lead to an unknown dx component, as the amount of material available for charge collection would not correspond to the global mean material thickness in the pixel detector. After quality cuts, the fraction of surviving clusters is $\sim 91\%$ of the original measured.

dE/dx

The pixel dE/dx is determined by dividing each cluster on the track with the path length, estimated by the geometry and the track trajectory. For a given track multiple clusters can be available, one in each detector layer. To reduce the Landau tails, coming from charge collection fluctuations, the measured dE/dx values are combined by truncation of the mean. The truncation scheme chosen removes the highest charged cluster for tracks with 2,3 or 4 good clusters. In case of 5 clusters, the two clusters with the largest charges are removed. Tracks with only one good cluster are discarded. The resulting dE/dx value is calibrated[2] such that a MIP deposits 1.24 MeVg^{-1}cm^2 as shown in figure 5.7.

The resulting dE/dx estimation tool have been validated on real data, for low momenta Standard Model particles. Figure 5.8 show the different bands from pions, kaons, protons and deuterons.

[2]By calibrated it is meant that the detector material properties are 'back-propagated' into the dE/dx estimation tool, rather than derived from first principle.

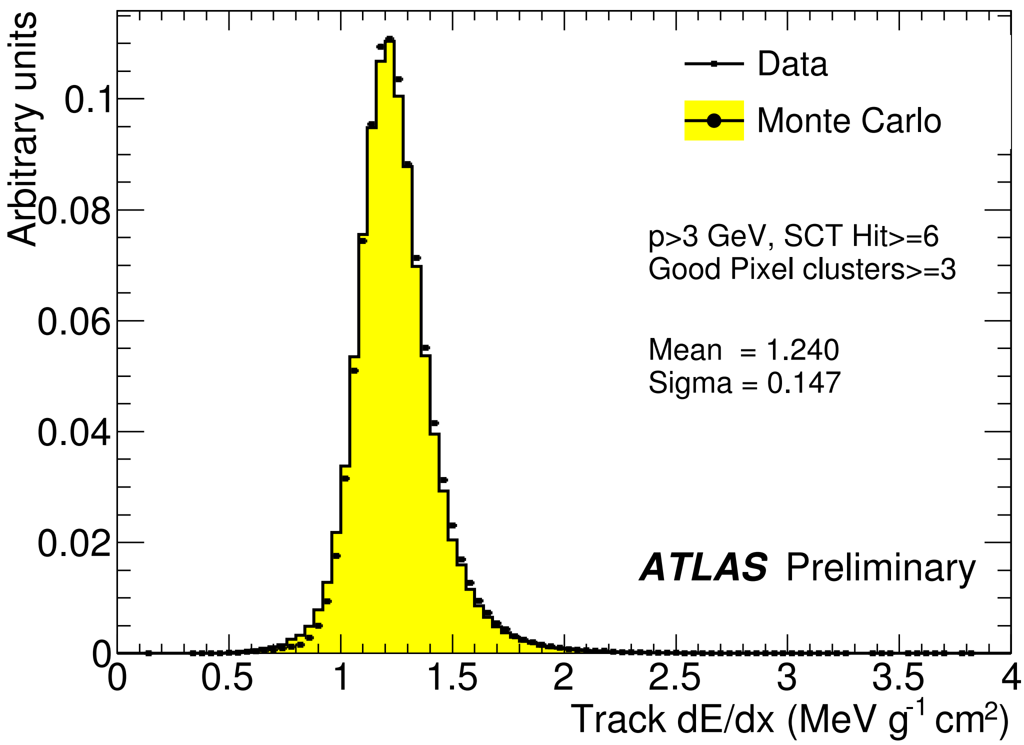

Figure 5.7: Pixel Tracker dE/dx after truncation.

The dE/dx variable is part of the Track Parameter information available at Analysis Object Definition (AOD) level (sec. 5.10) for each track after reconstruction, and is thus easy to use. The downside is that the hit information is being skimmed, making error propagation impossible for this estimator.

5.5 The SCT

The Semiconductor Tracker is a silicon strip detector with two slightly rotated detector surfaces per module. In total 4088 modules are used, creating a hermetic coverage of the interaction point with at least four space-point measurements for each track. The strip pitch of the barrel modules is 80 μm and the end-cap varies between 56.9 and 94.2 μm.

Spatial resolution for a single module is 17 μm in $(R-\phi)$ and 580 μm in (z).

5.6 The Transition Radiation Tracker

The Transition Radiation Tracker (TRT) consists of densely packed proportional chambers in the form of straws, embedded in a a radiator material of fibres and foils that enhances the probability of transition radiation as highly relativistic particles traverses the material. The emitted transition radiation is mostly soft x-ray photons ($\sim$ 5 keV). The straw detectors are filled with a gas mixture optimised at absorbing these photons, leading to

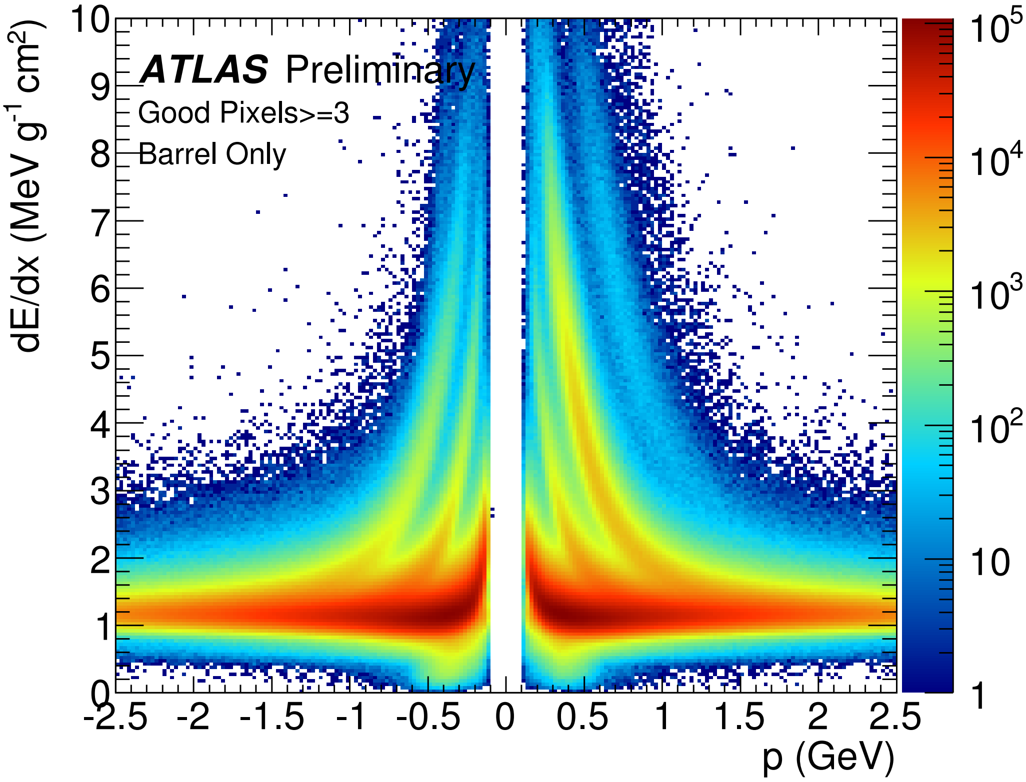

Figure 5.8: Pixel dE/dx vs. momentum. Bands from pions, kaons, protons and their anti-particles are visible as well as deuterons. The cut-off at low momentum is due to the tracking algorithm.

increased energy deposition. The transition radiation signature is a powerful PID tool for pion-electron discrimination at typical particle momenta for the LHC.

Each straw is 2 mm in radius, and is made of mylar coated kapton. The inner surface of the straws are coated with a 0.2 μm aluminium layer and serve as the cathode. The central anode in each straw is a gold coated tungsten wire 31 μm thick. The straws are filled with Xe (70%) CO_2 (27%) O_2 (3%), with Xenon instead of the cheaper Argon, customary used in drift chambers as avalanche medium, to absorb the transition radiation.

The TRT totals $298,304$ (2×122880 end-cap, 52544 barrel) straws. A full ADC readout of all channels has been deemed impractical. The larger charge deposition of a transition radiating particle is instead recorded by introducing two thresholds, rather than one during the digitalisation of the signal. The low threshold (LT) is set to trigger for minimally ionising tracks (250 eV), and the high threshold (HT) is set at roughly 6 keV (predominantly) triggering on transition radiating tracks [1].

The thresholds are readout in intervals of ~ 3 ns, and the LT state is sampled 8 times per bunch-crossing, and the HT once if the signal exceeds the HT within that time.

The resolution per straw is 140 μm ($R-\phi$), and the average number of hits per track is 35.

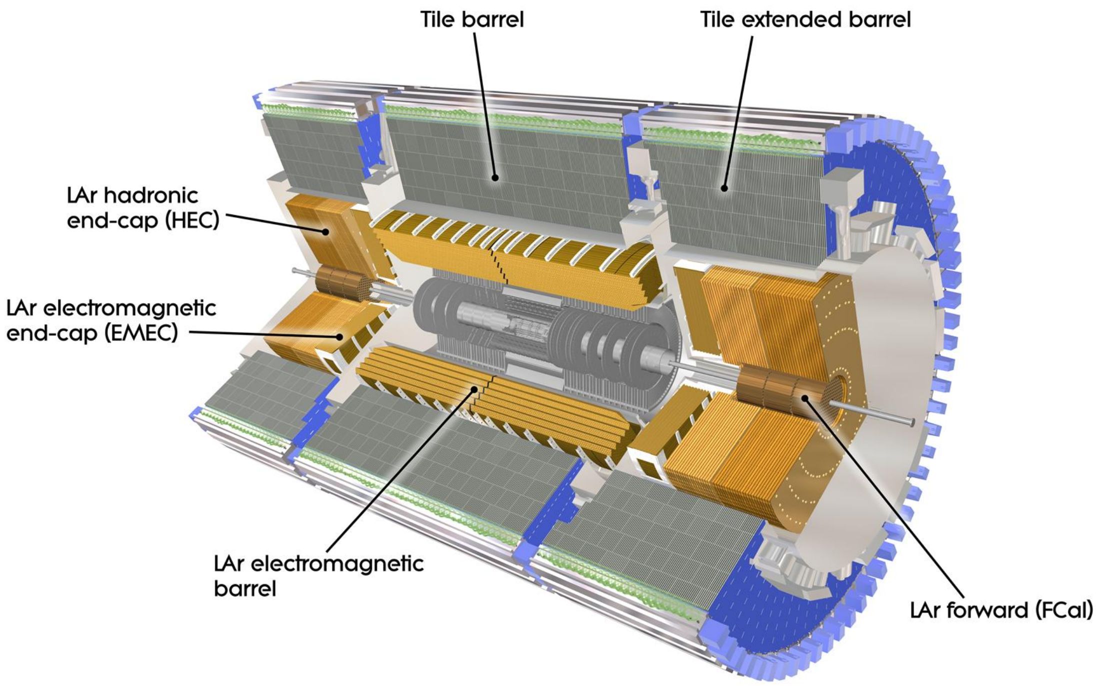

Figure 5.9: The ATLAS calorimeter systems.

5.7 Calorimetry

ATLAS is equipped with an electromagnetic and a hadronic calorimeter system, located between the inner detector and the muon spectrometer. The calorimeters cover a pseudo-rapidity range of $|\eta| < 5$, and are constructed based on two types of sampling-calorimeter technologies: Liquid Argon - lead (LAr-Pb) and scintillator - steel tiles (Tile).

The region with inner detector tracking ($|\eta| < 2.5$) is covered by a high precision liquid argon electromagnetic calorimeter, constructed with a finely segmented accordion geometry giving it good hermeticity, and high energy and position resolution, allowing precise measurements of electrons, photons, as well as missing energy. The hadronic calorimeter covering the barrel region ($|\eta| < 1.7$) is based on scintillator and steel tiles interleaved, to allow the large area as much radiation depth as possible at low cost. In pseudo-rapidity regions $|\eta| > 1.5$ the hadronic End-cap calorimeters extending to $|\eta| < 3.2$ uses Liquid argon like the electromagnetic barrel. Lastly a liquid argon based forward calorimeter covers the pseudo-rapidity all the way out to $|\eta| < 4.9$.

The LAr-Pb technology has been chosen for its linearity and stability as well as its radiation hardness, as the radiator material can be cycled without major interventions. The LAr is operated at a temperature of 88 K and a pressure around 1.25 bar.

The required depth of the calorimeter stack is related to the typical energy available in the collisions, to avoid particles escaping by punch-through the total depth of the electromagnetic calorimeter in the barrel region is around 22 radiation lengths (X_0) and 24 X_0 in the end-caps. The hadronic calorimeter is 9.7 interaction lengths (λ) in the barrel

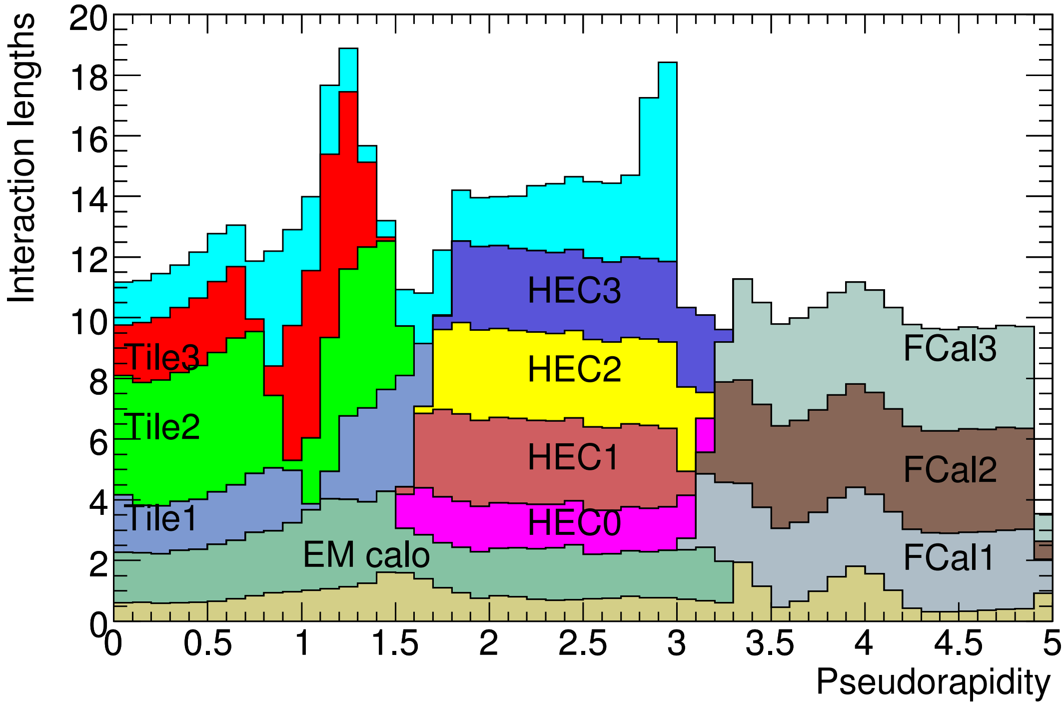

Figure 5.10: Material budget of the ATLAS calorimeters.

region and 10 in the end-caps. The overall material budget can be found in figure 5.10.

The electromagnetic calorimeter

The EM calorimeter is comprised by a series of accordion shaped (fig. 5.12) lead absorbers, with liquid argon in the crevices. A strong electric field is applied effectively turning the detector into a drift chamber. By using a liquid rather than plastic scintillators, the detector can be flushed when the detection medium is too ionised, making the detector very radiation resilient.

The accordion geometry of the EM barrel (fig. 5.11) is chosen to provided full coverage in ϕ without introducing artificial overlap or cracks for read-out electronics. The design also result in a very uniform resolution as a function of ϕ. The calorimeter cells are segmented in η to provide a uniform energy deposition as a function of pseudo-rapidity. The EM barrel is further divided into four layers (including the Presampler), with decreasing η resolution as a function of R. An exhaustive listing of coverage and granularity can be found in table 5.1, last in this chapter.

The total calorimetric depth is roughly constant in η, with the barrel region ($0 < |\eta| < 2.5$) segmented into three layers in R, but two layers in the end-cap region ($2.5 < |\eta| < 3.2$), as well as the overlap region between the end-caps and the barrel ($1.375 < |\eta| < 1.475$).

The energy resolution[3], as determined by test-beam studies of the barrel calorimeter

[3]The energy resolution have been estimated by test beam studies for electrons and pions, before

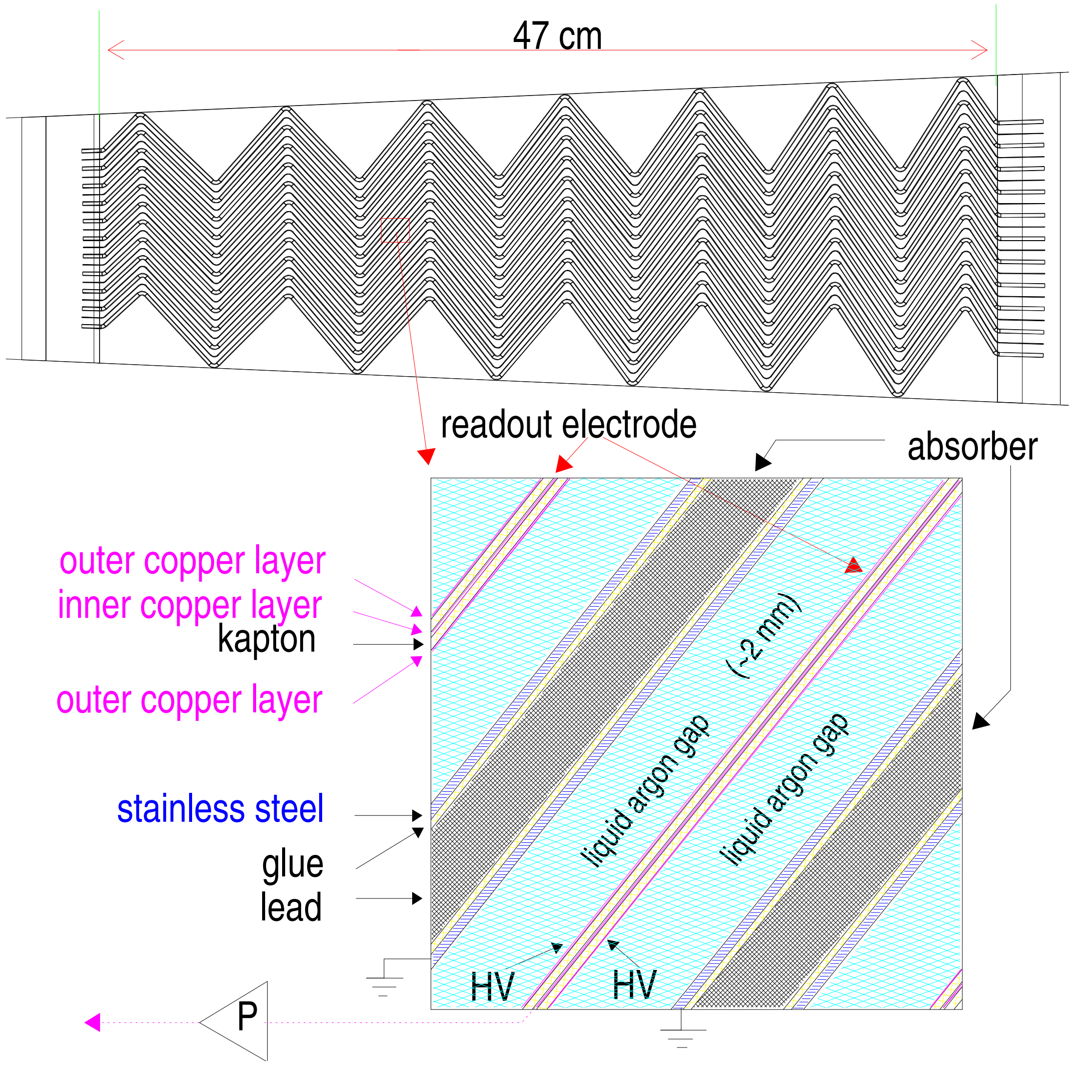

Figure 5.11: The accordion structure in the barrel region. The top figure shows a transverse view of a small section of the barrel module. The electrodes between the lead absorbers are kept positioned by honeycomb spacers. (ref. [10]).

is:

$$\frac{\sigma(E)}{E} = \frac{10.1\%}{\sqrt{E}} \oplus 0.17\%, \quad (|\eta| < 3.2) \tag{5.6}$$

where the first term is the sampling uncertainty and the second is due to mis-calibration and non-uniformity in the detector.

installation. The measurements have been fitted to $\sigma(E)/E = a/\sqrt{E} \oplus b\%$ where a is a stocastic term and b is a constant representing non-uniformities in the calorimeter response.

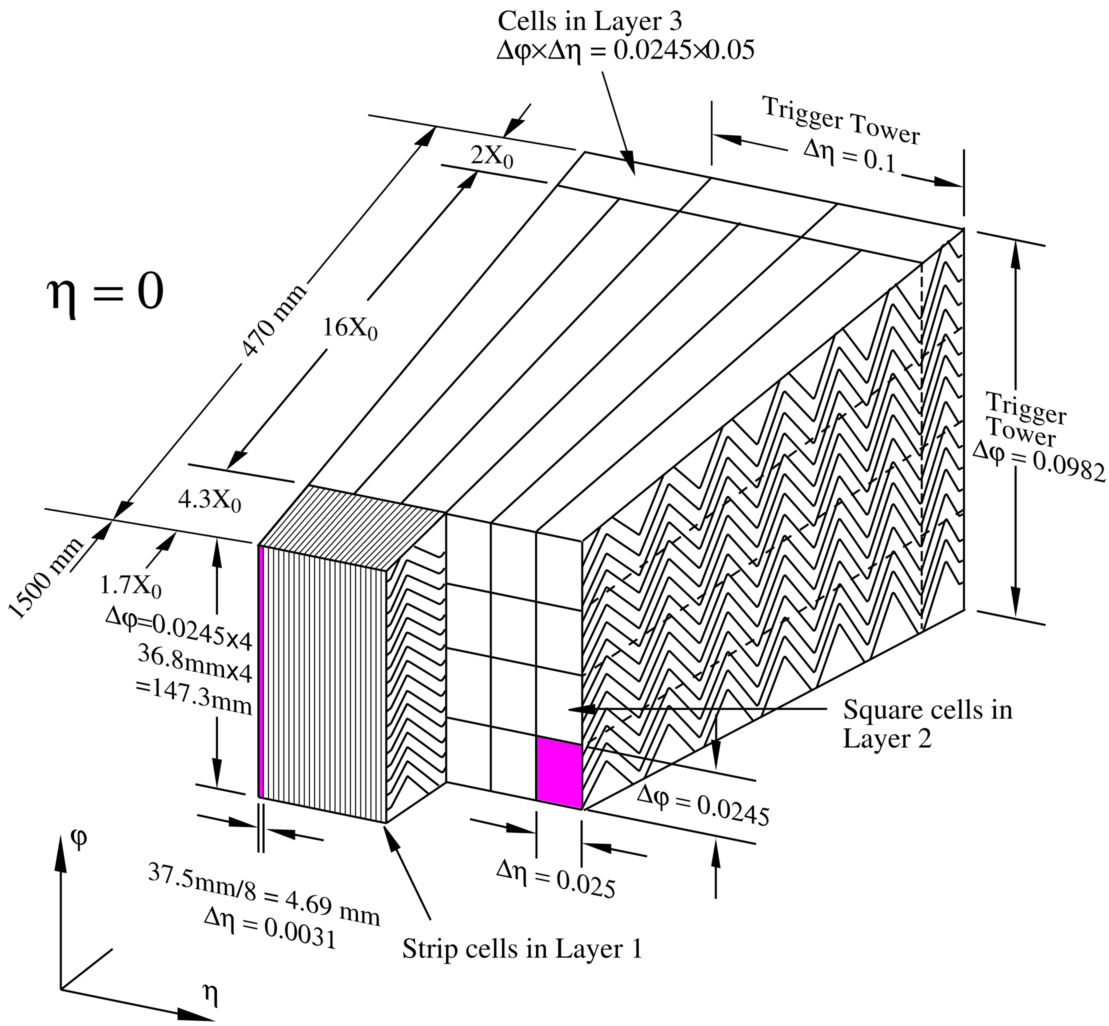

Figure 5.12: Liquid Argon calorimeter radial segmentation.

The hadronic calorimeters

The hadronic calorimeter is technologically separated into the barrel tile calorimeter and the end-cap LAr calorimeter.

The barrel covers $|\eta| < 1.7$ and is comprised of a central barrel system ($|\eta| < 1.0$) and two extended barrels ($0.8 < |\eta| < 1.7$). The tile calorimeter (TileCal) is made by stacks of absorber material (iron) and plastic scintillators. The barrel is placed directly after the electromagnetic calorimeter, and is 5.8 m long. The extensions are each 2.6 m in length.

The central barrel is separated into three layers, of 1.5, 4.1 and 1.8 λ in interaction lengths, and 1.5, 2.6 and 3.3 λ for the extend barrel. The inner radius is 2.28 m and the outer 4.25 m.

Between the central and the extended barrels a 60 cm gap is constructed to carry cables from systems placed before the hadronic calorimeter. This gap is covered by scintillating tiles and is called the Intermediate Tile Calorimeter.

The barrels each consist of 64 modules illustrated in figure 5.13. The modules are

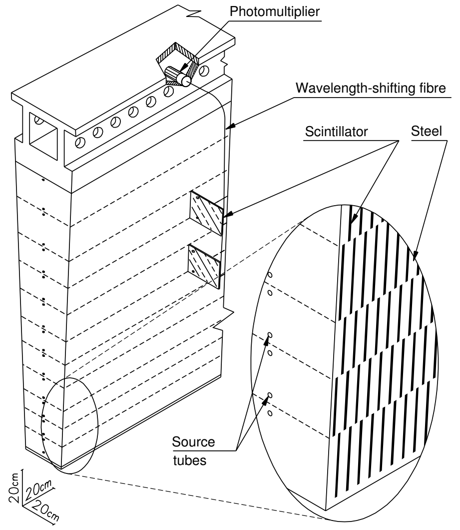

Figure 5.13: TileCal module.

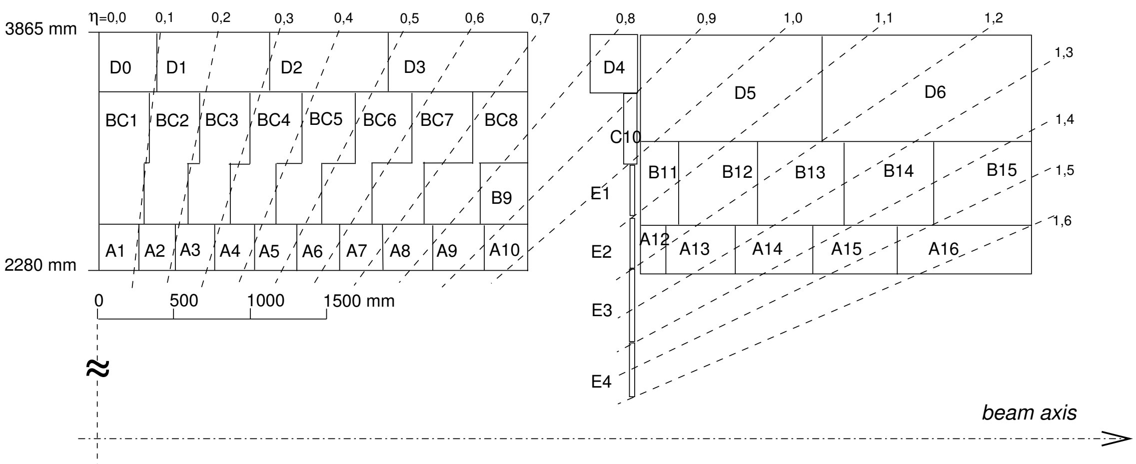

Figure 5.14: $R - z$ view of the tile calorimeter.

bundled into readout layers, denoted A, BC and D, as indicated in figure 5.14. The readout groupings are constructed in such a way as to provide a projective geometry in pseudo-rapidity. The scintillators are connected to two photomultiplier tubes (PMT) by wavelength shifting fibres. The two PMTs differs in gain by a factor of 64, to correct for signals produced in different regions of the module.

The hadronic end-cap calorimeter (HEC) is a copper plate - liquid argon calorimeter. It covers hadronic showers in $1.5 < |\eta| < 3.2$, and is positioned directly behind the electromagnetic end-caps. The HEC is organised into four layers in depth.

The energy resolution for hadronic jets are,

$$\frac{\sigma(E)}{E} = \frac{50\%}{\sqrt{E}} \oplus 3\%, \quad (|\eta| < 3.2) \tag{5.7}$$

in the barrel and end-cap, and

$$\frac{\sigma(E)}{E} = \frac{100\%}{\sqrt{E}} \oplus 10\%, \quad (3.1 < |\eta| < 4.9) \tag{5.8}$$

in the forward region [1, p. 5].

The forward calorimeter

The forward calorimeter (FCal) is both utilised for electromagnetic and hadronic energy measurements in the pseudo rapidity region $3.10 < |\eta| < 4.9$. Its main purpose is to increase the hermeticity, for the best possible missing transverse energy determination. The FCal has to be extremely radiation resilient to suvive in the environment close to the beam-pipe. The radiation requirement have dictated the use of liquid argon radiator material, but with copper absorbers in the first layer and tungsten in the last two. The total depth is roughly 10 interaction lengths.

5.8 The Muon Spectrometer

The muon spectrometer is constructed to measure muons deflected by large air-core toroid magnets, with a magnetic bending power in the barrel region of $\int \vec{B} \cdot d\vec{\ell} = 1.5$ to 5.5 Tm and between 1.0 and 7.5 Tm in the end-cap toroids.

The momentum resolution of a muon at 1 TeV/c is roughly,

$$\frac{\sigma_{p_T}}{p_T} = 10\% \text{ at } p_T = 1\text{TeV}, \quad (|\eta| < 2.7). \tag{5.9}$$

The detection stations utilised in the muon system comprises a near-complete study in detector physics. Monitored Drift Tubes (MDT), Multi-wire proportional chambers in the form of Cathode Strip Chambers (CSC) and two trigger systems: Resistive Plate Chambers (RPC) and Thin Gab Chambers (TGC) are in use.

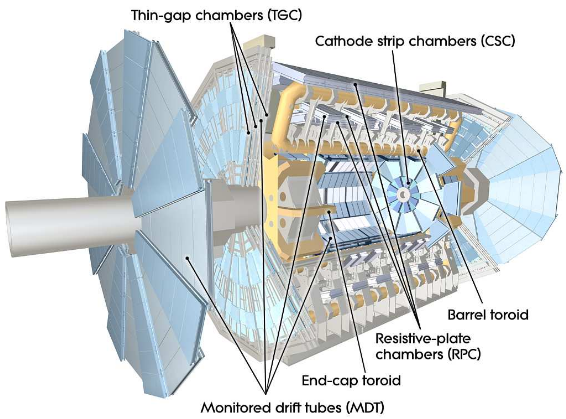

Figure 5.15: The ATLAS Muon system.

Monitored Drift Tubes

The MDTs are tube drift chambers, like the TRT, but with aluminium tubes rather than plastic and an argon gas mixture. The use tubes rather than larger arrays of wires in a single chamber enables flexible designs, and maximises redundancy, if one tube fails it will have little consequence to the overall efficiency, and the same design can be used for the end-caps and the barrel alike.

The MDTs provide a high spatial resolution, but the restitution time is close to 750 ns, making it unfit for high occupancy areas, such as the regions with $|\eta| > 2$.

Cathode Strip Chambers

In areas with a high counting rate, the MDTs are limited by their read out time. Instead CSCs are used. CSCs are multiwire proportional chambers, but with the cathode subdivided to enable charge interpolation as well as position information. the CSCs are used as the first layer of the muon system at $|\eta| > 2$, as they are able to sustain counting rates approaching 1000Hz/cm^2.

Resistive Plate Chambers and Thin Gap Chambers

Two types of fast triggering systems are applied in the muon system. Resistive Plate Chambers (RPCs) in the barrel region and Thin Gap Chambers (TGCs) in the end-caps. In order to separate tracks from different bunch crossings, the time resolution is on the order of a few nanoseconds.

5.9 Trigger system and data acquisition

At nominal intensity the LHC is expected to produce around 600×10^6 inelastic collisions per second at Point 1, with its 40 MHz bunch-crossings. The maximal read-out frequency of all the channels in ATLAS is around 75 kHz, and the storage system is only capable of handling around 200 events per second. Due to the large differences in data storage capability and collision rate, an efficient trigger system is needed to ensure that *interesting* events are kept while everything else is discarded. The trigger system in ATLAS is divided into three levels. The first level (LVL1) is implemented in hardware, and is connected directly to the muon trigger chambers and a reduced granularity calorimeter readout, supplying it with a rough picture of the event topology. The second level (LVL2) and the third called the Event Filter (EF) are combined known as the High-Level Trigger (HLT), and implemented in software running on a server farm situated directly adjacent to the detector cavern in a service area. At each level the trigger applies gradually more complete reconstruction to the events triggered by the previous level.

The trigger decision from level 1 must be propagated to the front-end electronics within 2.5 μs, and its based on signatures like high-p_T muons, jets and missing energy. Based on the trigger region found at level 1, called the 'Region of Interest' (ROI) the level 2 trigger analyses the ROI at full resolution, typically reducing the data rate to 3.5 kHz. The Event Filter is then seeded by the level 2 trigger, but have access to the entire event topology,

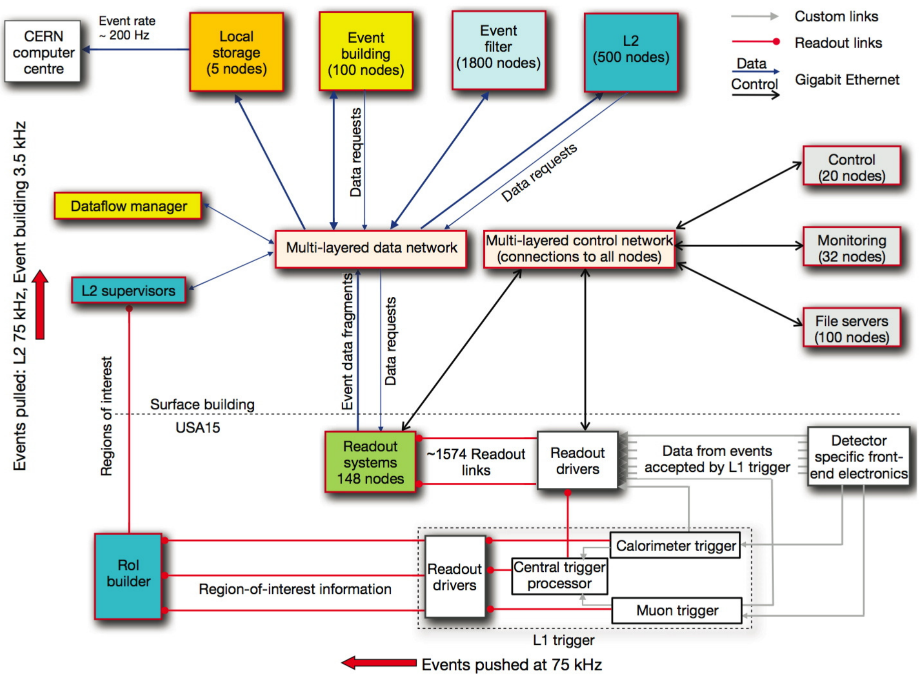

Figure 5.16: Trigger system.

and uses the same algorithms as the offline reconstruction. The event filter reduces the event rate to 200 Hz or around 300 MB/s.

5.10 The ATLAS software framework

The complicated machinery of the ATLAS detector is reflected in its software infrastructure. A general framework called ATHENA is used for simulation, reconstruction, calibration and physics analysis. The framework is ordered into components that can be exchanged without recompiling the entire framework, allowing people to independently add and modify the software, without affecting others.

The framework is written in C++ with run-time configuration scripts called *jobOptions* in Python. The underlying principles are basic object-oriented traditions such as:

- Abstraction
- Encapsulation
- Separation between data and algorithms
- Intelligent data handling. Based on the lifetime of a data object it is either stored in memory or on disk.

A clear distinction between different components are made to ensure reusability of code, especially the concepts of Algorithms and Tools have specific meanings that is important for this work:

- **Service**: Common software available to the whole framework. For instance histogram services or data access services.
- **Algorithm**: User application controlled by the framework (i.e. Analysis code or ntuple makers).
- **Tool**: A standalone program that can be shared between algorithms and executed by algorithms and services one or more times per event.
- **Data object**: An object-oriented representation of physics or detector information, for instance jets, calorimeter cells or electrons.

Computing and data formats

It is estimated that ATLAS will produce around $\mathcal{O}(10\ \mathrm{PB})$ of data yearly. Due to the large amount, a tiered computing model is used, where processing and storage is spread between multiple physics sites. These sites are connected in a network structure called Worldwide LHC Computing Grid or just 'The Grid', supplying a software and hardware fabric that allows for uniform execution of software over many heterogeneous clusters.

The tiered structure is divided into four main categories:

- **Tier 0 (CERN)**: First pass calibration, alignment and reconstruction. Archival of RAW data. Distribution of reconstructed output to Tier-1 sites.
- **Tier 1 (10 sites)**: Long term archival of a subset of the RAW data at each site. Precision calibration and alignment runs. Optimised reconstruction. Distribution of physics data to Tier-2 sites.
- **Tier 2 (35 sites)**: Physics analysis and simulation tasks.
- **Tier 3**: Local computer farms with grid access for end-user data.

As the data is processed and distributed, it is gradually distilled into increasinly abstract objects. The raw signal data from the detector is reconstructed into physics objects, and the physics object can be distilled further into event meta-data that can be used for skimming through large amounts of data fairly fast.

The following formats are available:

- **RAW**: 'Bytestream' data read out directly from the detector after triggering. (Event size 1.6 MB).
- **Event Summary Data (ESD)**: A combined format containing both reconstructed physics objects and low-level detector information. Useful for detector development, and low-level studies like the one presented in this thesis. (Event size 1.0 MB).

- **Analysis Object Data (AOD)**: Reconstructed objects, like tracks, particles and jets. Contains only a skimmed amount of detector information for refitting of tracks etc. (Event size 100 kB).
- **Derived Physics Data (DPD)**: If the standard ESD and AOD formats are insufficient for specific analysis and performance groups, derivations can be constructed with domain specific information.
- **TAG**: Meta information stored in a database, used for selected AODs and ESDs of interest. (Event size 1 kB).
- **NTuple**: The native Athena data formats are fairly complex and can only be analysed within the Athena software itself. To allow easier analysis outside Athena, flat ntuples can be made.

Table 5.1: ATLAS Calorimeter properties (Ref. [1]).

	Barrel		**End-cap**	
EM calorimeter				
Number of layers and $\lvert\eta\rvert$ coverage				
Presampler	1	$\lvert\eta\rvert < 1.52$	1	$1.5 < \lvert\eta\rvert < 1.8$
Calorimeter	3	$\lvert\eta\rvert < 1.35$	2	$1.375 < \lvert\eta\rvert < 1.5$
	2	$1.35 < \lvert\eta\rvert < 1.475$	3	$1.5 < \lvert\eta\rvert < 2.5$
			2	$2.5 < \lvert\eta\rvert < 3.2$
Granularity $\Delta\eta \times \Delta\phi$ versus $\lvert\eta\rvert$				
Presampler	0.025×0.1	$\lvert\eta\rvert < 1.52$	0.025×0.1	$1.5 < \lvert\eta\rvert < 1.8$
Calorimeter 1st layer	$0.025/8 \times 0.1$	$\lvert\eta\rvert < 1.40$	0.050×0.1	$1.375 < \lvert\eta\rvert < 1.425$
	0.025×0.025	$1.40 < \lvert\eta\rvert < 1.475$	0.025×0.1	$1.425 < \lvert\eta\rvert < 1.5$
			$0.025/8 \times 0.1$	$1.5 < \lvert\eta\rvert < 1.8$
			$0.025/6 \times 0.1$	$1.8 < \lvert\eta\rvert < 2.0$
			$0.025/4 \times 0.1$	$2.0 < \lvert\eta\rvert < 2.4$
			0.025×0.1	$2.4 < \lvert\eta\rvert < 2.5$
			0.1×0.1	$2.5 < \lvert\eta\rvert < 3.2$
Calorimeter 2nd layer	0.025×0.025	$\lvert\eta\rvert < 1.40$	0.050×0.025	$1.375 < \lvert\eta\rvert < 1.425$
	0.075×0.025	$1.40 < \lvert\eta\rvert < 1.475$	0.025×0.025	$1.425 < \lvert\eta\rvert < 2.5$
			0.1×0.1	$2.5 < \lvert\eta\rvert < 3.2$
Calorimeter 3rd layer	0.050×0.025	$\lvert\eta\rvert < 1.35$	0.050×0.025	$1.5 < \lvert\eta\rvert < 2.5$
Number of readout channels				
Presampler	7808		1536 (both sides)	
Calorimeter	101760		62208 (both sides)	
LAr hadronic end-cap				
$\lvert\eta\rvert$ coverage			$1.5 < \lvert\eta\rvert < 3.2$	
Number of layers			4	
Granularity $\Delta\eta \times \Delta\phi$			0.1×0.1	$1.5 < \lvert\eta\rvert < 2.5$
			0.2×0.2	$2.5 < \lvert\eta\rvert < 3.2$
Readout channels			5632 (both sides)	
LAr forward calorimeter				
$\lvert\eta\rvert$ coverage			$3.1 < \lvert\eta\rvert < 4.9$	
Number of layers			3	
Granularity $\Delta x \times \Delta y$ (cm)			FCal1: 3.0×2.6	$3.15 < \lvert\eta\rvert < 4.30$
			FCal1: $\sim$ four times finer	$3.10 < \lvert\eta\rvert < 3.15$,
				$4.30 < \lvert\eta\rvert < 4.83$
			FCal2: 3.3×4.2	$3.24 < \lvert\eta\rvert < 4.50$
			FCal2: $\sim$ four times finer	$3.20 < \lvert\eta\rvert < 3.24$,
				$4.50 < \lvert\eta\rvert < 4.81$
			FCal3: 5.4×4.7	$3.32 < \lvert\eta\rvert < 4.60$
			FCal3: $\sim$ four times finer	$3.29 < \lvert\eta\rvert < 3.32$,
				$4.60 < \lvert\eta\rvert < 4.75$
Readout channels			3524 (both sides)	
Scintillator tile calorimeter				
	Barrel		Extended barrel	
$\lvert\eta\rvert$ coverage	$\lvert\eta\rvert < 1.0$		$0.8 < \lvert\eta\rvert < 1.7$	
Number of layers	3		3	
Granularity $\Delta\eta \times \Delta\phi$	0.1×0.1		0.1×0.1	
Last layer	0.2×0.1		0.2×0.1	
Readout channels	5760		4092 (both sides)	

6

Event generation and Data retrieval

6.1 Event generation

R-Hadron event generation is done in the Pythia package [42]. Gluinos in this study is assumed to be direct pair produced. Customised routines have been developed for inclusion of final state R-Hadrons [18].

6.2 R-Hadron Interaction simulation

With event generation, a picture of the overall event geometry from the primary interaction is available. Unfortunately the real-life detector reconstruction is not perfect enough for direct comparison with the physics objects predicted by event generation alone. To compare prediction with experiment, the prediction must be further processed, by simulating how the event will look like after interaction with the detector material.

R-Hadrons are likely to behave differently than other particles, as they traverse material. The gluino can be viewed as a kinetic energy reservoir propagating in some direction, with the light quark system free to exchange constitutes by hadronic interaction when passing material. At LHC energies the expected combined kinetic energy of the light partons is roughly ~ 1 GeV, giving raise to reaction cross sections not unlike those of proton-proton and pion-proton interactions [8, 32]. Consequently the combined R-Hadron object have a chance of changing its electric charge in flight, as the light parton content fluctuates, but because the gluino remains unperturbed the momentum and the overall stopping power is constant throughout the length of the detector.

Simulation of particles traversing the material in ATLAS is done with the Geant4 simulation toolkit [15]. The R-Hadron interaction model has been implemented in Geant4 by Ref [28, 33].

6.3 Triggering

The trigger menu is selected to avoid obvious problems with out-of-time trigger signals from e.g. observing a slow moving particle in the muon system, several bunch-crossing too late. Instead, fundamental assumptions about the production mechanism (outlined in chapter 3) and the energy depositions are used instead.

The primary production channel is expected to be gg fusion, causing additional jets by initial-state radiation. The relatively modest energy deposition by the R-Hadrons in the detector system combined with the ISR jets causes missing transverse energy (MET) signatures. We are only interested in unprescaled triggers for this search, and as most low energy jet triggers are heavily prescaled, triggering on the ISR jets alone is not possible. Combining the ISR jet deposition with the missing energy from the R-Hadrons, it is possible to utilise unprescaled missing energy triggers, the trigger chosen is called xe40_noMu, which is a high level trigger, seeded by the L1_XE25 trigger. The advantage of using this trigger is that it is muon-system agnostic and have a higher trigger efficiency than the nearest jet-trigger alternative: EF_L1J95_NoAlg (ref. [8]).

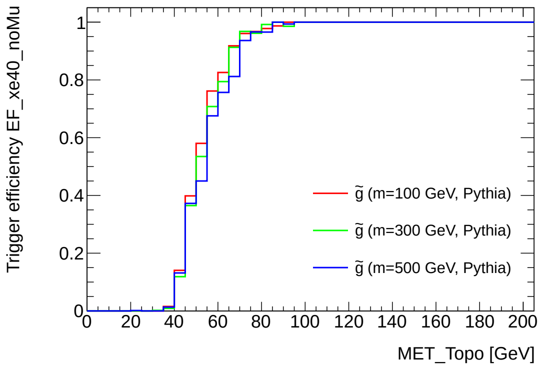

(a)

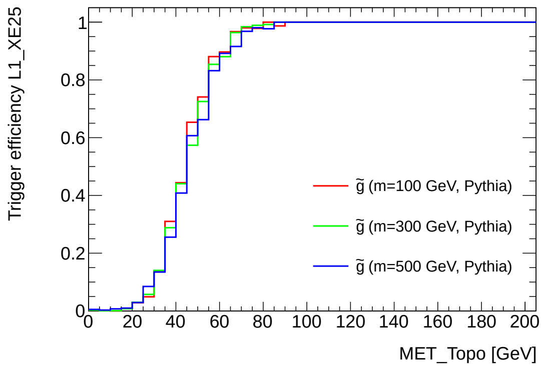

(b)

Figure 6.1: Turn on curves for 100 GeV R-Hadron. (from [8]).

6.4 Signal samples

Signal samples have been produced assuming $\sqrt{s} = 7$ TeV at ten mass points between 100 and 1000 GeV. The mass hypotheses are selected based on the foreseen available statistics and the kinematical envelope allowed at $\sqrt{s} = 7$ TeV p-p collisions.

The cross section for each mass point is estimated by PROSPINO as described in section 3.3. Every event is scaled by the cross section, to gauge the expected signal to background yield doing the analysis, but is not considered when calculating upper limits, where the absolute selection efficiency is used instead.

The scale factor for each event is calculated based on the observed 15.3 pb^{-1} integrated luminosity, by applying:

$$w_i = \frac{15.3 \text{ pb}^{-1}}{N_{evt}/\sigma_{\tilde{g}}} \tag{6.1}$$

All data samples used in this analysis have been produced officially produced by ATLAS central production.

The signal samples are listed in table 6.1 with their expected cross sections, and corresponding integrated luminosity.

Mass (GeV)	$\sigma_{\tilde{g}}$ (pb)	N Events	Integrated lumi (pb^{-1})
100	21200.000	10528	0.497
200	625.000	10528	16.845
300	62.100	10528	169.533
400	10.400	10528	1012.308
500	2.340	10528	4499.145
600	0.634	10528	16605.678
700	0.194	10528	54268.041
800	0.065	10528	161720.430
900	0.023	10528	451845.493
1000	0.009	10528	1214302.190

Table 6.1: Signal samples, cross sections calculated at NLO by Prospino [6].

6.5 Background samples

The expected Standard Model background can be divided into QCD and EW processes. In general QCD jets constitute a large background at the LHC, and especially low energy jets are produced in abundance. The amount of events required to full simulate the lowest energies are prohibitively resource consuming, and only a small fraction have been produced. This can cause serious fluctuations in the analysis as a single simulated event accounts for a massive number of scaled events. As R-Hadrons are produced with high momenta, the key to avoid problems with underdetermined background samples, is to cut on the momentum. Besides jets, top quarks are also produced as potential background to R-Hadrons, as they are likely to decay into high-p_T muons. The last background considered is the electro weak decays producing muons, such as W and Z decays to $\mu\nu_\mu$ and $\mu\mu$. Also Z and W to τ and further into μ contributes to the expected background.

The simulated background samples used in the analysis is listed in table 6.2.

6.6 Data samples

The data used in this analysis is collected in the 2010 run periods labeled E to H and corresponds to an integrated luminosity of 15.3 pb^{-1}. Data quality flags set based on the status of the ATLAS subsystems is considered by filtering events by a "Good-Run List" [5], the number of surviving events after the GRL is used for the analysis, and for calculating the integrated luminosity quoted above.

Sample type	σ (pb)	N Events	Integrated lumi (pb^{-1})
QCD (Pythia)			
J0 (p_T : $8-17$ GeV)	9856800000.000	1400000	0.0001
J1 (p_T : $17-35$ GeV)	678080000.000	1400000	0.002
J2 (p_T : $35-70$ GeV)	40994000.000	1400000	0.034
J3 (p_T : $70-140$ GeV)	2196000.000	1400000	0.637
J4 (p_T : $140-280$ GeV)	87848.700	1400000	15.936
J5 (p_T : $280-560$ GeV)	2328.560	100000	42.945
J6 (p_T : $560-1120$ GeV)	33.620	10000	297.486
Electro-weak (Pythia)			
$W \to \mu\nu$	8939.800	100000	11.185
$W \to \tau\nu$	8936.600	100000	11.189
$Z \to \mu\mu$	855.740	50000	58.428
$Z \to \tau\tau$	854.020	50000	58.547
Top (MC@NLO Herwig)			
$t\bar{t}$ (semi-lep)	80.110	10000	124.833
$t \to \mu\nu$ single-top t-chan	7.180	2000	278.679
$t \to \mu\nu$ single-top s-chan	0.470	2000	4270.128
$t \to \tau\nu$ single-top t-chan	7.130	1998	280.314
$t \to \tau\nu$ single-tau s-chan	0.470	1998	$4,251.064$
$Wt \to$ inclusive	14.580	1999	137.096

Table 6.2: Background samples.

Good Run Lists

ATLAS is a complicated machine, and during collision runs the overall status of the detector can change. If for instance parts of the inner detector is offline due to errors or maintenance, the rest of the detector is still operational, but with diminished detector availability. Likewise, the LHC could be in a ramp phase, with 'unstable beams', this situation would be potentially dangerous for the inner detectors, but other systems might be logging information for beam alignment. At any single point during operation the status of the entire machine is saved into a condition database. This data is later used to calculate Good Run Lists (GRL). These lists are useful when analysing data, as they contain data quality flags run by run. So if for instance an analysis requires the muon spectrometer and nothing else, a GRL can be produced masking the runs in a dataset where the muon spectrometer was offline.

The production of GRLs can happen on a per user basis, but in collaborations the group normally produces a common one, to enable direct comparison of results.

When calculating the integrated luminosity of a dataset the GRL must be supplied as well, to correctly determine the amount of data based on the runs flagged for use.

For this analysis a GRL prepared by the ATLAS SUSY group has been applied.

OTX Data Quality

When using the liquid argon calorimeters a problem has arisen with optical transmitters relaying signals from the front-end electronics on the detector to the back-end system outside the detector. These optical transmitters (OTx) causes erroneous energy responses to be recorded. Currently the OTx problem is not handled by the standard data quality system, so to avoid introducing false data into the analysis, the regions of the calorimeters affected must be filtered manually. For this a set of 2D histograms containing a map of the faulty regions is consulted for every track traversing the calorimeter.

Event overlap removal

The trigger system in ATLAS is separated into distinct data-streams. The streams are optimised for minimum overlap, but avoiding double counting in rare event searches is important. The data-stream corresponding to the selected trigger is called JetTauEtmis. The debug stream is used as well, to catch possible “problematic” but interesting events, dropped by being out-of-time with the bunch-crossing windows. The events in the two data-streams can in principle be overlapping, as the data-stream recording is non-exclusive. To avoid double-counting, overlap removal is performed before the analysis, by matching event and run numbers. Of the same event is present in both data streams, the JetTauEtmis stream vetoes the other.

6.7 Ntuple generation

The analysis is done outside the ATLAS framework, by processing ROOT ntuples. Conversion from ESD to ntuple files is accomplished by a Athena Tool called SYNTMaker “Stockholm & Yale NTuple Maker”.The tool read ESD data objects and write them to vectors, in such a way that for every event a new “page” is created in the ntuple file, containing a vector for each variable attributed to a physics object. For instance momentum, and the angles ϕ and η is stored for every track in every event inside a tuple. The estimators developed in chapter 7 have been integrated into SYNTMaker.

Skimming

All data and background monte-carlo samples, are skimmed to reduce the size of the files, and minimise the number of obvious uninteresting events. The skimming is done by:

- Require the event to pass any of a set of triggers outlined in section 6.3.
- Require the event to have at least one muon with a $p_T > 10$ GeV.

Muons are not required to be detected in the muon spectrometer at this stage, muons identified in the calorimeter during the reconstruction process are allowed as well.

6.8 Track matching

The ntuple files contains tracks reconstructed in the inner detector, muons reconstructed with combined inner detector and muon spectrometer measurements, and information

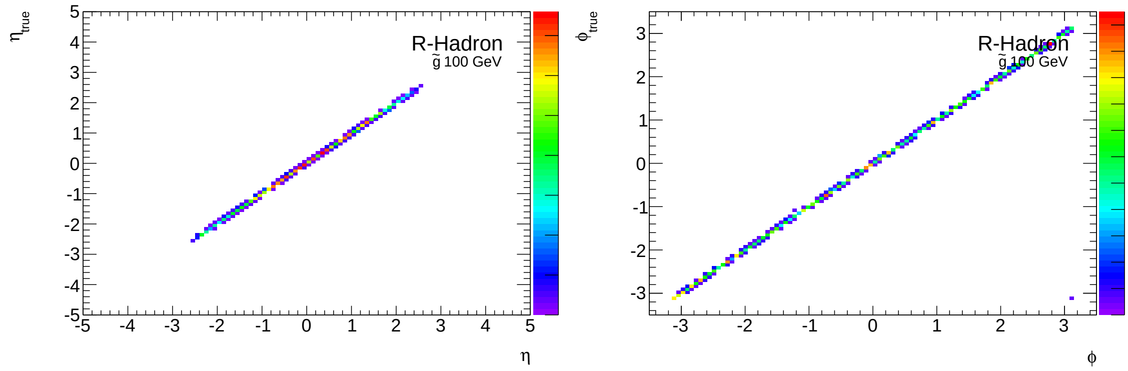

(a) η_{reco} vs η_{true} (b) ϕ_{reco} vs ϕ_{true}

Figure 6.2: Truth matching correlation for a 100 GeV R-Hadron.

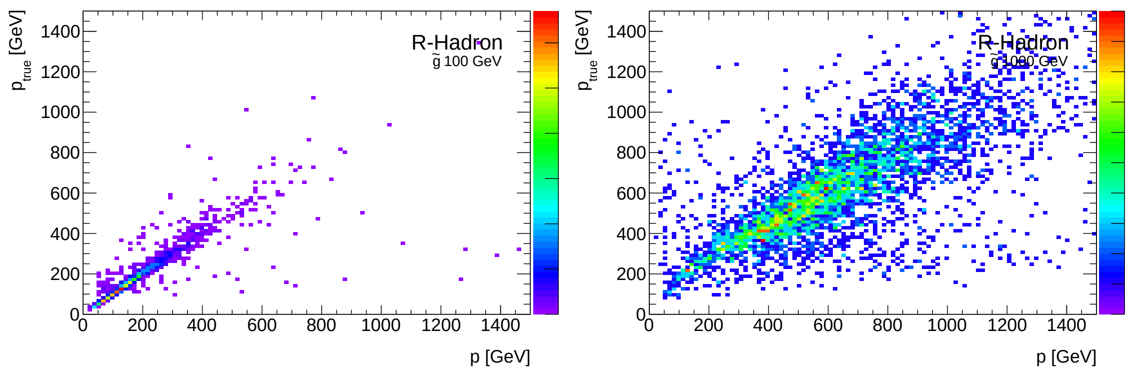

(a) 100 GeV R-Hadron (b) 1000 GeV R-Hadron

Figure 6.3: True momentum vs Reconstructed momentum.

about the true values created by the event generator before the ATLAS reconstruction chain. The three categories of information is not linked by default, if information about the true momentum is needed for a reconstructed track, track matching must be applied. The track matching scheme applied is implemented by minimising the distance between the objects in the $\eta - \phi$ plane:

$$\Delta R = \sqrt{(\eta_{reco} - \eta_{true})^2 + (\phi_{reco} - \phi_{true})^2} \tag{6.2}$$

To match a track to its truth information, the algorithm iterates over all truth objects and calculates the distance to each. If the distance is smaller than a threshold (i.e. $dR < 0.1$) and no other track have been matched to the truth object previously, the match is made.

In figure 6.2 the correspondence between true and reconstructed track can be seen for η and ϕ.

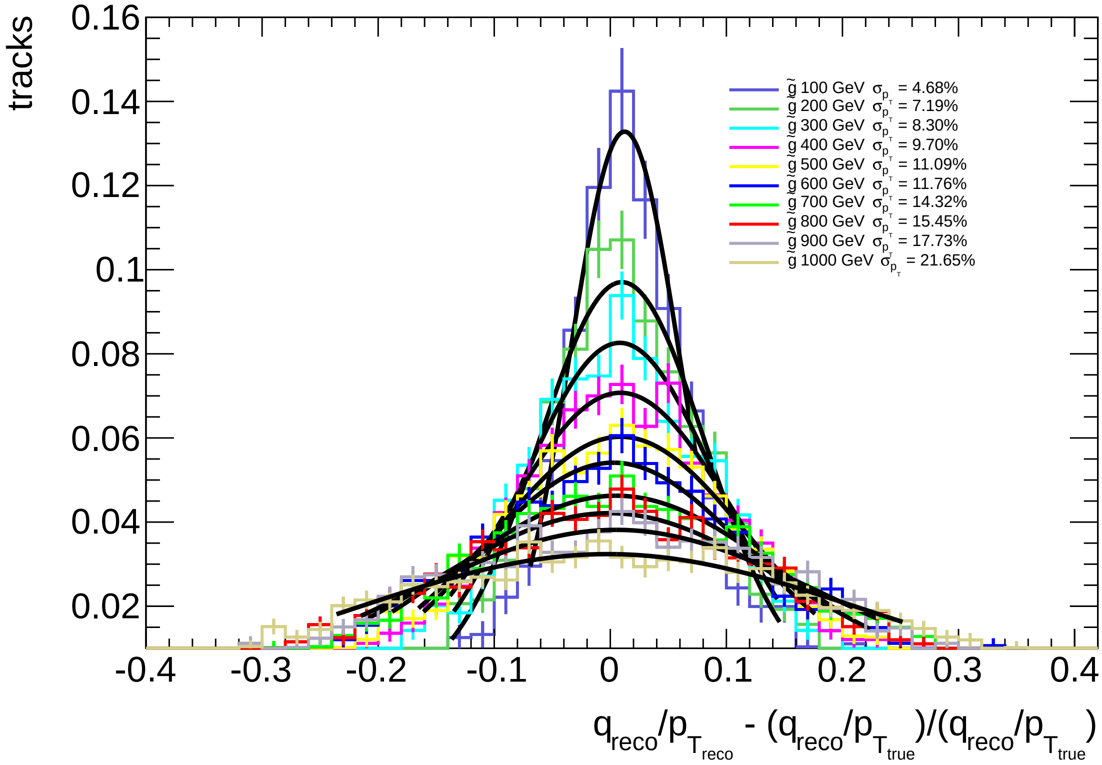

Figure 6.4: Difference between true and reconstructed momentum for R-Hadrons at various masses.

6.9 Momentum resolution

The momentum resolution cited in section 5.8 is not expected to related to R-Hadrons. At high masses, R-Hadrons will move at velocities $\beta \ll 1$ causing problems for the track fitter. Charge flipping could in principle also deteriorate the fit. Comparing the reconstructed momentum with the true momentum, for all the signal samples, we find that indeed the momentum resolution worsens as the mass increase. Figure 6.4 illustrates this comparison, the σ values represent the relative error by the width of a gaussian fit of the distribution for each mass point. In figure 6.3 the correlation in momentum from the match between reconstructed and truth, illustrates the same effect.

Part III

dE/dx based mass estimators

7

R-Hadron identification by dE/dx in calorimeters

Because of the timescales of particle physics, many of the processes of interest are not observed directly, but by developing a picture of what happened based on decay products measurable in the detector. This "reconstruction" of the original event is based on assumptions such as lepton, baryon and charge conservation, as well as energy conservation in terms of kinematics. A 'Z' particle can for instance be observed as two muons passing the muon spectrometer carrying specific momenta corresponding to the mass differences between the Z and the two muons. Most particle detectors including ATLAS are constructed to directly detect properties of known long lived Standard Model particles, such as photons, electrons and pions. Discriminating between these directly observable particles is done by assumptions based on their ionisation deposits and how far they can survive in the detector before being stopped. R-Hadrons being long lived, represent a special scenario where new physics can be directly observable like electrons and muons. Because ATLAS is a general purpose detector it has no specific method of discriminating new types of long lived particles, worst case is that the R-Hadrons will be treated like out-of-time muons belonging to an earlier event, based on their penetrative powers but low velocity.

If R-Hadrons exist but we are unable to distinguish them from muons or any other type of Standard Model particle, it would in effect, solely change the production cross sections for the Standard Model particles very slightly. To discriminate between long lived Standard Model particles and R-Hadrons, other estimators than just looking at the event geometry under the assumption that R-Hadrons reconstructs as a muon is needed. Such estimators should be based on specific observables optimally discriminating R-Hadrons from other particles. This chapter focuses on the development of one such estimator, based on the specific energy loss any charged particle suffers as it traverses some length of material.

7.1 Particle identification by energy loss

When electrically charged heavy particles traverses material at moderate velocities $v = \beta c$, they have a certain probability of interacting with electrons in the material. This interaction can cause ionisation or excitation of the atoms, leading to energy transfer from the projectile particle to the material. For particles moving at moderately relativistic velocities, the mean energy loss per unit length dE/dx can be defined by the "Bethe" equation [16],

Symbol	Definition	Units or Value
α	Fine structure constant ($e^2/4\pi\epsilon_0\hbar c$)	1/137.035 999 11(46)
M	Incident particle mass	MeV/c^2
E	Incident part. energy γMc^2	MeV
T	Kinetic energy	MeV
m_ec^2	Electron mass $\times$ c^2	0.510 998 918(44) MeV
r_e	Classical electron radius $e^2/4\pi\epsilon_0 m_ec^2$	2.817 940 325(28) fm
N_A	Avogadro's number	6.022 1415(10) $\times$ 10^{23} mol^{-1}
ze	Charge of incident particle	
Z	Atomic number of absorber	
A	Atomic mass of absorber	g mol^{-1}
K/A	$4\pi N_A r_e^2 m_ec^2/A$	0.307 075 MeV g^{-1} cm^2 for A = 1 g mol^{-1}
I	Mean excitation energy	eV (*Nota bene!*)
$\delta(\beta\gamma)$	Density effect correction to ionization energy loss	
$\hbar\omega_p$	Plasma energy ($\sqrt{4\pi N_e r_e^3}\ m_ec^2/\alpha$)	$\sqrt{\rho\,\langle Z/A\rangle}\times 28.816$ eV (ρ in g cm^{-3})
N_e	Electron density	(units of r_e)$^{-3}$
w_j	Weight fraction of the jth element in a compound or mixtu	
n_j	$\propto$ number of jth kind of atoms in a compound or mixture	
—	$4\alpha r_e^2 N_A/A$	(716.408 g cm^{-2})$^{-1}$ for $A = 1$ g mol^{-1}
X_0	Radiation length	g cm^{-2}
E_c	Critical energy for electrons	MeV
$E_{\mu c}$	Critical energy for muons	GeV
E_s	Scale energy $\sqrt{4\pi/\alpha}\ m_ec^2$	21.2052 MeV
R_M	Molière radius	g cm^{-2}

Table 7.1: Variables used in this section, (from ref. [16]). $\beta = v/c$ is the velocity and γ is the relativistic gamma factor, $\gamma = \frac{1}{\sqrt{1-\beta^2}}$. Mean energy loss is commonly plotted as a function of $\beta\gamma = \frac{p}{Mc}$, instead of momentum, as the energy loss is constant in $\beta\gamma$ regardless of particle mass.

$$-\left\langle \frac{dE}{dx} \right\rangle = Kz^2 \frac{Z}{A}\frac{1}{\beta^2} \times \left[\frac{1}{2} \ln \frac{2m_ec^2\beta^2\gamma^2 T_{max}}{I^2} - \beta^2 - \frac{\delta(\beta\gamma)}{2} \right]. \tag{7.1}$$

The Bethe equation describes the mean rate of energy loss for most materials[1] at projectile velocities in the region $0.1 \lesssim \beta\gamma \lesssim 1000$, for all charged particles heavier than the electron, illustrated by a muon in copper in figure 7.1. The variables in eq. 7.1 can be found in table 7.1. The energy loss is a specific material is in practice only dependent upon the projectile velocity β.

$$\frac{dE}{dx} \sim \frac{1}{\beta^2} \tag{7.3}$$

The velocity dependence can be explained by the observation that a slow moving particle spend a longer time in the vicinity of atomic electrons than a fast moving one [21], increasing its chance of elastic scattering.

[1] In practice, when referring to (7.1), in relation to moderately thick detectors, it is more correct to assume the most probable value (MPV) described by the Landau-Vavilov distribution [16],

$$\Delta_p = \xi \left[\ln \frac{2mc^2\beta^2\gamma^2}{I} + \ln \frac{\xi}{I} + 0.2 - \beta^2 - \delta(\beta\gamma) \right] \tag{7.2}$$

where $\xi = (K/2)\langle Z/A\rangle(x/\beta^2)$ MeV. See table 7.1 for explanations.

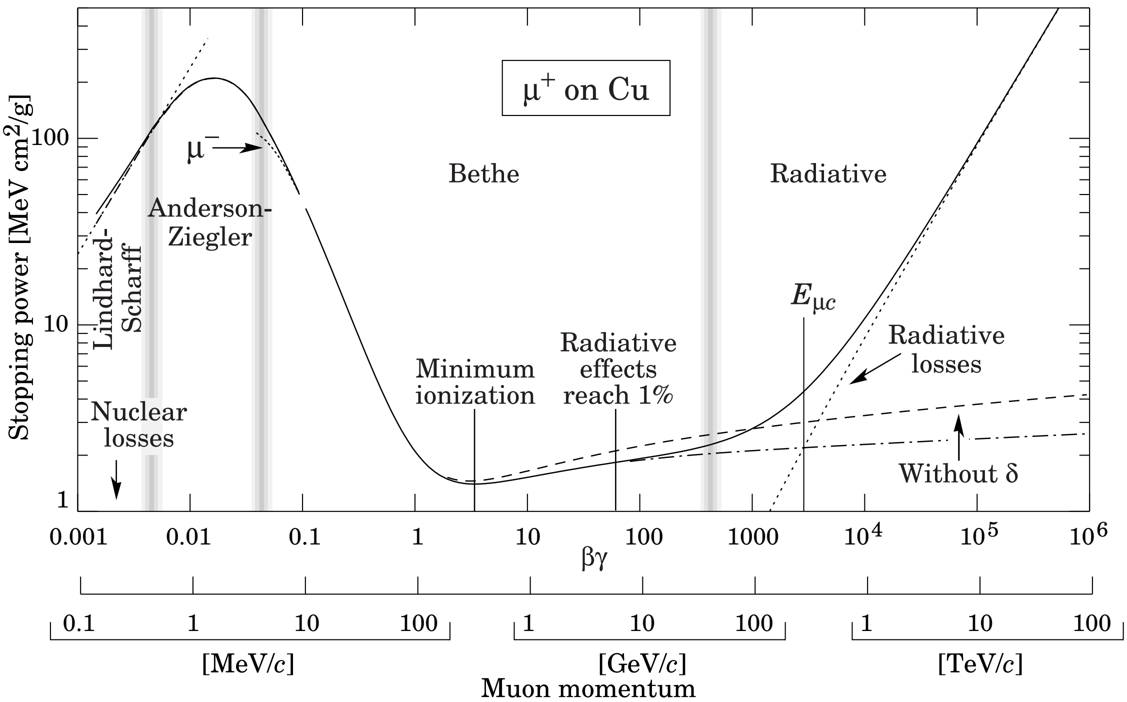

Figure 7.1: Stopping power for muons in copper as a function of $\beta\gamma$. The region discussed in the text is labeled "Bethe". Ref. [16].

Particles with different masses will at the same momentum move at different velocities ($p = Mv$), hence plotting dE/dx as a function of momentum will show characteristic rises in energy loss at specific momenta called depending on the particle type, depicted in figure. 7.2.

In most of the interesting processes observed at the LHC, the momentum of the Standard Model particles are many times higher than the region of the rise, and are said to be minimum ionising particles (MIPs), except for the muons[2] that can reach momenta high enough to loose energy by radiative effects. In general it is expected that all Standard Model particles produced ionises minimally, creating a widening band around 1 MIP (~ 1.5 MeV g^{-1} cm^2), rising at increasing momentum, due to relativistic effects.

R-Hadrons, if charged will show the same effect, but because of their high mass, the rise will happen at high momentum. Large energy losses at high momenta thus serve as a key signature for new long lived charged massive particles.

7.2 Specific energy loss in the ATLAS Calorimeters

The two calorimetric systems found in ATLAS (see general description in section 5.7) are constructed to measure energy content in particles by stopping them in dense material. The electromagnetic calorimeter predominantly causes electromagnetic interactions as photons, positrons and electrons enters. These interactions are primarily pair-production for photons and bremsstrahlung for the leptons, creating showers of leptonic particles

[2]Electrons are the exception in general, as they predominantly lose energy by bremsstrahlung.

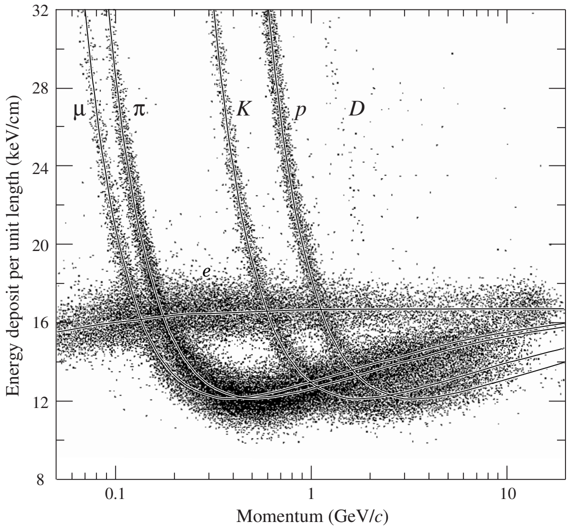

Figure 7.2: dE/dx as a function of momentum. At momenta less than 2 GeV characteristic rises in energy loss is observed for muons, pions, kaons, protons and deuterons. The horizontal band at 16 keV/cm is due to electrons. (Ref. [16]).

with gradually lower energy until the energy content of the incoming is absorbed in the calorimeter material. The hadronic calorimeter also causes electromagnetic showers in charged particles, but the denser material also give a high probability of hadronic scattering, causing hadronic showers. Depending on the depth of the calorimeter stack, only muons (and the ghostly neutrinos) have a high chance of escaping.

During commissioning of the ATLAS detector, cosmic muons have been used for in situ calibration of the calorimeter systems [4, 41]. The calorimeter energy scale calibration is outside the scope of this thesis, but calculations of dE/dx were performed as a study of energy deposition as function of momentum. The Electromagnetic calorimeter group found good correspondence to the theoretical expectation, see figure 7.3.

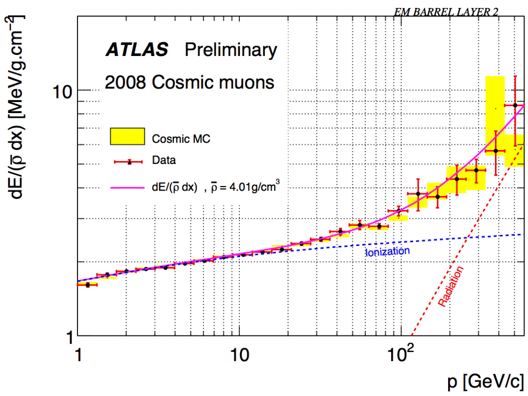

Figure 7.3: **LAr Calorimeter** momentum vs dE/dx for cosmic muons (run 2008).

Likewise the Hadronic calorimeter group have used cosmic muons for calibration studies, and have found a good linearity between energy deposition and path length in the calorimeter, illustrated in figure 7.4.

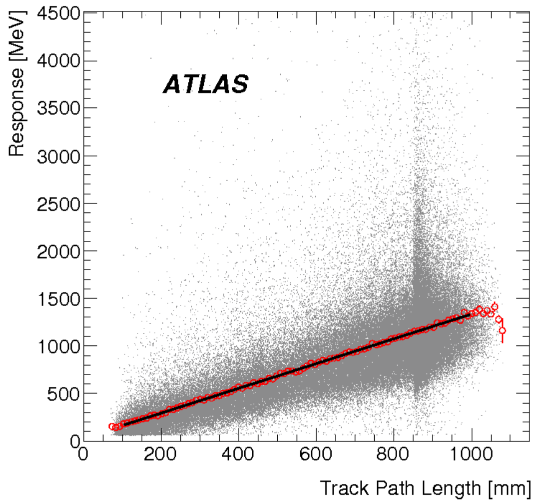

Figure 7.4: **Tile Calorimeter** dx vs dE for cosmic muons.

R-Hadrons should prenetrate both calorimeters much like muons, but because of their large mass, the ionisation should be closer to the low β rise found at $0.1 \lesssim \beta\gamma \lesssim 1$, giving it a significantly different signature from every other Standard Model particle, as they either causes showers or ionises very little in case of the muon.

The prospect of measuring "Bethe"-like energy loss from R-Hadrons in the calorimeters, has motivated the development of a software tool establishing this observable in my analysis.

7.3 Athena calorimeter dE/dx tool

Estimating dE/dx for a detector of some depth $dx \gg 1$ mm can be done by simply combining the energy deposition and the track path length. In practice the geometry and the energy deposition assumptions complicates matters greatly.

Considering the depth of the calorimeters dR and the angle in η one can estimate the distance traversed in the electromagnetic and hadronic calorimeters as a straight line by,

$$dx_{\mathrm{EMB}} = \frac{dR = 1970 - 1400}{\sin\{2\arctan[\exp(-|\eta|)]\}}\ \mathrm{mm} \tag{7.4}$$

$$dx_{\mathrm{Tile}} = \frac{dR = 4230 - 2280}{\sin\{2\arctan[\exp(-|\eta|)]\}}\ \mathrm{mm} \tag{7.5}$$

illustrated in figure 7.5a.

Without more precise geometry information it is difficult to get any results resembling the expected dE/dx values, as variations in the detector material across sampling layers smears the signal.

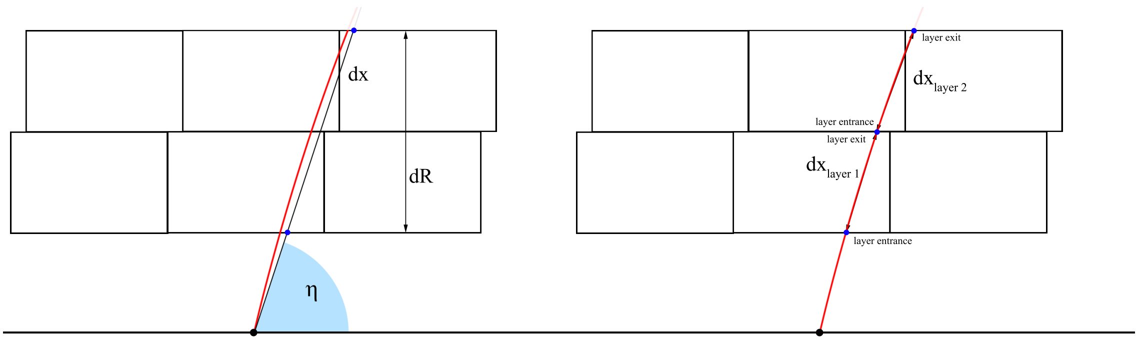

(a) **Initial dx method** The first way used to estimate dx, assumed that the entire calorimeter is one layer, with a known depth dR. The pseudo-rapidity η is utilised in calculating the effective distance by using formulae 7.4 and 7.5.

(b) **Current method** Use the ATLAS track extrapolator to find the entry and exit points in each calorimeter layer, and calculate the distance between these points.

Instead a tool is constructed in Athena that can access the correct geometrical model of ATLAS stored in the framework. This tool is a utilises official track extrapolation routines by calling a tool called TrackExtrapolatorToCalo [29], extrapolating inner detector track through the calorimeter, with correct handling of multiple scattering and other material effects. By combining this tool with the information about which calorimeter cells is crossed by the extrapolated track, it is possible to gain a precise estimate of dE/dx. The tool developed for this thesis is on the TrackExtrapolatorToCalo tool with the additional requirements relevant for the analysis, such as error propagation, and handling of miss reconstructed and noisy calorimeter readings. The functionally of this Athena tool called CaloSmpPidTool is to return estimates of dE/dx for each sub-calorimeter system in ATLAS. Additionally it calculates a particle mass estimate based on the method described in chapter 8. The sub-systems covered by the tool are listed in table 7.2.

CaloSmpPidTool implementation

For each track, the energy loss is calculated, as well as the extrapolated distance in each layer of each calorimeter. The dE and dx values of each layer is then combined, and the error on the dE/dx estimate is calculated.

The algorithmic flow of the Calorimeter dE/dx tool is described below.

Calculating energy loss (dE)

The method calculating the energy loss for each layer is illustrated by a flow-chart in figure 7.16.

1. The calorimeter cells crossed by the track are returned by the TrackInCaloTool, that extrapolate the track, through the calorimeters and look up the crossed cells in each layer. A vector of CaloCell objects is returned.

2. Each CaloCell contains a sampling layer value, that is distinct from the Track Extrapolator naming scheme. A map from the CaloCell naming to the Track Extrapolation naming scheme is done.

Estimator name	sub systems
Electromagnetic Calorimeter	
Presampler	PreSamplerB, PreSamplerE
Layer 1	EMB1, EME1
Layer 2	EMB2, EME2
Layer 3	EMB3, EME3
Hadronic Calorimeter	
Tile 1	TileBar0, TileExt0
Tile 2	TileBar1, TileGap1, TileExt1
Tile 3	TileBar2, TileGap2, TileExt2
Hadronic Endcap calorimeter	
HEC0	HEC0
HEC1	HEC1
HEC2	HEC2
HEC3	HEC3

Table 7.2: The 11 calorimeter dE/dx estimators, available in the CaloSmpPidTool, and the technical names for the corresponding subsystems.

3. The noise level from the general detector calibration in each cell is retrieved using the CaloNoiseTool. If the energy deposit in the cell is lower than the noise, the entire layer is abandoned.

4. A quality check is done as well, checking for cells marked as 'bad' in the geometry. If any cell crossed by the track in a layer is marked as bad, the entire layer is abandoned. (the track extrapolator does not know about good and bad cells, so even if we had a good cell in the same layer the dE value would not match the dx value)

5. Every crossed cell in each layer is summed.

6. The error δdE on dE (returned by the CaloNoiseTool) are added in quadrature.

7. the dE and δdE values for each layer are returned as vectors.

Distance traversed in layers (dx)

The track traversal length in each calorimeter layer is estimated by calling the ATLAS Track Extrapolator. By comparing the extrapolated track to the position of the calorimeter layers, an entry and exit position on each layer is found. The distance between these points are estimated as a euclidian distance. For R-Hadrons and muons, the two principal

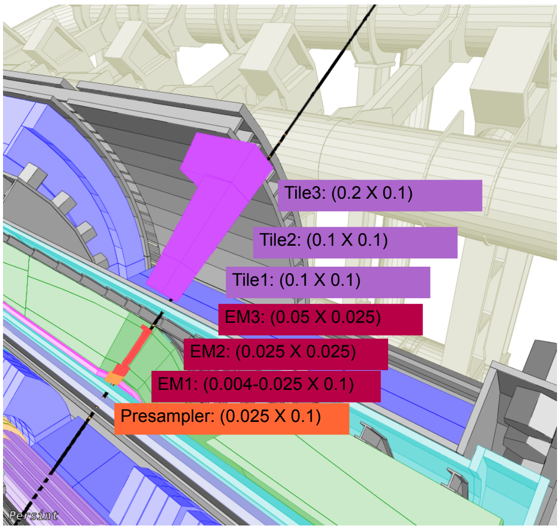

Figure 7.5: Energy deposition by a muon traversing the calorimeter layers in ATLAS. Ref. [30].

candidate particles for this tool, a straight line over the relatively short distances are not expected to contribute significantly to the overall uncertainness.

The error on the dx estimate, is not computed due to complications with the track extrapolator, but a small error on the order of a few percent is assumed.

A vector with dx and δdx are returned.

dE/dx

The final computation of dE/dx is done for every layers with a $dE > 0$ and a $dx > 0$. The error on dE/dx is calculated using first order error propagation,

$$\delta\frac{\mathrm{dE}}{\mathrm{dx}} = \sqrt{\frac{\delta\mathrm{dE}^2}{\mathrm{dx}^2} + \frac{\mathrm{dE}^2\delta\mathrm{dx}^2}{\mathrm{dx}^4}} \tag{7.6}$$

The Calorimeter dE/dx variables returned by the CaloSmpPidTool is stored in all the ntuples produced as part of the official R-Hadron analysis, making them easily accessible for use and verification by all members of the R-Hadron group.

Density normalisation

Traditionally dE/dx is presented as dE/($\bar{\rho}$ dx) where $\bar{\rho}$ is the mean density of the detector medium. This normalises the value making it comparable between detector types. The mean density for the Liquid Argon calorimeters is estimated to be [4]:

$$\bar{\rho} = 4.01 \text{ g cm}^{-3} \tag{7.7}$$

The dE/dx estimate for the liquid argon based calorimeters is returned in units of MeV g^{-1} cm^2 For the tile calorimeter no mean density have been estimated, and the value returned in units of MeV mm^{-1}.

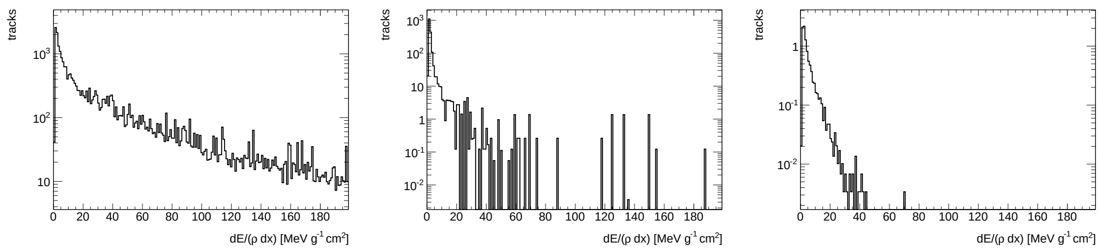

(a) Gluon. (b) Muon. (c) R-Hadron ($m = 500$ GeV).

Figure 7.6: LAr layer 1. fig. 7.6a QCD Jets. The dE/dx spectrum is contaminated by decorrelated measurements, but showing a rise at MIP energies from 'punch throughs'. fig. 7.6b Muons showing a clear MIP peak, and not much tail structure. fig. 7.6c R-Hadrons show a wider Landau tail than muons.

7.4 Results

The expected response from the CaloSmpPidTool can be divided into three categories: Muon-like, R-Hadron-like and thirdly the rest of SM.

- **Muons** should produced a MIP band with a gradual rise due to relativistic effects, for high-p_T muons.
- **R-Hadrons** should relative to the momenta show a signal corresponding to the band structure in figure 7.2, with a raise at low $\beta\gamma$ flattening around the minimum ionisation valley. In semi-dense material such as the electromagnetic calorimeter, charge flipping can occur, but at low enough rates to observe multiple ionisation bands. As R-Hadrons traverse denser material, we expect a decoupling between dE/dx and momentum especially in the deeper hadronic calorimeters, as the probability of charge flipping increases.
- **Other Standard Model particles** should in general not show much correlation between momentum and dE/dx in the calorimeter layers. In the electromagnetic calorimeter this is true because of the long sampling depth for dx relative to the high energy losses by electromagnetic showers, decoupling the energy loss from the distance extrapolated. In the hadronic calorimeter particles also exhibit nuclear scattering, producing non-'Bethe' energy depositions.

Plotting the dE/dx distribution for the first layer of the electromagnetic calorimter in the barrel region, for muons, QCD jets and R-hadrons, verify our expectations. In figure 7.6a we find that QCD jets don't exhibit any structure resembling the Landau distribution expected from a 'Bethe' like energy loss, instead we see a long fat tail gradually falling with decreasing production cross-section.

Muons in figure 7.6b show the expected peak at one MIP, with a steeply fall tail. In figure 7.6c R-Hadrons, like the muons have a tight distribution, but with a wider Landau tail, from the highly ionising particles at low β.

Looking at dE/dx vs momentum in the first layer of the electromagnetic barrel calorimeter, we get a clearer picture of the ionisation evolution as the velocity increases. In

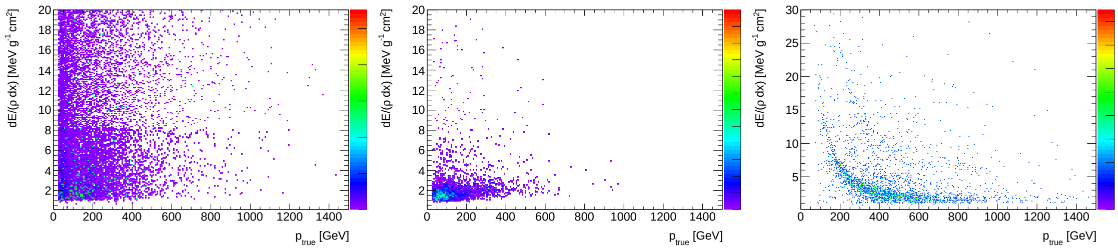

(a) Gluon. (b) Muon. (c) R-Hadron ($m = 500$ GeV).

Figure 7.7: dE/dx as a function of momentum.

figure 7.7c we see a clear band structure with a rise at low momentum for R-Hadrons. The gluon seeded jets show no correlation with momentum (fig. 7.7a).

The muon sample (fig. 7.7b) behaves as expected, we find a band structure around 1.5 MeVcm^{2}g^{-1} at the expected MIP level. The limited statistics in the muon sample makes it impossible to confirm the expected rise at high p, but the mean value is well established at the expected MIP value, confirming the density normalisation of the dE/dx value.

An important observation in figure 7.7c is the emergence of bands above the main band. We expect from eq. 7.1 that double charged particles should ionise four times as much as single charged particles. What we observed in the figure is indeed a band at around 4 MIPs, but also a slightly dimmer band at double the ionisation of the main band. The third band is a signal expected from an additional charged particle, ionising in the same calorimeter cells as the R-Hadron. The additional ionisation can be caused by remnants from hadronic interactions, in that case we would expect a gradual smearing with the number of interactions in each layer, as the remnants would be produced with varying momenta.

In figure 7.8 we see that for the same number of generated particles, at $\sqrt{s} = 7$ TeV the heavy particles ionises more than the light. This is expected as the 1000 GeV particles with be produced with a larger fraction of available energy bound in their masses, where the 100 GeV particles can be created with a considerable amount of kinetic energy at the LHC.

A complete table of figures for all signal masses can be found in appendix B.

Charge flow

Charge flipping is a well established part of R-Hadron phenomenology [33]. As an R-Hadron interact with material, the change of it changing its charge increases until it becomes an R-baryon [33, fig. 5.9]. Because of baryon conservation combined with a general lack of anti-baryons and mesons in the detector material, R-baryon to R-meson transitions are rare. If an R-Hadron is produced with charge 1 it will have probability p_{flip} of changing to one of the other possible states (see table 2.2) after some distance. From the graphs in figure 7.11, we can see the single and double charge bands in the first three layers in the electromagnetic calorimeter. For every particle it is possible to calculate the transition probability by geometrically segment the dE/dx–p plane into

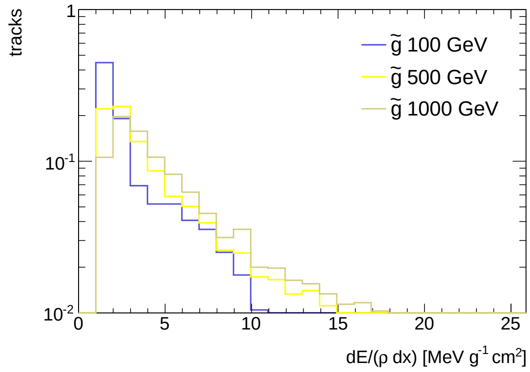

Figure 7.8: LAr layer 1, 100, 500 and 1000 GeV R-Hadrons.

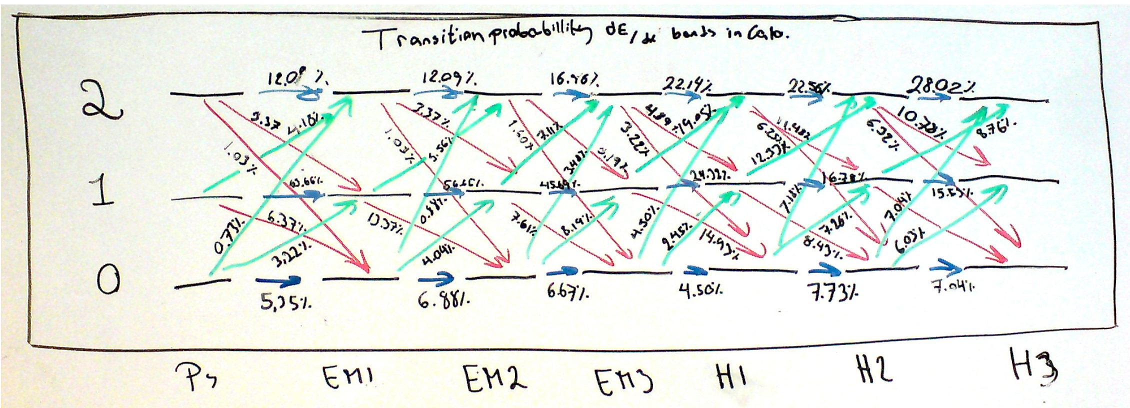

Figure 7.9: Transition probabilities, see figure 7.10 for definition of regions.

a charge 1 and a charge 2 region, and count how many times each particle is found in the two regions. Because of the increased smearing because of coarser granularity in the outer calorimeter layers, this technique becomes difficult in the tile calorimeter, with the exception of the last layer, where the band structures can be rediscovered (see figs. B.8 in appendix B). An attempt to quantify the transition probabilities have been made, segmenting 2D histograms of dE/dx vs p into three regions. One dubbed 0 where depositions outside of the charge 1 and char 2 regions. The separation is illustrated in figure 7.10. the resulting probabilities are drawn in figure 7.9, for practical purposes no attempt has been made to digitalise the visualisation.

Comparison with data

A comparison between Monte-Carlo and collision muons can be used to get a feeling for the performance of the dE/dx estimators.

Muons in collision events can be created close to jets, to avoid contamination from other particles, a few isolation cuts have been made before producing the following plots.

- Must pass trigger requirements defined in section 6.3.

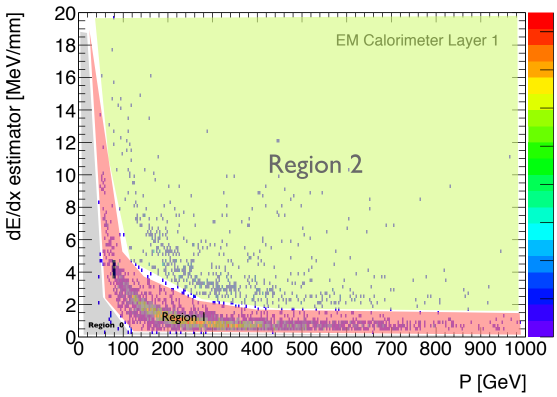

Figure 7.10: Transition regions.

- Must be flagged as a muon object from any subsystem.
- Distance to nearest jet object: $\Delta R_{jet} > 0.7$ (chapter 9.2).
- Must pass OTX requirements to avoid fake energy deposits from failing hardware in the electromagnetic calorimeter (chapter 6.6).
- Must pass the good run list (chapter 6.6).
- dE/dx values shall be larger than 0.

Comparing the data with the monte carlo expectations, we overall see a good agreement. The muon isolation is not as good in the real data as in the monte carlo where information about truth have been applied to filter the muons from background. The difference in statistics also affects the comparison, especially in the presampler and the third layer of the electromagnetic calorimeter.

In the presampler (fig. 7.13, 7.12), the difference in statistics is pronounced, so it is difficult to gauge wether the decorrelated dE/dx values at low momentum in the data plot is due to isolation issues or the detector geometry, but it is most likely isolation if we compare with figure 7.11a which show a good dE/dx vs p correlation for R-Hadrons in the presampler.

The rest of the layers exhibit good agreement between monte carlo estimation and data.

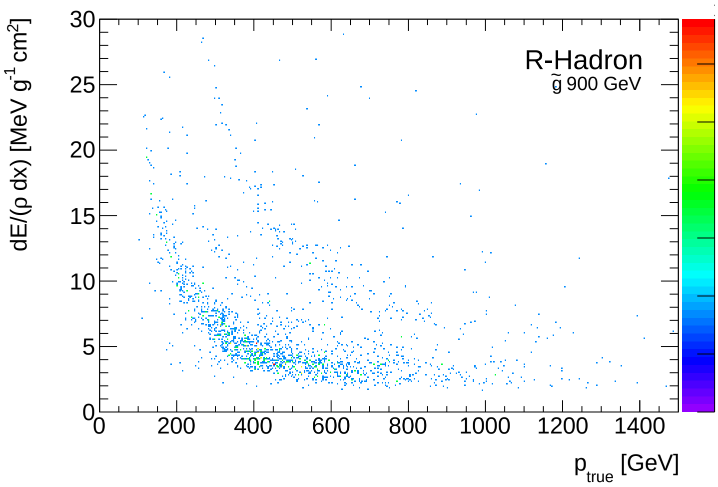

(a) Presampler

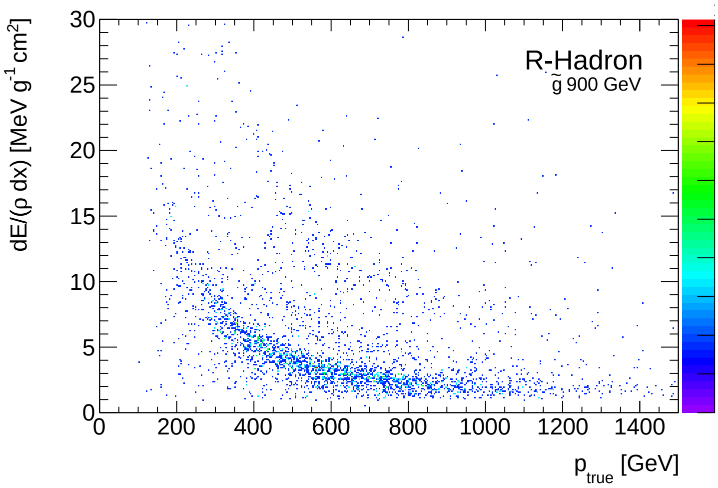

(b) LAr layer 1

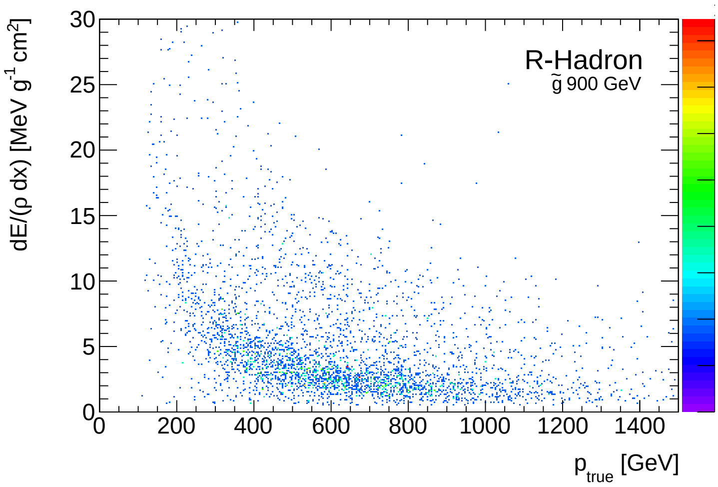

(c) LAr layer 2

Figure 7.11: R-Hadron (m = 900 GeV) in the first three layers of the electromagnetic calorimeter: 7.11a presampler, 7.11b layer 1 and 7.11c layer 2.

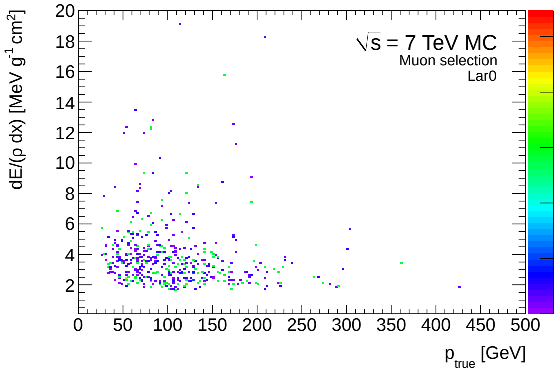

Figure 7.12: Presampler, monte-carlo dE/dx response versus momentum for muons.

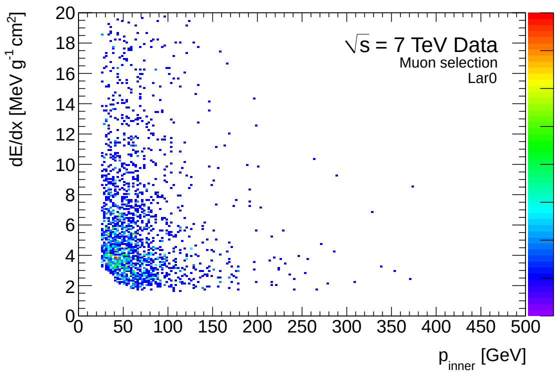

Figure 7.13: Presampler, data ($\sqrt{s} = 7$ TeV) dE/dx response versus momentum for muons.

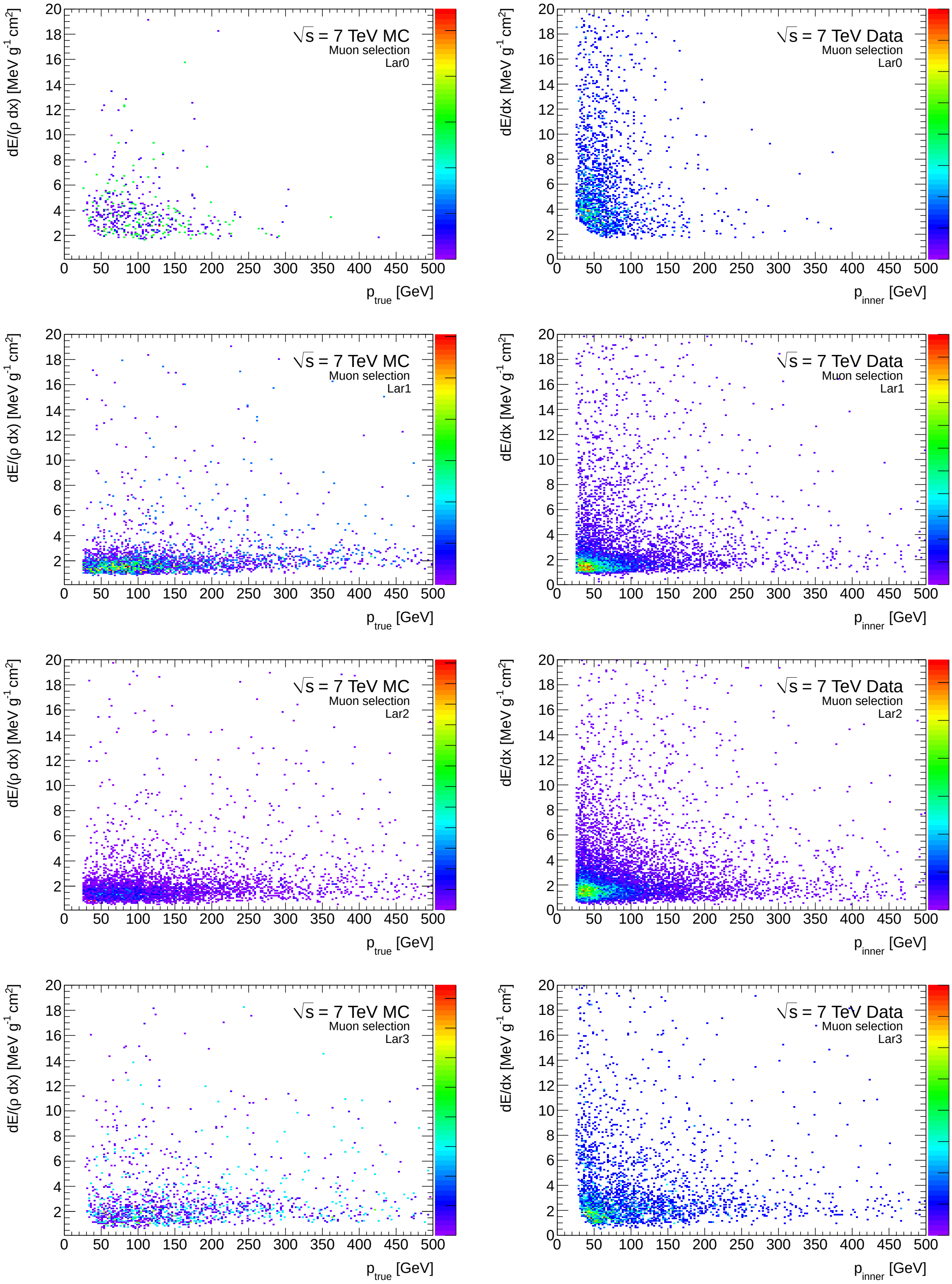

Figure 7.14: Muons data vs monte carlo in the Electromagnetic calorimeter.

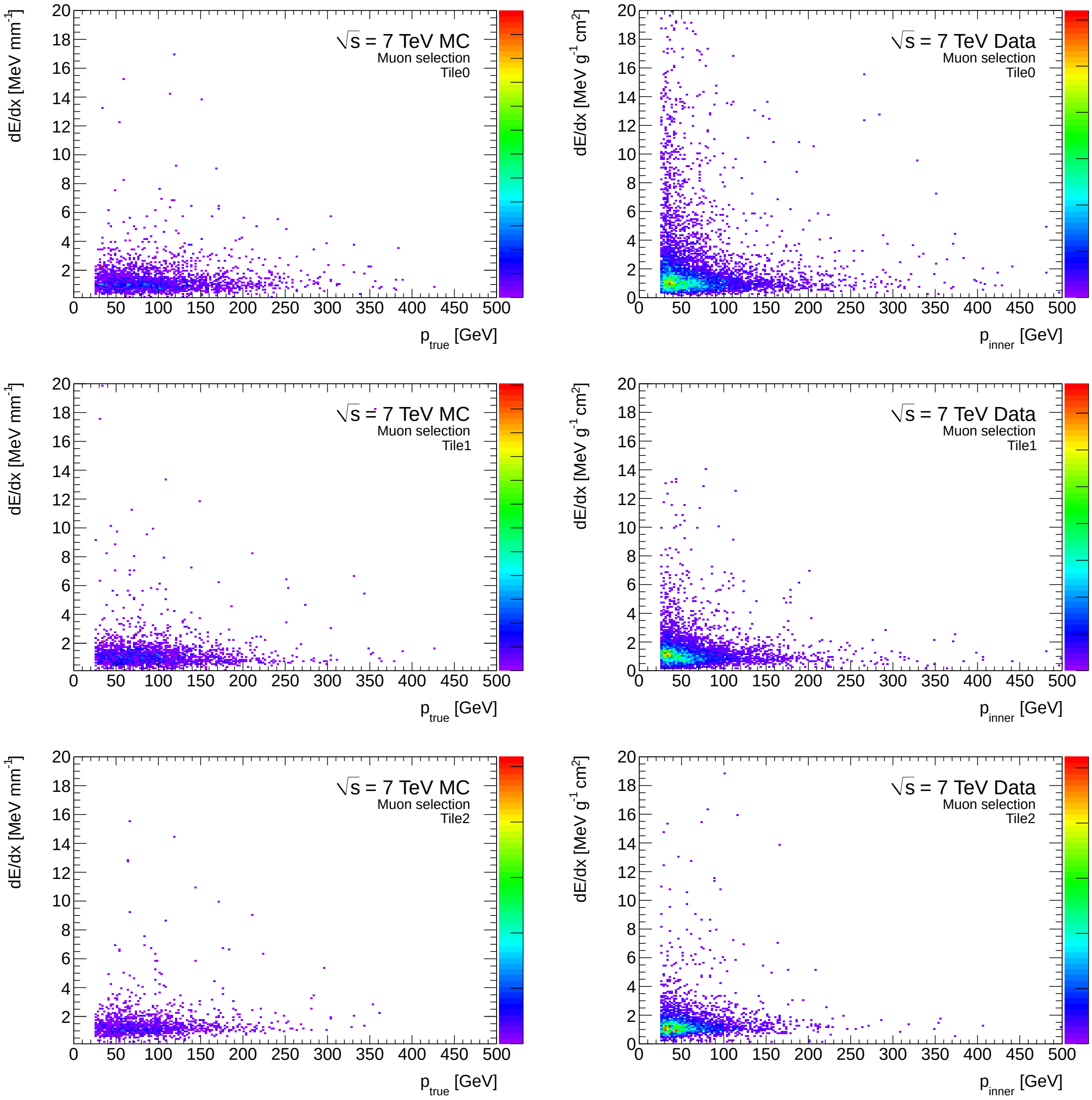

Figure 7.15: Muons data vs monte carlo in the Hadronic calorimeter.

Figure 7.16: Calorimeter dE/dx dE method.

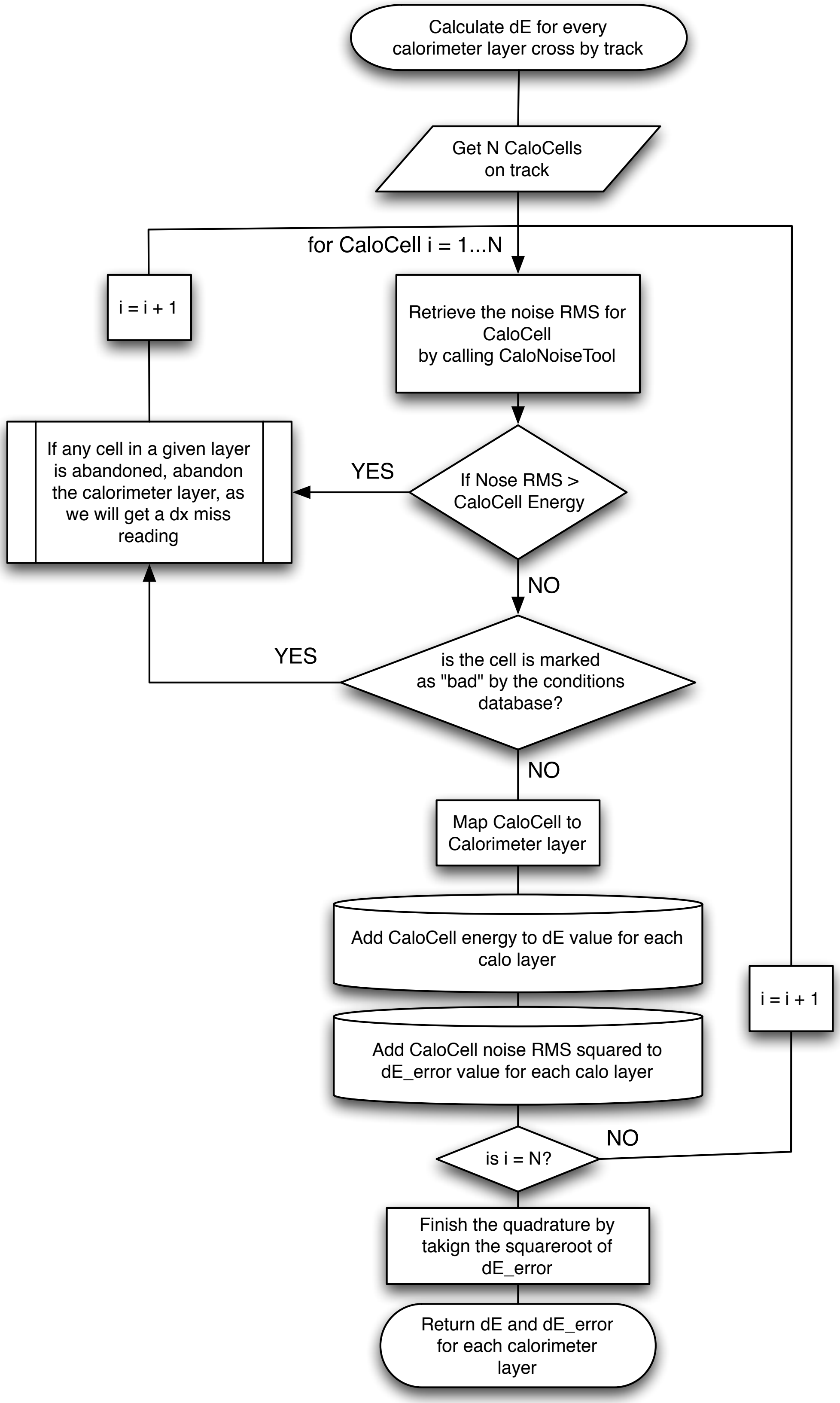

8

Mass estimation

In a search for new massive particles, estimating the mass is of obvious importance. Mass is fundamentally related to particle energy and momentum by $m^2 = E^2 - p^2$. By measuring the energy and momentum it is possible to estimate the mass. R-Hadrons are expected to pass through the detector, making the direct energy measurement impossible. Instead other relationships can be utilised. One of these methods relies on the idea that dE/dx is principally dependent on velocity. Velocity and momentum naturally is related to mass: $p = \gamma\ \beta\ m$, so by using the inverse function of dE/dx to find β, it is possible to estimated the mass of a slow moving particle.

To see this relationship we start by finding m in terms of $(\beta\gamma)^2$,

$$
\begin{aligned}
p &= \gamma\ \beta\ m \\
m^2 &= \frac{p^2}{(\gamma\beta)^2}
\end{aligned}
\tag{8.1}
$$

The Bethe-equation (eq. 7.1) is effectively a function of projectile velocity β:

$$\frac{dE}{dx} \sim \frac{1}{\beta^2}. \tag{8.2}$$

It is possible to combine eq. 8.1 and eq. 8.2 by simplifying $1/(\beta\gamma)^2$,

$$
\begin{aligned}
\frac{1}{(\beta\gamma)^2} = \frac{1}{\left(\frac{\beta}{\sqrt{1-\beta^2}}\right)^2} = \frac{1-\beta^2}{\beta^2} &= \frac{1}{\beta^2} - 1 \\
&\xrightarrow{\text{for } \beta \ll 1} \frac{1}{\beta^2} \\
\frac{1}{(\beta\gamma)^2} &\sim \frac{1}{\beta^2}
\end{aligned}
\tag{8.3}
$$

Using the similarity between eq. 8.3 and eq 8.2, we can express eq 8.1 in terms of dE/dx,

$$m^2 \sim p^2\ \frac{dE}{dx} \tag{8.4}$$

Equation 8.4 is only valid for $\beta \ll 1$, because of the approximation in eq. 8.3. This approximation translates to high dE/dx values. For particle identification this is not a limitation, as only slow moving particles can be discriminated, since most other particles moving at β close to 1 are minimum ionising at the LHC.

The full Bethe equation is not analytically invertible, and has to be either numerically inverted or simplified. For particle identification, the region of interest lies between $0.01 \lesssim \beta\gamma \lesssim 2.5$, this region is well described by the following relation (ref. [12]),

$$\frac{dE}{dx} \sim K\,\frac{m^2}{p^2} + C \tag{8.5}$$

where K and C are constants specific to the detector material. From figure 8.2 the relative difference between the Bethe function and equation 8.5 can be seen for the parameters estimated later in figure 8.5. An overall systematic error from the choice of fit function have been estimated to roughly 15%, in the $\beta\gamma$ interval relevant for mass estimation.

The difference between the full Bethe function and eq. 8.5 is illustrated in figure 8.1, where the two functions have been fitted to the same data sample, the relative difference for these curves is shown in figure 8.2.

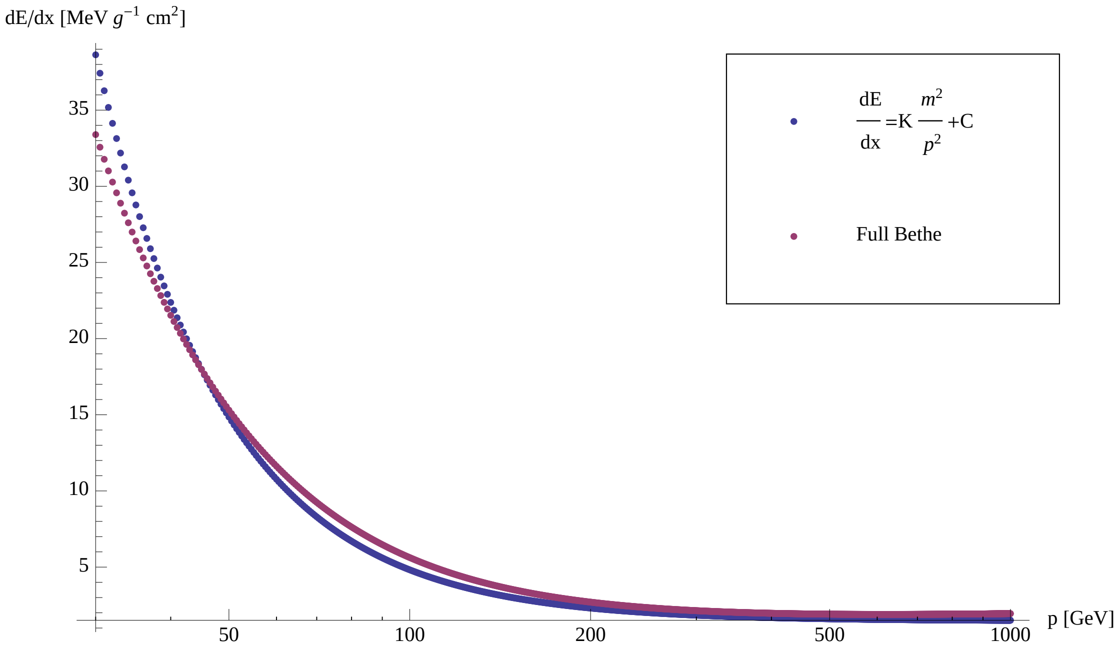

Figure 8.1: Equation 8.5 compared to the full Bethe function (eq. 7.1).

Solving equation 8.5 for m, gives an expression for the particle mass given its ionisation loss and momentum,

$$m \sim p\,\sqrt{\frac{dE/dx - C}{K}}. \tag{8.6}$$

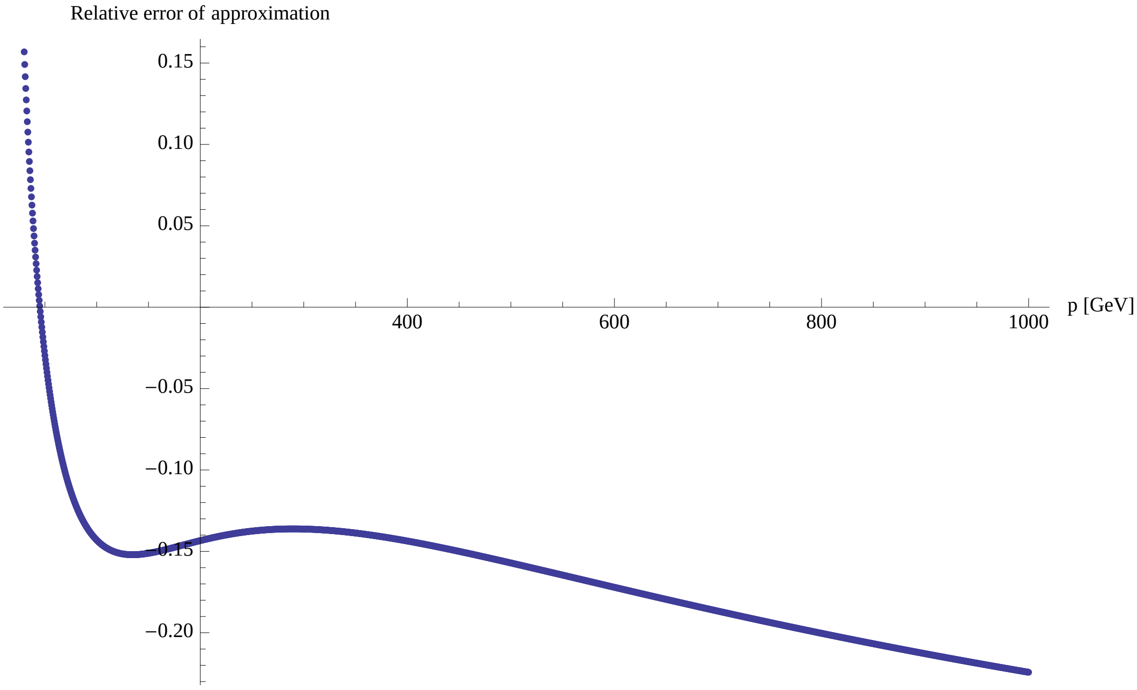

Figure 8.2: The relative error between the full Bethe relation and the approximation (eq. 8.5).

The following sections describe the calibration procedure used in determining the C and K constants for the different detector systems.

8.1 Mass constant calibration method

Determining C and K is done by fitting the 2-dimensional dE/dx vs momentum distribution. Fitting the 2D histogram directly is quite complicated, as most fitting routines regress to a fairly simplistic minimisation due to the $\mathcal{O}(N^2)$ input space. To circumvent this problem, the 2D distribution can be sliced into 1D histograms, by histogramming the values in a specific bin-range on one axis. This concept is illustrated in figure 8.3a and 8.3b.

The 1D histograms resulting from these slices are then in the opposing units of the axis where the slice has been place, see figures 8.3c and 8.3d.

In relation with particle identification by continuous energy loss, the rise on the Bethe-curve is of principal importance, the better description of this rise, the tighter the mass estimate. To capture the detail on both axes, the method used slices both the X and the Y axis. If we only sliced one axis, say along the momentum (X axis), then the region around 50GeV $< p <$ 150GeV in figure 8.3b would be badly described, given a finite number of slices, needed in view of the statistics available. When slicing along both axes, all ranges will be accounted for in an optimal way.

The number of slices on each axis determines the resolution on the final description of the Bethe-curve. In practice the amount of statistics available[1] in the histogram limits the number of slices to around 10 per axis. On each slice, a peak finder is used to find the most likely place of the band, these peaks are marked by a red triangle on figures 8.3c and 8.3d. The largest peak is then used as a seed mean value for the fit. The distribution is fitted with either a gaussian or a crystal ball function [44]:

$$f(x;\alpha,n,\bar{x},\sigma) = N \cdot \begin{cases} \exp(-\frac{(x-\bar{x})^2}{2\sigma^2}), & \text{for } \frac{x-\bar{x}}{\sigma} > -\alpha \\ A \cdot (B - \frac{x-\bar{x}}{\sigma})^{-n}, & \text{for } \frac{x-\bar{x}}{\sigma} \leqslant -\alpha \end{cases} \tag{8.7}$$

$A = \left(\frac{n}{|\alpha|}\right)^n \cdot \exp\left(-\frac{|\alpha|^2}{2}\right)$, $B = \frac{n}{|\alpha|} - |\alpha|$, N is a normalisation factor and α, n, $\bar{x}$ and σ are parameters which are fitted with the data.

If the fit fails to converge, or the width of the fitted distribution is larger than the RMS of the whole slice, then the mean value is estimated based on bin counting, and the error on the mean is taken to be RMS/$\sqrt{N}$ where N is the number of entries in the slice. If only one entry is present in the slice, the error is taken to be the standard deviation of a single bin[2] $1/\sqrt{12}$ [16].

The most probable values from each slice is then plotted on a graph, and fitted by equation 8.5, as illustrated in figure 8.4a. The resulting fit K and C parameters are used in equation 8.6 to estimate the mass, resulting in a mass distribution similar to the one in figure 8.4b.

8.2 Calibration results

The mass estimators for pixel, LAr 1, LAr 2 and the presampler have been calibrated by applying the method described in section 8.1 to the ten R-Hadron signal samples. The choice of calibrating on monte carlo samples is in principle troublesome as badly described real world effects can contribute to both the momentum and the dE/dx estimates. For all but the pixel detector, this choice is simply dictated by the lack of any known particle that can produce a low-β dE/dx raise. In all the detectors R-Hadrons can be double charged. In the mass calibration a single band is required. To help the calibration tool, a region of interest is defined around the main band, allowing only the entries within this area to contribute to the calibration fits (indicated by the red band in figure 7.10). In principle, this type of geometrical cut can introduce a bias, as the overall distributions in the slices tend to be shifted in one direction, if the region contains slight asymmetries from the definition of the region The bias is minimised by the fit selection requirements in section 8.1, but particularly the case where the fit doesn't converge, and more than 1 entry is present in a slice can be problematic in this case. An example of the distribution after cleaning is found in figure 8.5. The overall mass bias is discussed later in this section.

[1] See section 6.4 for monte-carlo production details

[2] Assuming a uniform distribution

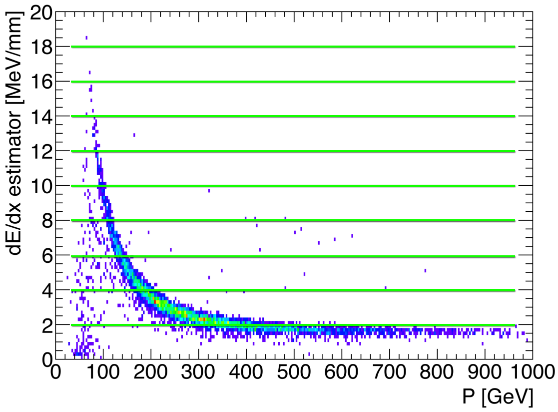

(a) Momentum estimation by horizontal slices at known dE/dx values. For this mass hypothesis, a valid range would be from dE/dx $\gtrsim$ 4.0 MeVg^{-1}cm^2.

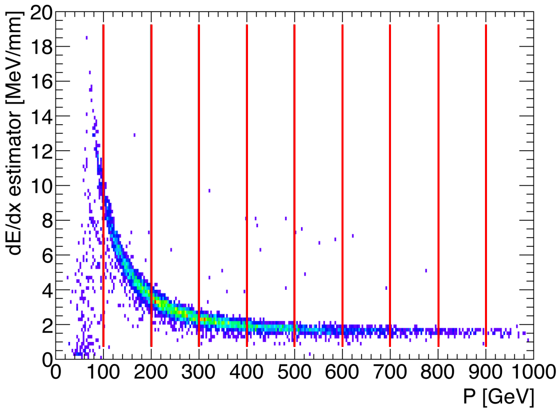

(b) dE/dx estimation by vertical slices at known momenta. For this mass hypothesis, a valid range would be from p $\gtrsim$ 300 GeV.

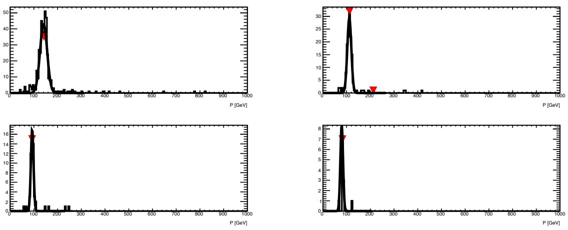

(c) Slices along the Y-axis (dE/dx), each histogram corresponds to a slice along a green line in figure 8.3a.

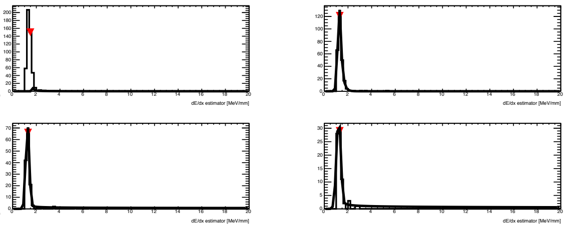

(d) Slices along the X-axis (momentum), each histogram corresponds to a slice along a green line in figure 8.3b.

Figure 8.3: 2D histogram fitting by slicing along both axes.

All the signal samples have been cleaned for other particles caused by initial state radiation, by requiring them to be labeled as 'R-Hadron' by the event generator. True momentum is used.

For each of the detector systems, the constants K and C have been found, for all the signal samples, and is plotted in figure 8.10. The constants for the third layer and the three tile layers in the hadronic calorimeter have been estimated as well, but they have proved unsuitable for mass estimation, based on the calibration results.

For each calorimeter layer, the calibration pairs (K,C) from each mass hypothesis is combined by calculating the weighted mean with the error on the constants as weight,

$$\langle K \rangle = \frac{\sum_i \left(K_i / \sigma_{K_i^2} \right)}{\sum_i \frac{1}{\sigma_{K_i^2}}}. \tag{8.8}$$

The error of the weighted mean is,

$$\frac{1}{\sigma_K^2} = \sum_i \frac{1}{\sigma_{K_i^2}}. \tag{8.9}$$

The weighted means are listed in table 8.1.

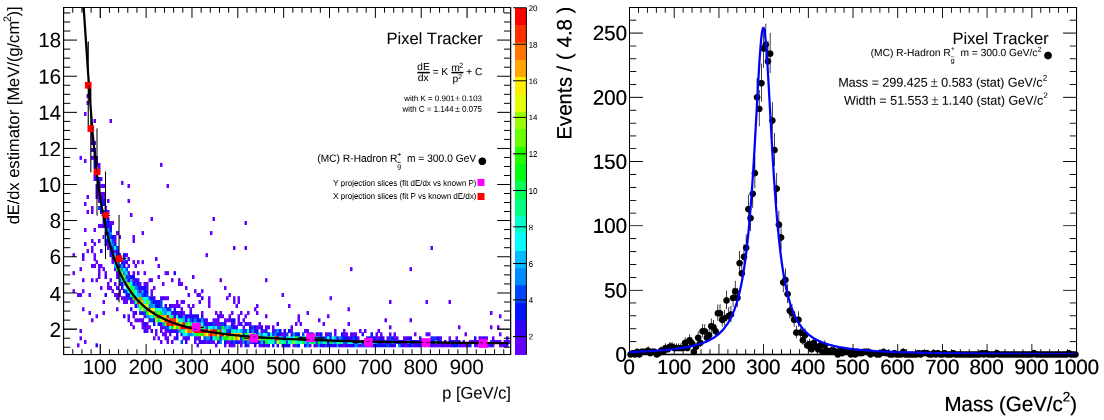

(a) dE/dx fit.

(b) Breit–Wigner fitted to the mass distribution for 300GeV R-hadrons.

Figure 8.4: In (a) the coloured squares (pink and red), mark the most probable values found by fitting slices. The fit of equation 8.5 to these points is marked by the black line. Figure 8.4b: The mass estimate is found using equation 8.6.

	$\langle C \rangle$	$\langle K \rangle$
Presampler	0.895 ± 0.067	0.204 ± 0.004
LAr 1	0.525 ± 0.045	0.288 ± 0.022
LAr 2	0.434 ± 0.058	0.278 ± 0.032
Pixel	1.464 ± 0.061	0.905 ± 0.031

Table 8.1: Calibration results for for the mass estimators.

Mass reconstruction performance

The calibration constants found, have been integrated into the NTuple software, enabling mass estimation for all slow moving particles. To gauge the performance of the mass estimators, the bias with respect to the true mass is calculated. The bias is found by histogramming the reconstructed mass minus the true mass (figure 8.8). The histogram is then fitted with a Breit-Wigner function [25], and the bias is estimated to be the mean value found by this fit.

Bias and mass resolution

Looking at the relative mass resolutions listed in table 8.2, it is noticeable that the momentum resolution (figure 6.3 in chapter 6.9) is dominating the mass resolution when using reconstructed momentum. When using the true momentum, the mass resolution becomes better at increasing masses, as we would expect since a larger part of the data points lies on the low-β rise, compared to the lower masses, where a substantial amount of the data lies close to the MIP region.

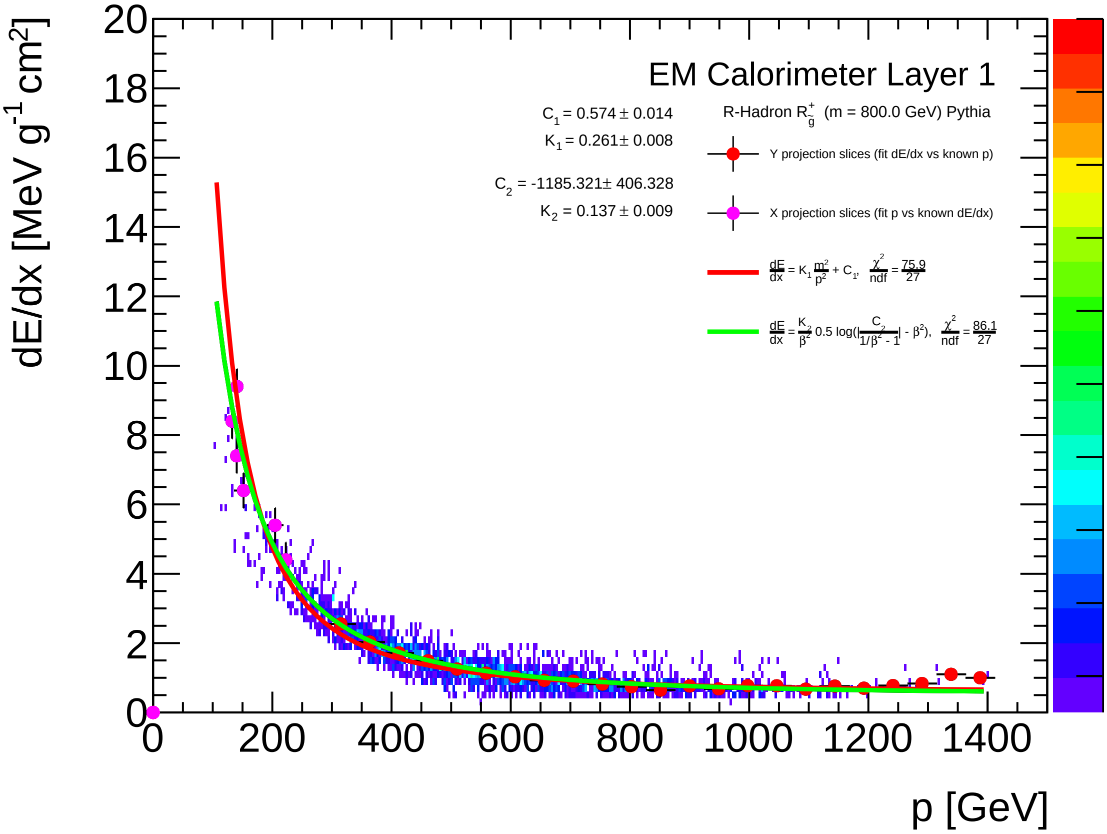

Figure 8.5: Fit result from a cleaned R-Hadron sample with a mass of 800 GeV. The red curve is the dE/dx fit employing eq. 8.5 and the green curve is the full Bethe function for comparison.

The bias from the true mass is growing as masses increase, independently of momentum. In figure 8.6 the absolute value of the bias for reconstructed momentum (red dots) is plotted together with the bias assuming true momentum (green dots). The increased rate of the rise in bias with reconstructed momentum could hint at a possible correlation between the two errors, which could be expected from the choice of dE/dx function, as figure 8.2 show a clear discrepancy between the theoretical predicted energy loss as a function of momentum and the applied model. Furthermore, we would expect some variation in the overall functional description with respect to mass, as the expression is sensitive at the onset of the low-β rise due to the lack of a logarithmic term found in the Bethe equation.

The bias have been calculated using mass estimates with true (figure 8.9) and reconstructed momentum. The resulting shifts are listed in table 8.2 for the pixel mass estimator and in table 8.3 for the first layer in the electromagnetic calorimeter.

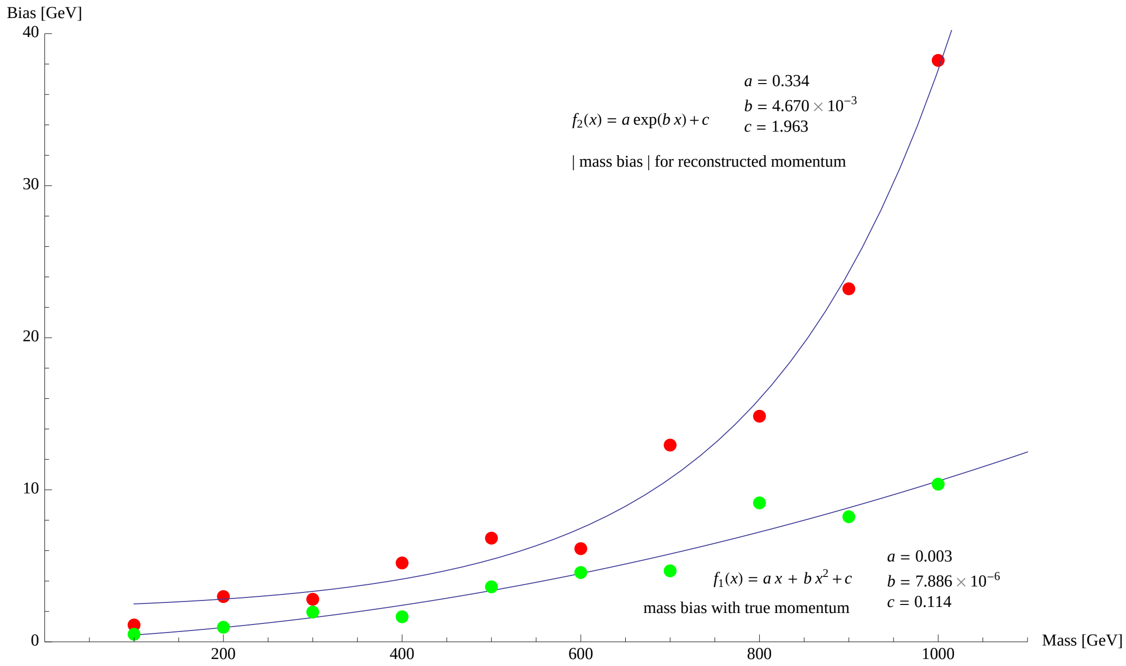

Figure 8.6: Evolution in bias as a function of R-Hadron mass.

Mass estimation in the pixel detector of low-p_T Standard Model particles.

The mass estimator has been tested against collision data from the minimum bias data stream. This data is mainly dominated by low energy particles, making it suitable for particle identification purposes with the dE/dx method. In figure 8.16 the inlayed 2D histogram shows the dE/dx vs momentum distribution utilised for mass estimation. The black line represents a cut on the dE/dx value, excluding minimum ionising particles. In

Mass [GeV]	Bias [GeV] $m_{est} - m_{true}$	Bias [GeV] $m_{est_{true_p}} - m_{true}$	Mass resolution $\sigma_m = \frac{m_{est}-m_{true}}{m_{true}}$	Mass resolution $\sigma_m = \frac{m_{est_{true_p}}-m_{true}}{m_{true}}$
100	−1.11	0.50	13.91 %	13.32 %
200	−2.98	0.96	13.49 %	11.65 %
300	−2.80	1.96	13.59 %	10.53 %
400	−5.19	1.65	14.12 %	9.56 %
500	−6.82	3.62	15.72 %	9.13 %
600	−6.13	4.56	16.09 %	8.48 %
700	−12.94	4.67	16.67 %	8.02 %
800	−14.84	9.14	17.47 %	8.02 %
900	−23.22	8.23	18.69 %	7.44 %
1000	−38.24	10.37	20.03 %	7.54 %

Table 8.2: Bias and mass resolution for the pixel detector. Errors on the mean can be found in figures 8.9 8.8 8.11 8.12.

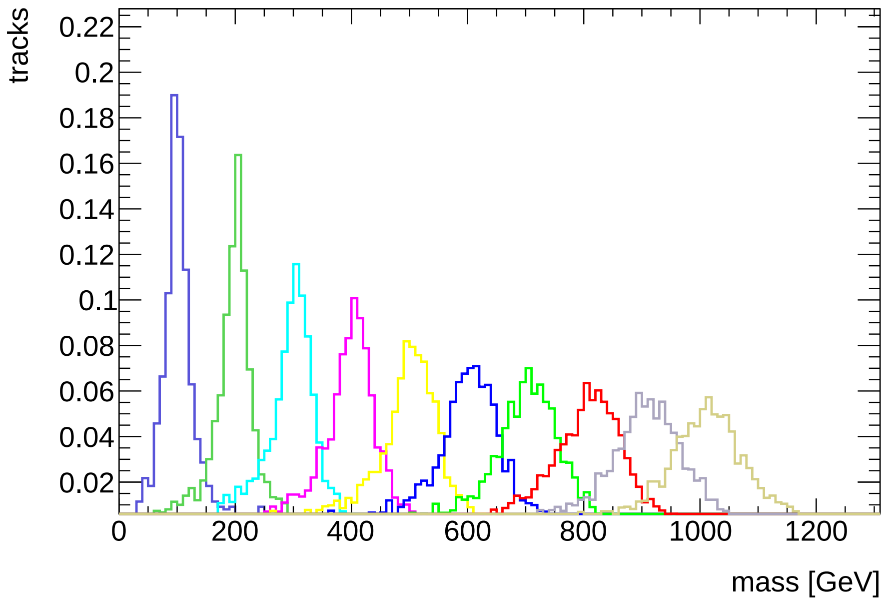

Figure 8.7: Mass estimation based on pixel dE/dx. R-Hadron masses plotted assuming true momentum.

Mass [GeV]	Bias [GeV] $m_{est} - m_{true}$	Bias [GeV] $m_{est_{true_p}} - m_{true}$	Mass resolution $\sigma_m = \frac{m_{est} - m_{true}}{m_{true}}$	Mass resolution $\sigma_m = \frac{m_{est_{true_p}} - m_{true}}{m_{true}}$
100	27.63	32.00	24.55 %	27.86 %
200	31.22	32.73	25.02 %	27.26 %
300	28.61	30.55	22.04 %	19.86 %
400	28.07	29.70	22.18 %	19.52 %
500	29.69	27.56	24.30 %	18.95 %
600	28.59	26.33	24.87 %	18.71 %
700	31.23	28.01	28.64 %	18.07 %
800	16.64	20.54	25.41 %	16.93 %
900	7.26	28.55	31.38 %	17.27 %
1000	−7.32	31.73	26.38 %	16.49%

Table 8.3: Bias and mass resolution for the electromagnetic calorimeter layer 1.

the mass plot, pions, kaons, protons and deuterons are visible. The asymmetry between positive and negative charged deuterons are clearly visible in both plots. The vertical lines on the mass plot represents the true masses of the particles. The offset from the true masses are caused by two effects. The first is the fact that the mass estimator has been calibrated on R-Hadrons with a simplified ionisation model. The second is a bit more subtle. Particle tracks are by default assumed to be pions during the track reconstruction. This affects the momentum measurement markedly at low p_T, as energy loss, multiple scattering and other material effects become important when $m/p \to 1$. Nevertheless, this plot is a sanity check for the mass estimator.

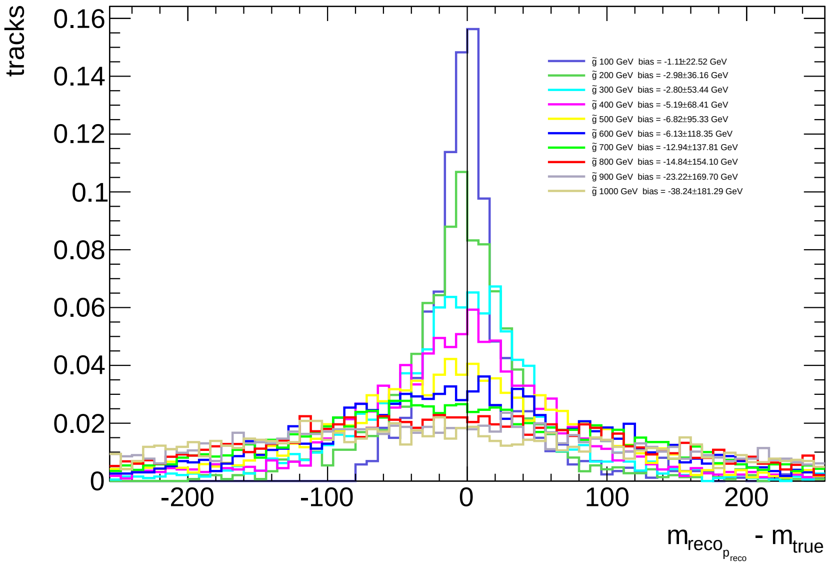

Figure 8.8: Bias in the pixel mass estimate.

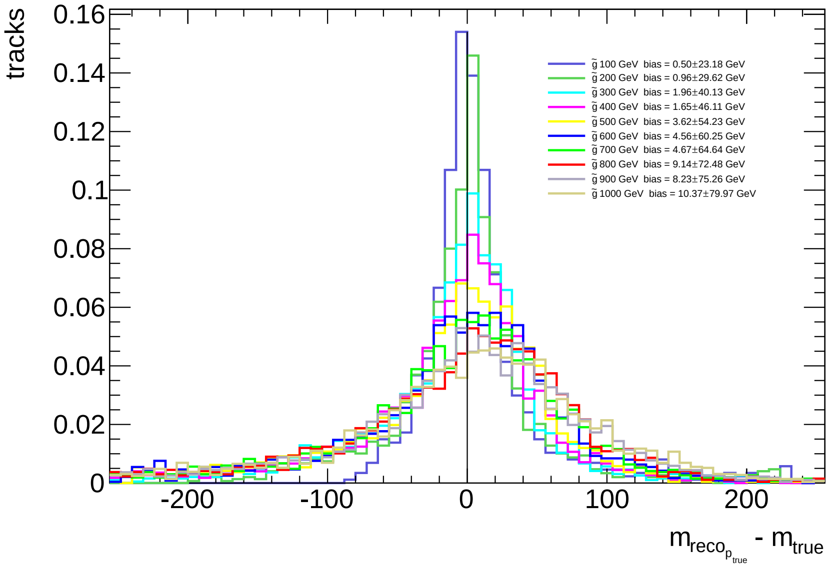

Figure 8.9: bias in the pixel mass estimate, mass estimated with true momentum.

Figure 8.10: Mass estimator constants.

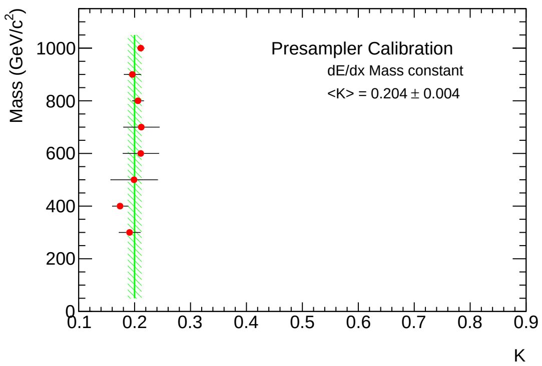

(a) Presampler.

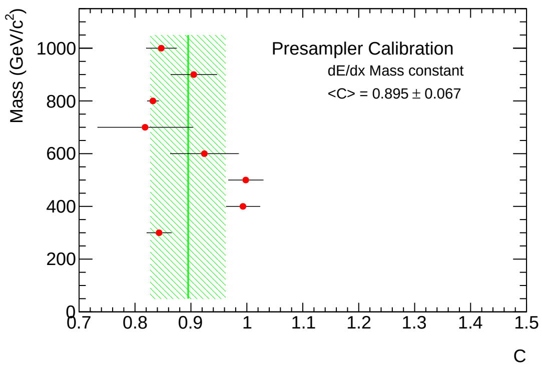

(b) Presampler.

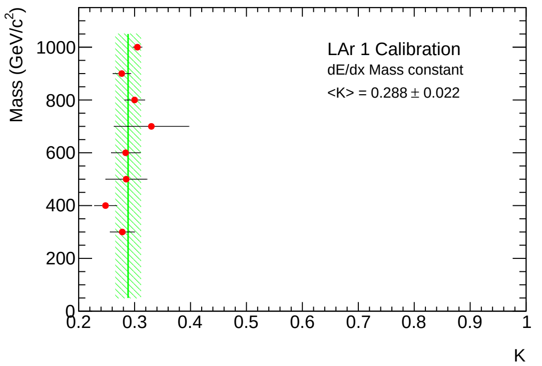

(c) LAr 1.

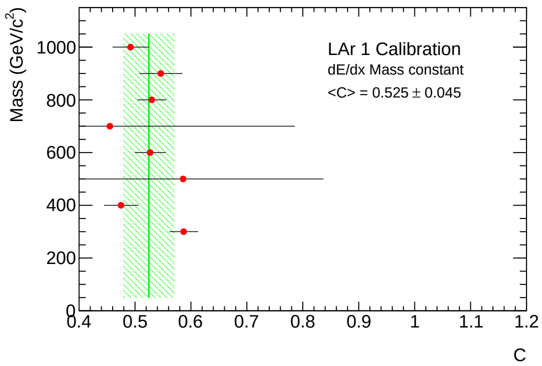

(d) LAr 1.

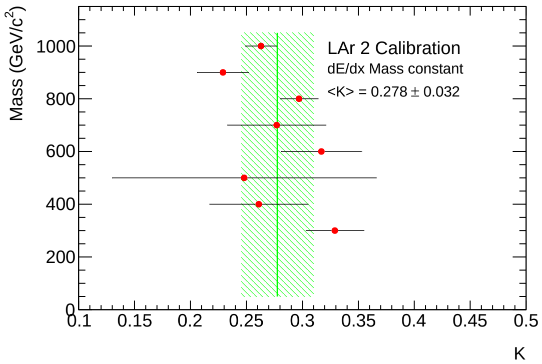

(e) LAr 2.

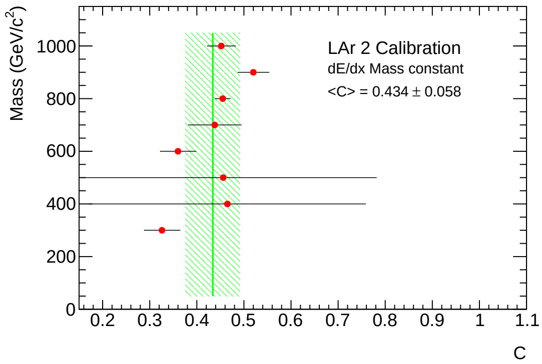

(f) LAr 2.

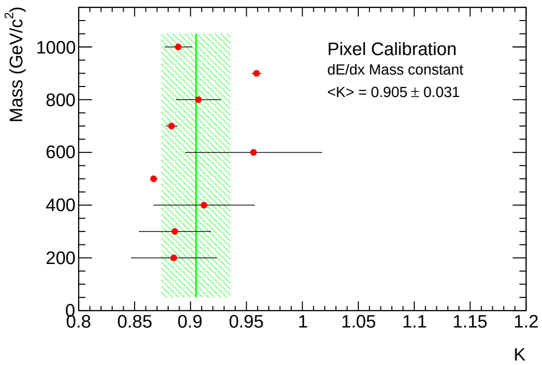

(g) Pixel.

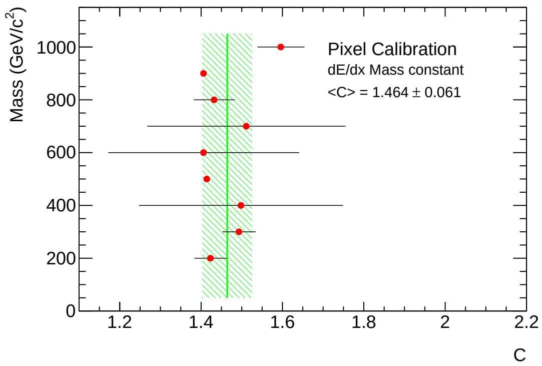

(h) Pixel.

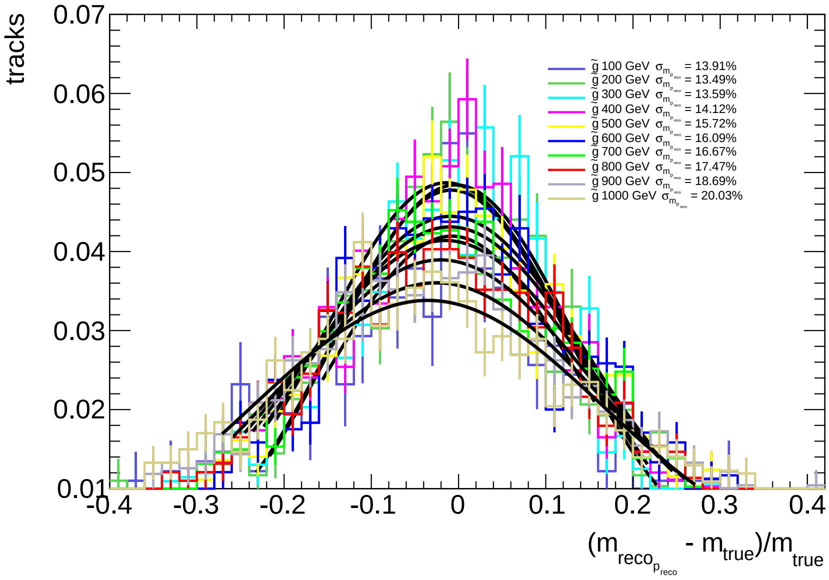

Figure 8.11: Resolution of the pixel mass estimator (reconstructed momentum).

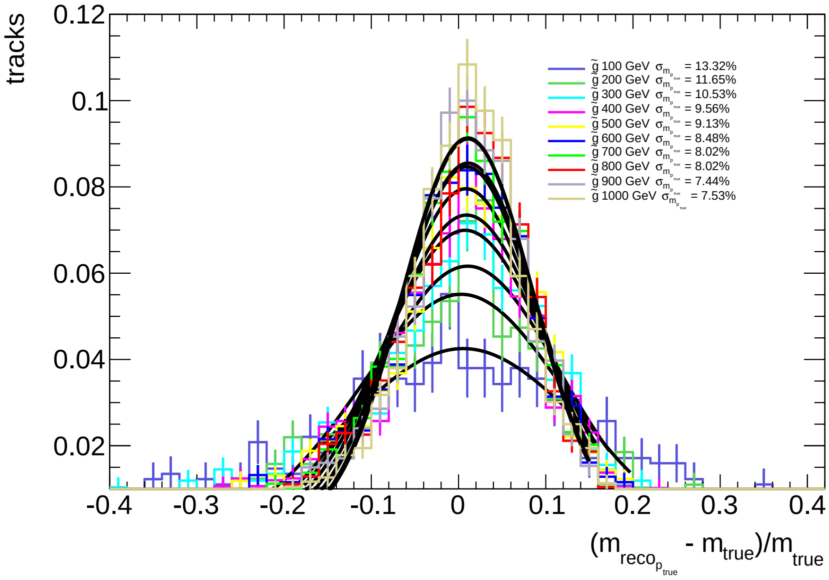

Figure 8.12: Resolution of the pixel mass estimator (true momentum).

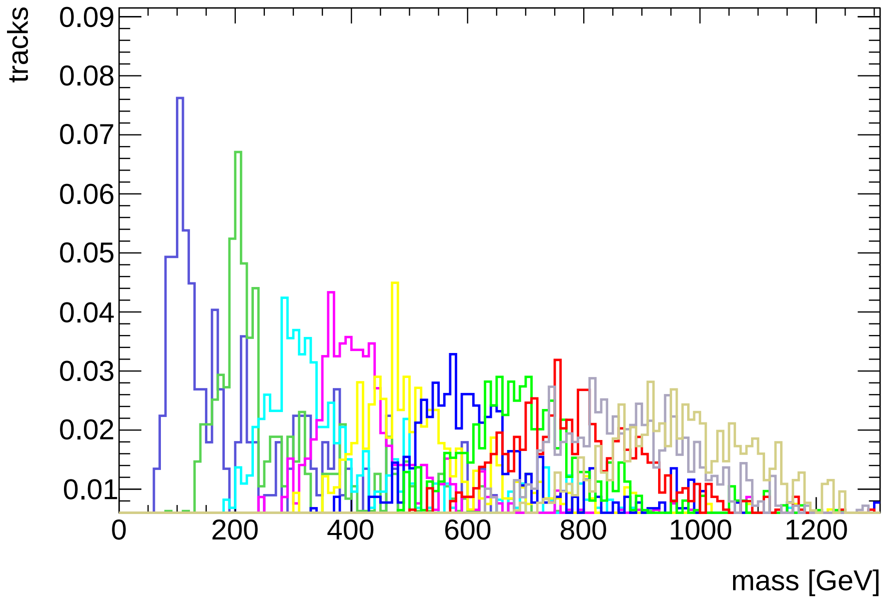

Figure 8.13: Presampler mass reconstruction of signal samples (true momentum).

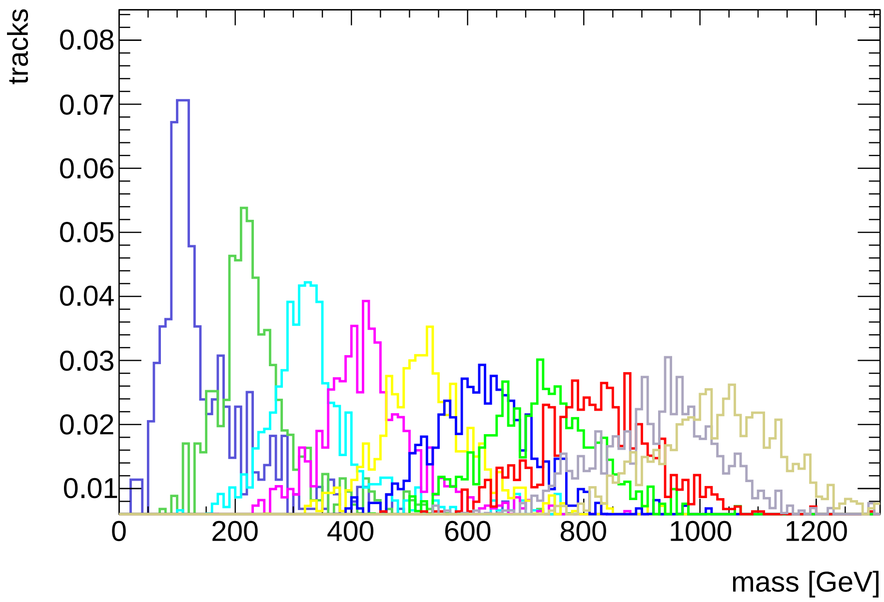

Figure 8.14: Electromagnetic calorimeter layer 1 mass estimates (true momentum).

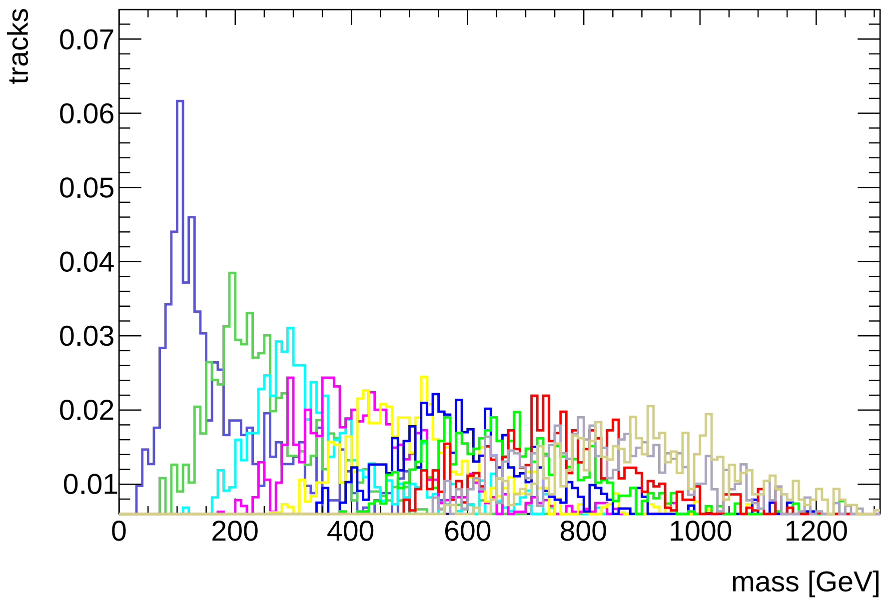

Figure 8.15: Electromagnetic calorimeter layer 1 mass estimates (reconstructed momentum).

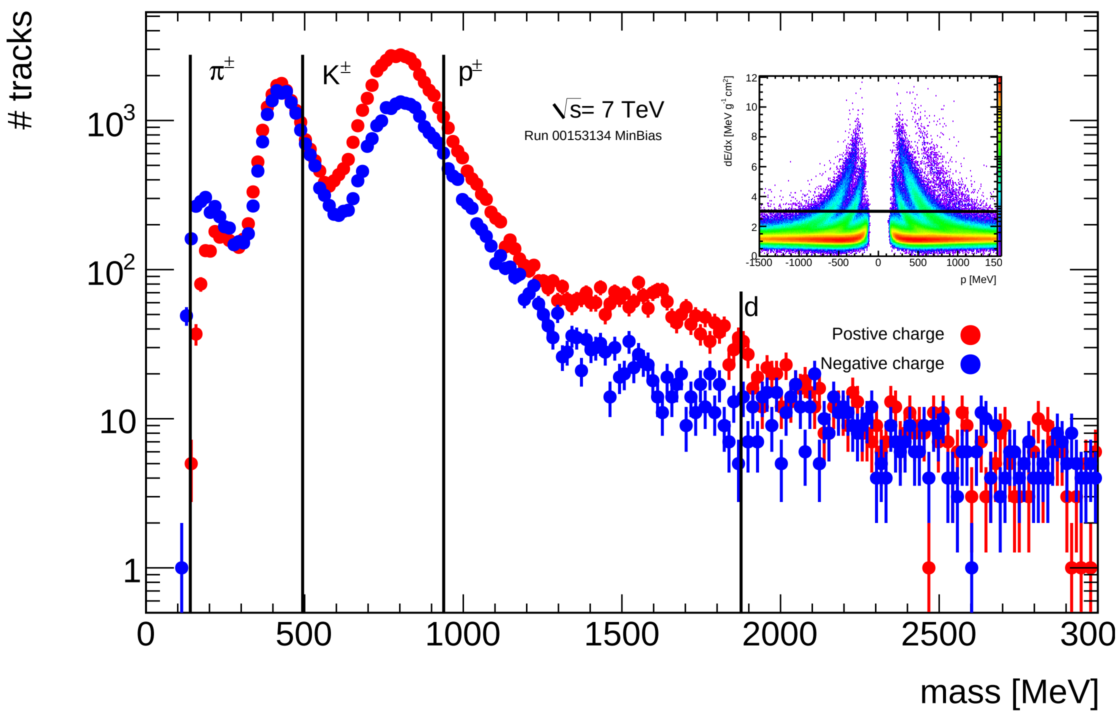

Figure 8.16: Real data. Pixel mass minimum bias sample. Requires a dE/dx value ≥ 2.4, at least 3 pixel hits, and more than 6 SCT hits.

Part IV

Analysis

9

Analysis

In order to postulate anything about the possible existence of R-Hadrons, a statistical analysis is performed. The analysis can be described as a counting experiment. The principle is simple, we define a region in parameter-space where we expect a specific amount of counts from background processes, and a sizeable addition from a possible R-Hadron signal. If, when comparing to data, there is a significant discrepancy between expected background and the observed number of events, we can claim a discovery. If instead, observation and expected background coincide with no significant deviation, a limit can be placed on the R-Hadron production cross section.

Before the counting itself, the area of interest in the parameter space is defined. The parameter space is comprised of every observable available after event reconstruction: track momentum, direction, energy depositions, particle identification variables such as mass and velocity among others.

For this search a subset of the available parameters is extracted based on signal significance, 'cuts' defining the effective ranges of the parameters are found by optimising the specific signal significance for each variable in turn, this process will be described in section 9.3.

9.1 Preselection

Before the analysis a preselection is applied to ensure the quality of the reconstructed tracks.

The preselection cuts are chosen based on advice from the muon combined performance group, inner tracking Combined Performance Group and lastly by cut optimisation using simulated annealing.

Event level requirements

- The event must pass the *xe40_noMu* trigger chain (sec. 6.3).
- Real data events must pass the SUSY working group good run list (sec. 6.6).
- Real data must pass the OTX data quality map (sec. 6.6). Correspondingly monte carlo events are scaled by the efficiency loss to compensate.
- Real data from multiple data streams have overlapping events removed (sec. 6.6).
- Each event is required to have at least one vertex with three associated tracks.

Track level requirements

- Require at least 3 hits in the pixel detector (minimum requirement for the pixel dE/dx observable).
- At least 5 hits in the Semiconductor tracker.
- 0 pixel clusters shared with other tracks.
- 0 SCT hits shared with other tracks.
- Transverse impact parameter $|d_0| < 2.0$ mm and Longitudinal impact parameter $z_0 < 10$ mm.

The overall preselection efficiencies are listed in table 9.3.

9.2 Selection variables

In part III of this thesis 7 independent dE/dx estimators where developed. In addition to the Calorimeter dE/dx variables, it is also possible to measure dE/dx in the pixel detector. Furthermore, a Time-of-Flight (ToF) observable utilising the hadronic calorimeter timing has been constructed by other members of the ATLAS SMP group [23]. By combining any of these variables with momentum, a mass estimate can be calculated. Beyond the special purpose estimators, a selection of standard observables is included in the event selection.

In all, the following variables are available for event selection:

Custom observables

- Calo dE/dx LAr layer 0
- Calo dE/dx LAr layer 1
- Calo dE/dx LAr layer 2
- Calo dE/dx LAr layer 3
- Calo dE/dx Tile layer 1
- Calo dE/dx Tile layer 2
- Calo dE/dx Tile layer 3
- Pixel dE/dx
- Calo ToF β Tile
- (Mass estimates from all of the above)

General observables

- Transverse momentum (p_T)

- Distance to nearest jet (ΔR_{jet})
- Missing transverse energy ($E_{\mathrm{T}}^{\mathrm{miss}}$)

Not all the available observables are needed in the analysis, selecting the optimum combination is done by sorting them by significance, estimator efficiency and correlations.

Time of Flight

At readout level every cell in the hadronic calorimeter estimates the energy deposition by fitting the pulse shape of the electronic signal. The pulse is sampled at seven points S_i each spaced by 25 ns. The time t_{reco} is defined as the point where the pulse peaks on the time axis. A particle moving at light speed is defined to have $t = 0$. As particles are assumed to travel at light speed in ATLAS, the fit function is optimised around that value. In order to use the timing measurement for slow moving particles, alternative algorithms have been implemented. [23].

Converting the time signal to β is done by,

$$\beta_{cell} = \frac{v}{c} = \frac{d_{cell}}{t_{reco}c + d_{cell}} \tag{9.1}$$

where d_{cell} is the distance from the interaction point to the centre of the calorimeter cell.

For multiple cell hits a weighted mean is computed weighted by the cell energy.

The particle mass is then trivially computed by,

$$m = \frac{p}{\beta c}. \tag{9.2}$$

The β measurements for signal, background and data is plotted in figure 9.1 before any cuts have been applied.

Distance to nearest jet

R-Hadrons produced at the LHC are due to their high rest mass not likely to be created together with high-E_T jets. The distance between R-hadron candidate tracks and the nearest jet is thus a powerful discriminator against QCD jets, produced in abundance at the LHC. The distance is calculated by looping over every jet container in the event, while calculating the distance. The distance is calculated in η–ϕ:

$$\Delta R_{jet} = \min_i \sqrt{(\eta_{track} - \eta_{jet_i})^2 + (\phi_{track} - \phi_{jet_i})^2}. \tag{9.3}$$

ΔR_{jet} for each mass hypothesis as well as total background and data is shown in figure 9.2. The correspondence between background and data is within expectations, as fluctuations in the QCD samples are unavoidable due to low monte carlo statistics.

Transverse momentum

The transverse momentum depicted in figure 9.3 show a reasonable good agreement between background and data at low p_T. At high values the background estimate suffers from low statistics.

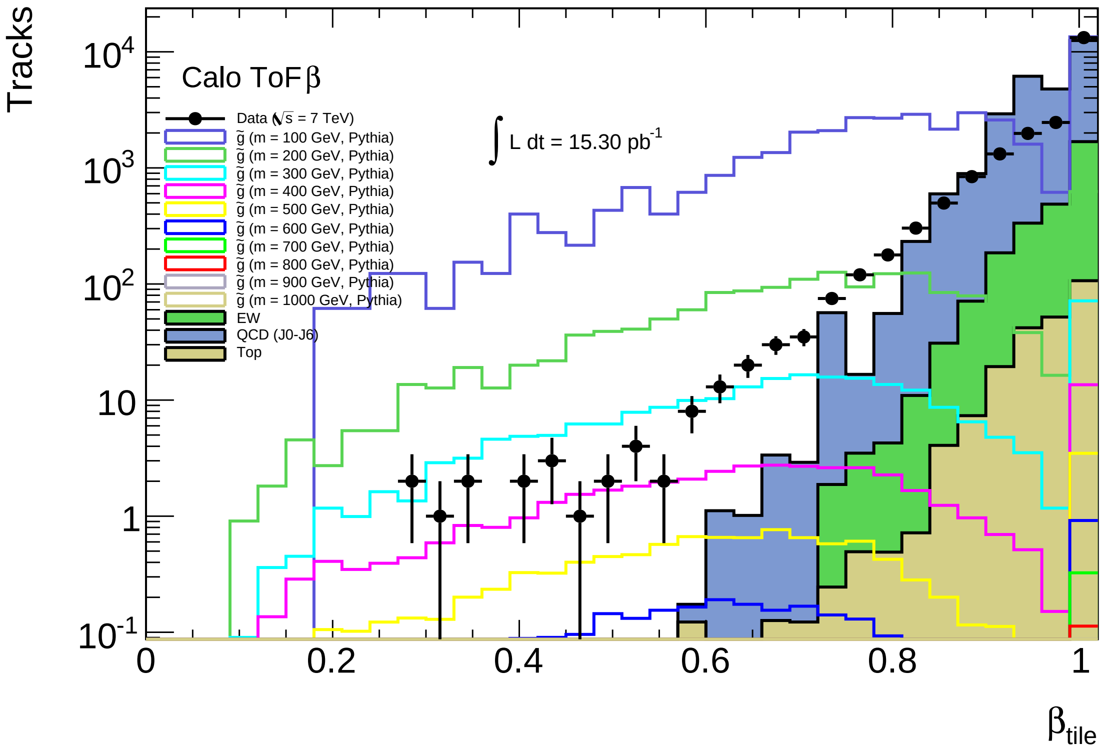

Figure 9.1: Tile of flight β estimated from tile.

dE/dx variables

The dE/dx variables all show good agreement between expected background and data. The signal samples in figure 9.4a show a known discrepancy with both the background and data. The MIP peak is shifted towards a slightly higher value. This shift has been found to be caused by the ionisation model in Geant4. The signal samples have been produced with a simplified model that ignores certain types of electromagnetic interactions. In later work this problem have been corrected, but at the time of writing the new signal samples where unavailable.

The consequence of the shifted dE/dx spectrum is increased acceptance, in this analysis this is compensated by increasing the systematic uncertainty on the signal count.

Mass variables

The mass resolution is largely dependent upon the momentum resolution. In section 6.9 we found a gradual uncertainty on the reconstructed momentum approaching 20 % for 1000 GeV R-Hadrons. This uncertainty is reflected in the mass distributions, especially comparing the pixel mass spectrum in figure 9.6a with the same masses, but with true momentum, in figure 8.7.

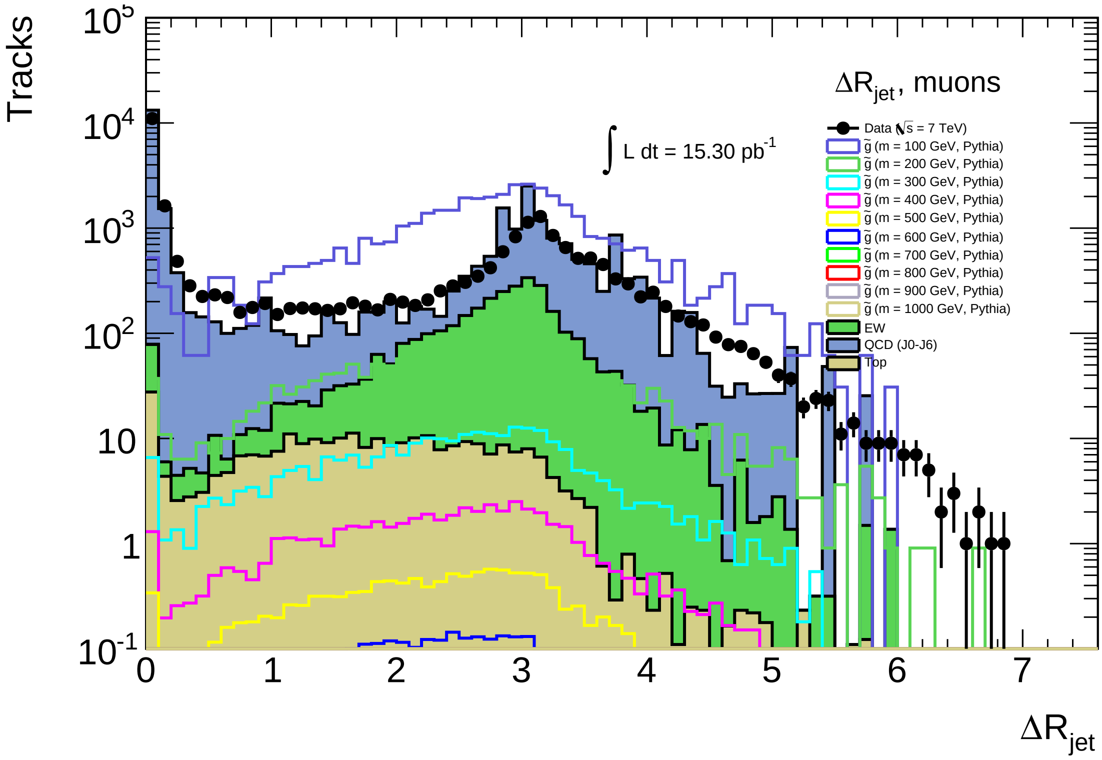

Figure 9.2: Distance to the nearest jet in η–ϕ of the R-hadron candidate track.

Correlations

To discriminate between signal and background, it is important to require the right combination of discrimination power and signal efficiency. If any of the chosen variables are strongly correlated in both signal and background they represent the same discrimination power, but potentially decreasing the signal efficiency, by requiring two or more measurements where only one is needed. In this analysis we expect all the observables to be correlated for the signal in some way. A particle with a low β will also ionise more leading to correspondingly higher dE/dx values. For the calorimeter dE/dx variables the energy depositions should be strongly correlated between the calorimeter layers, but uncorrelated for most of the background apart from muons. In figure 9.8 the correlations between the chosen variables is visualised by colouring the correlation matrix according to the correlation strength between each set of variables.

The variables are largely uncorrelated for the background samples, and moderately correlated for the signal samples.

Estimator efficiencies

The custom estimators are not always available for any given R-hadron candidate track. When choosing the estimators based on their significance it is important to realise that a highly significant estimator can cause efficiency loss if its rarely available for the signal candidate.

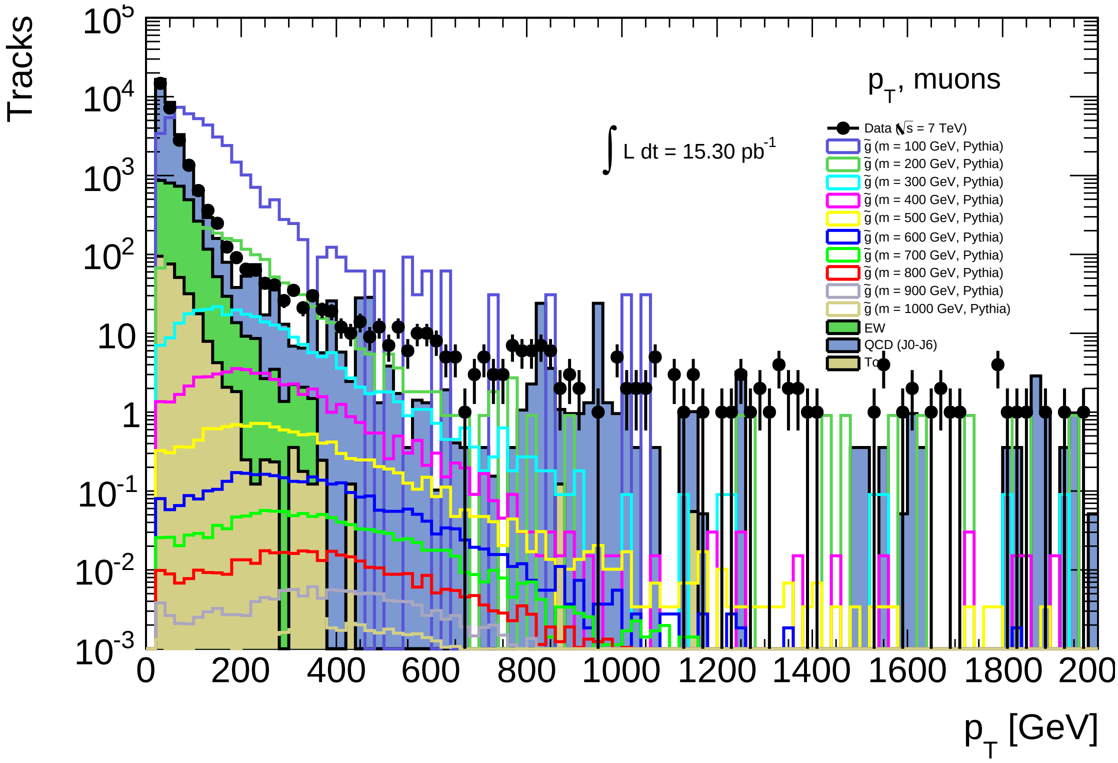

Figure 9.3: p_T

9.3 Choice of variable cuts

In terms of statistics, the goal of this analysis is to test if the R-Hadron hypothesis is true. The basic statistical framework for hypothesis testing is described in appendix A. In order to test the hypothesis a criteria defining what is R-Hadrons and what is not, must be constructed. Assume we only have a 1 dimensional distribution describing all the available information about the physics. The distribution must be based on an estimator that maximises the difference between signal and background as much as possible, such as the dE/dx estimators developed earlier. With such a distribution it is meaningful to ask which values to expect from signal and which from background. By defining an 'acceptance' region where we expect the background hypothesis to be true and a critical region where we expect the signal hypothesis to be true. Separating the distribution into these two regions is done by creating a decision boundary or 'cut', where if an observation falls on one side of the boundary it belongs to the signal hypothesis and if it falls to the other side, it belongs to the background hypothesis.

The optimal decision boundary for a simple 1d distribution can be found by deciding on a level of significance α (eq. 9.4) and then maximise the power $1-\beta$ (eq. 9.5). The significance is the probability that the background hypothesis falls within the critical

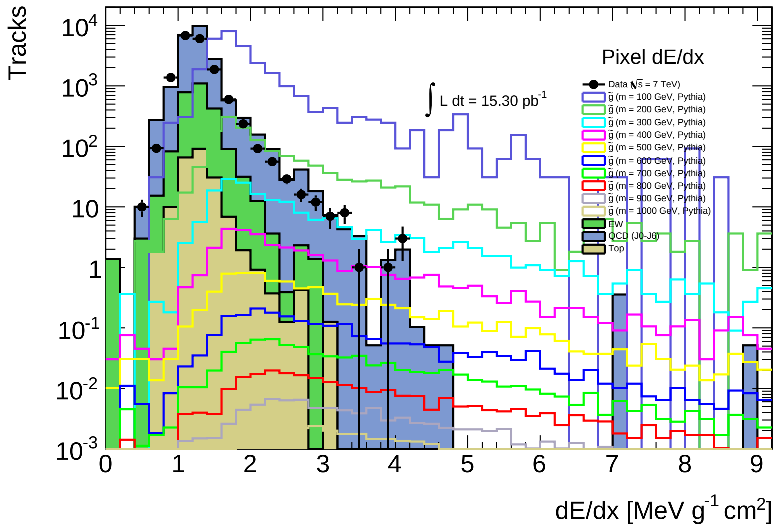

(a) Pixel dE/dx

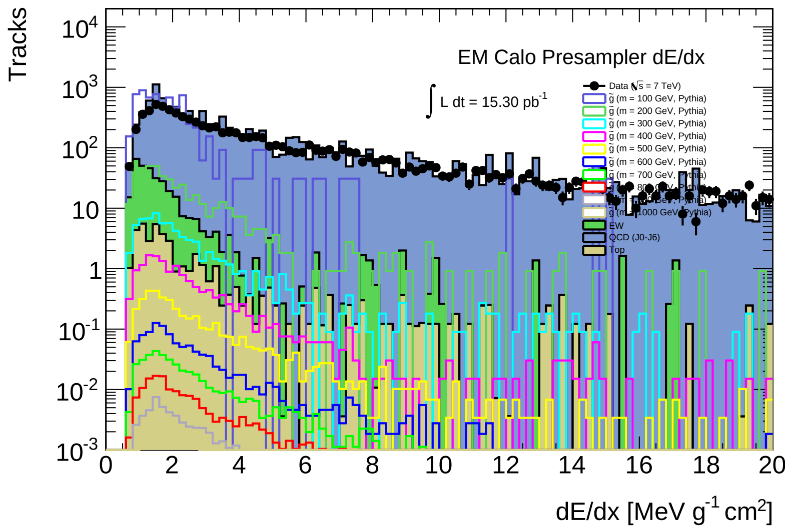

(b) Presampler dE/dx

Figure 9.4: dE/dx

region, and the power is the probability that the signal falls within the signal region,

$$\alpha = \int_{cut}^{\infty} f(X|bg)\ \mathrm{d}X \tag{9.4}$$

$$1 - \beta = \int_{cut}^{\infty} f(X|sig)\ \mathrm{d}X \tag{9.5}$$

These sizes are illustrated in figure A.1. The optimal way of creating a cut given these criteria is by calculating likelihood ratio $f(X|sig)/f(X|bg) \geq cut_\alpha$ where cut_α is chosen in a way that satisfies the significance requirement (9.4). If the ratio is larger than cut_α the signal hypothesis is chosen and if its smaller or equal to cut_α the background hypothesis

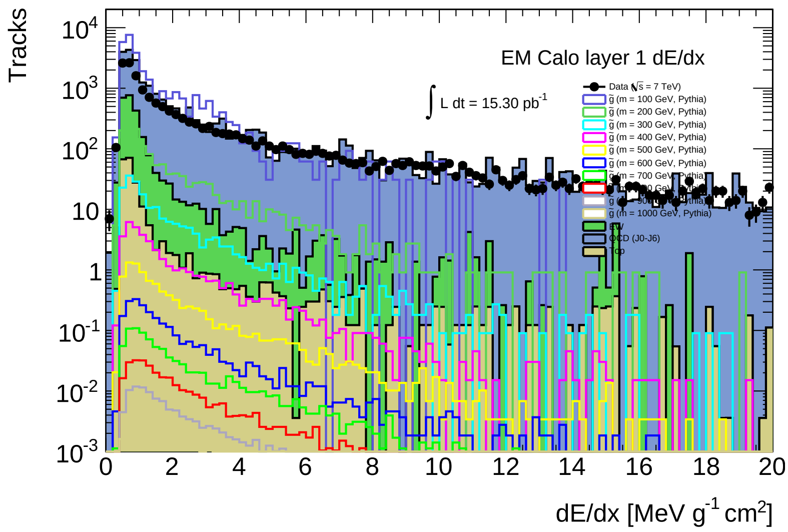

(a) LAr layer 1 dE/dx

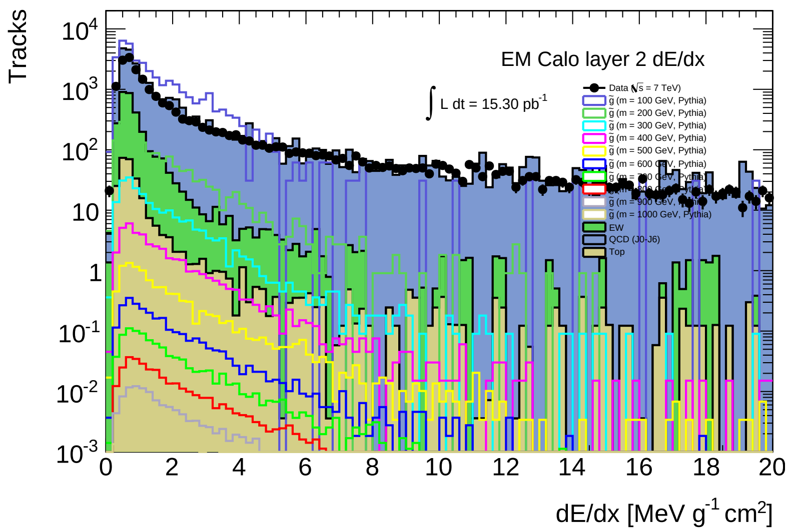

(b) LAr layer 2 dE/dx

Figure 9.5: dE/dx

is chosen. This construction is called the *Neyman-Pearson Test* [25], and produces the best test in the simple case of two completely specified distributions.

In practice this construction is impossible. The parameter space available in this analysis is 18 dimensional, and because of limited statistics it is not continuous and not likely to be completely specified. This dimensionality poses a practical problem, because of the 'curse of dimensionality'. If we were to place a decision boundary in this 18d space it would require a histogram containing the entire distribution. The required amount of memory would assuming single precision floating points, and 200 bins per axis would be around $(4 \times 200)^{18}$ bytes $\sim 10^{33}$ exabytes, slightly more than I have available in my computer! The distributions are not well described either, so any analytical expression is

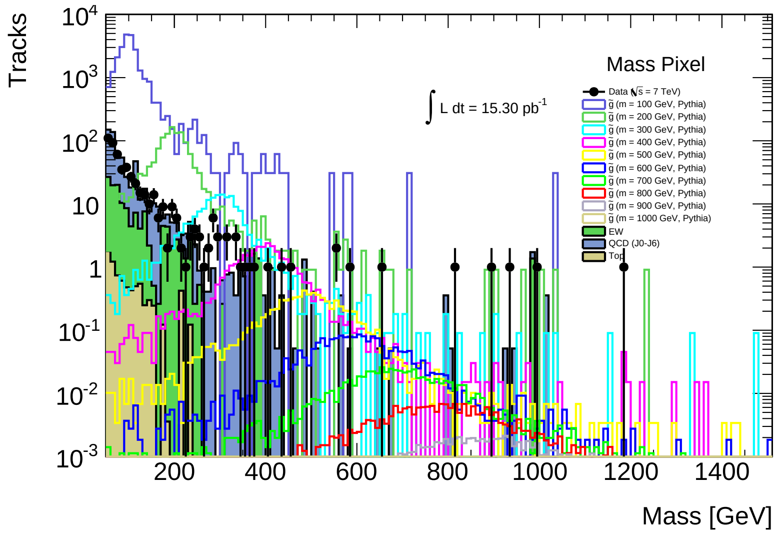

(a) Pixel dE/dx based mass

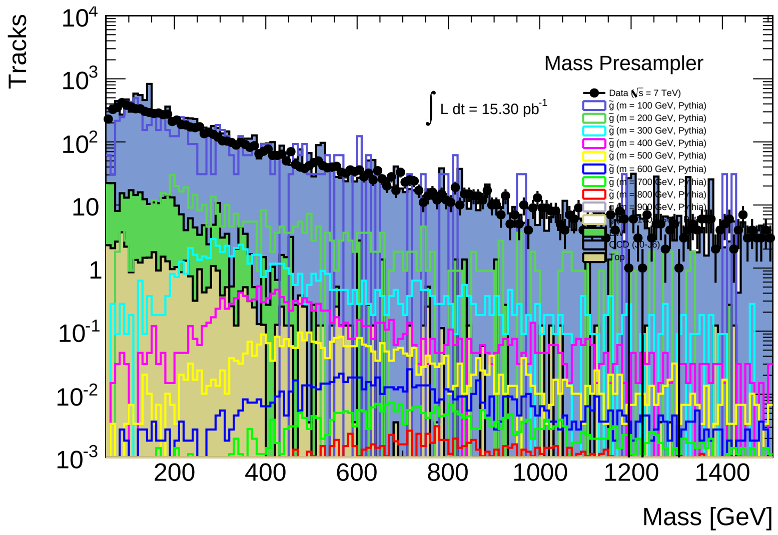

(b) Presampler dE/dx based mass

Figure 9.6: Mass estimators

excluded.

Numerous alternative methods have been developed during the last century, these multivariate methods are lossy optimisers based on heuristics inspired from a variety of fields such as neuroscience (neural networks), thermodynamics (Simulated Annealing) and genetics (Genetic Algorithms). While many of these methods have been tested as part of this work[1], the decision based on the availability of strong estimators is to approximate the Neyman-Pearson test by constructing a method that is based on 1 dimensional projections of the 20-space can estimate optimal decision boundaries.

---

[1]Simulated Annealing is used i the preselection, Boosted Decision Trees [7] have been investigated for the analysis, but failed to produce any significant improvement over the method described here.

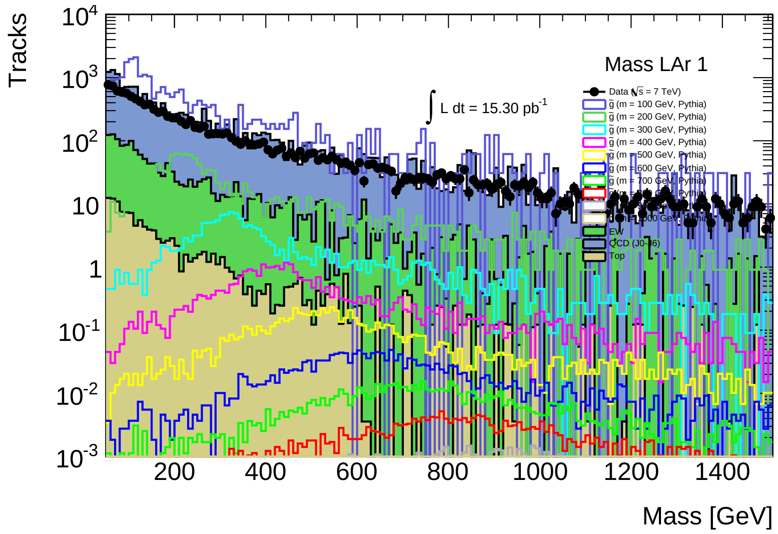

(a) LAr layer 1 dE/dx based mass

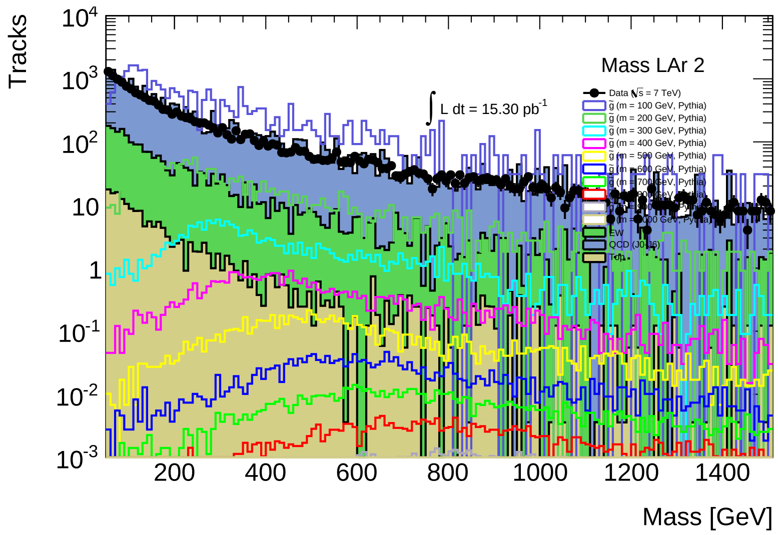

(b) LAr layer 2 dE/dx based mass

Figure 9.7: Mass estimators

Cut optimisation method

The optimisation routine is constructed to maximise the signal purity on single variables, the purity in this context can be defined by three distinct approximations, all of which are applied in parallel to gauge the optimal choice for the final cuts.

The three functions are all defined by the number of signal S and background B counts that passes the test statistic given a cut value, cut_i. The first (9.6) is a poissonian likelihood ratio construction,

$$p_{sLR} = \sqrt{2(S+B)\ln\left(1+\frac{S}{B}\right) - S} \tag{9.6}$$

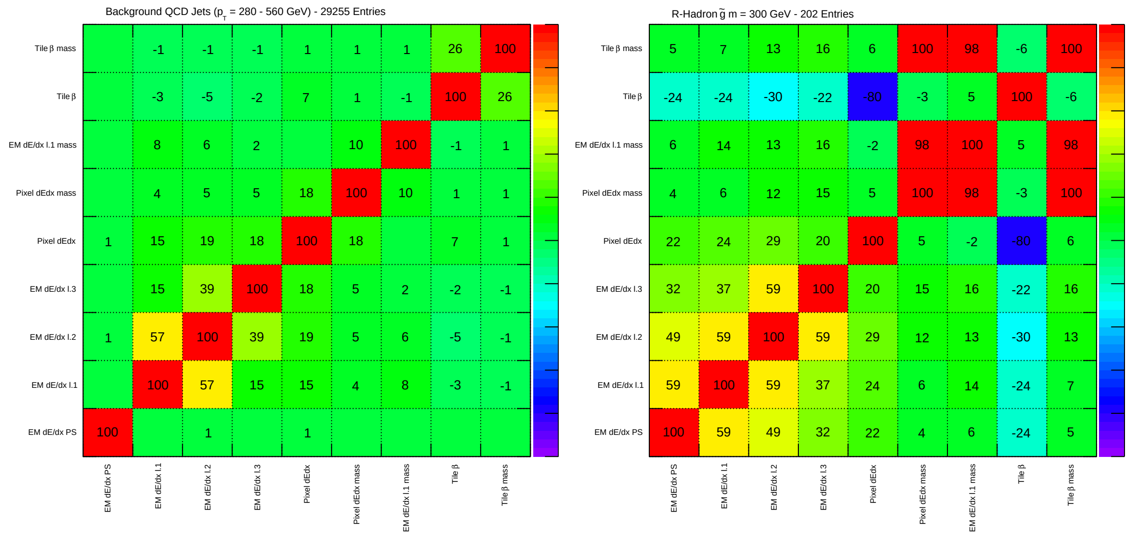

(a) Background QCD Jets ($p_T = 280 - 560$ GeV) (b) R-Hadrons ($m = 300$ GeV)

Figure 9.8: Linear correlations between observables. (Figures in percentage (%).

Mass [GeV]	LAr 3	LAr 2	LAr 1	LAr 0	Tile 1	Tile 2	Tile 3	Pixel	Tile β
100	32.8%	83.5%	69.9%	17.2%	51.3%	50.0%	28.1%	71.4%	97.7%
200	35.5%	83.0%	69.9%	22.5%	51.7%	48.5%	27.3%	70.3%	97.0%
300	37.0%	82.9%	72.9%	26.6%	54.7%	51.1%	28.4%	69.7%	97.5%
400	40.2%	84.2%	75.0%	30.3%	54.9%	51.1%	27.9%	69.4%	97.8%
500	40.3%	83.9%	74.6%	33.0%	54.7%	51.5%	28.3%	68.6%	97.6%
600	41.6%	84.1%	75.6%	34.2%	53.1%	51.4%	30.7%	69.8%	97.3%
700	41.8%	82.9%	75.6%	36.9%	54.1%	51.7%	29.4%	67.0%	97.3%
800	44.7%	84.4%	77.6%	41.8%	52.9%	50.0%	28.7%	66.9%	97.1%
900	46.5%	85.4%	78.6%	42.7%	54.9%	51.7%	29.8%	69.6%	97.1%
1000	45.9%	84.7%	78.6%	46.3%	54.4%	50.5%	28.7%	69.1%	96.8%
$\langle eff \rangle$	40.6%	83.9%	74.8%	33.1%	53.7%	50.7%	28.7%	69.2%	97.3%

Table 9.1: Estimator efficiency. Observable availability per track in signal samples.

The second method (9.7) is the classic signal-to-noise ratio [25],

$$p_{s/\sqrt{b}} = \frac{S}{\sqrt{B}} \tag{9.7}$$

The third method (9.8) is in general the most commonly used [19] approximation of purity,

$$p_{s/\sqrt{s+b}} = \frac{S}{\sqrt{S+B}}. \tag{9.8}$$

Of these three (9.8) is the method selected for the final analysis, based on comparing the tests for all variables (fig. 9.9).

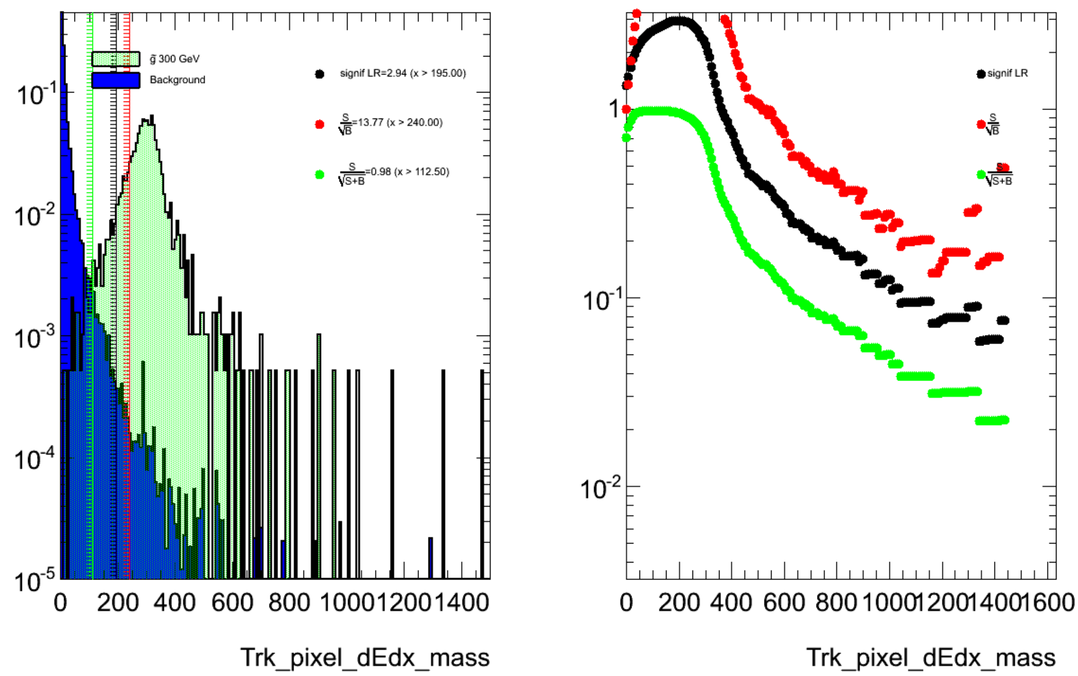

Figure 9.9: Cut optimisation methods

The routine is divided into two parts, part one processes the signal and background monte carlo data filling histograms for each of the observables. The second part calculates the purity for each possible cut_i point in every histogram. The new decision boundary found by the second part is introduced into the analysis process in part one, and the histograms are filled again based on the previous cuts. This approach incorporates correlations among variables by penalising variables that are correlated with variables already chosen earlier in the cut flow.

The procedure can be summarised by:

1. For every observable fill a histogram with signal and a histogram with background.
2. Normalise both histograms to the same area, this results in a shape comparison rather than one based on statistics.
3. For every bin along the x axis calculate $p_i = S/\sqrt{S+B}$ by (9.9), the other purity metrics are calculated in a similar fashion.
4. Find the optimal decision boundary for each observable: $p_{dist} = \max_i p_i$.
5. Compare all observables and find $\max_{dist}\ p_{dist}\varepsilon$ where ε is the estimator efficiency from table 9.1 for the relevant observable.
6. Refill all histograms while applying the previously found cut(s).
7. Repeat the above until $\max_{dist} p_{dist} < c_{termination}$ is met.

In equation 9.9 'dir' is the direction, or the side of the cut value on which the critical region is placed. In figure 9.9 the acceptance region is indicated by the hashed side of the cut line.

$$\frac{S}{\sqrt{S+B}} = \frac{\int_a^b f_N(X|sig)\ \mathrm{d}X}{\int_a^b f_N(X|sig)\ \mathrm{d}X + \int_a^b f_N(X|bg)\ \mathrm{d}X} \quad \begin{cases} a = cut_i, b = \infty & \text{if } dir = -1 \\ a = \infty, b = cut_i & \text{if } dir = 1 \end{cases} \tag{9.9}$$

An illustration of this principle is shown in figure 9.10 for two observables. Because one cut is applied after another (boolean 'AND') the overall parameter space is gradually decreased as exemplified by the shaded regions.

When scanning a distribution with an unknown parameter (the mass), one must be careful not to overtrain or in this case tighten the critical region too much. For the selection each of the 10 mass hypotheses are treated as independent analyses, each with a unique set of cuts based on their specific momentum range and ionisation loss. Because of the nature of this work is to search for a particle with the mass as a free parameter, the above method will introduce a severe bias akin to the look-elsewhere effect [25]. Because of this the final exclusion limit is not directly based on this method, but manual cuts inspired by the output, with careful avoidance of narrow two sided cut windows.

9.4 Event selection

The cut method for the final selection is a combinatorial weighting scheme where if specific observables pass a cut value, a point is assigned to a common sum. If the sum passes a threshold value the track is selected as a R-Hadron candidate. Some of the stronger observables such as Pixel dE/dx can cause subtraction of points if the value is strictly outside the critical region. The calorimeter dE/dx values cannot count by themselves as they only give sensible predictions of the energy deposit is consistent in multiple layers. The argument is that Calorimeter dE/dx is uncorrelated for QCD jets but highly correlated for R-Hadrons. Muons can pass as R-Hadrons in the Calorimeter dE/dx but since they would be MIPs in the Pixel detector or high-β in the Tile, requiring the right amount of points will discriminate against them as well.

The cut-flow is as follows:

- Pass preselection (sec. 9.1).
- $p_T > 50$ GeV.
- Distance to nearest jet $\Delta R_{jet} > 0.5$.
- More than 2 discriminator points from discriminators in table 9.2.
- (tight cut) Mass hypothesis based on either pixel EM Calo dE/dx or Hadronic Calo β between $\pm 2\sigma_m$ of the mass hypothesis.

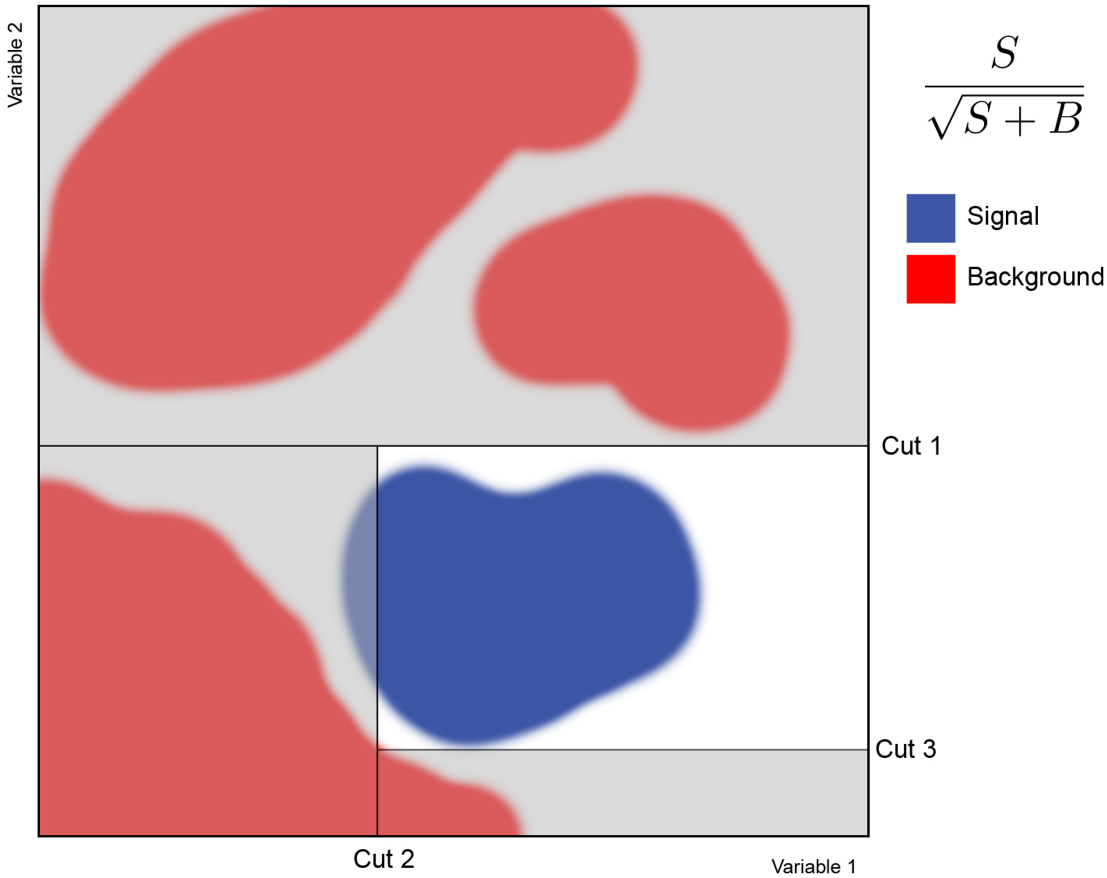

Figure 9.10: Cut optimisation process. With a parameter space spanned by Variable 1 and 2, the optimal cuts are found by calculating the $\frac{S}{\sqrt{S+B}}$ for each variable in 1 dimension. The most significant cut for each variable is evaluated. The largest of the two is chosen as the first cut. The parameter space is reconstructed requiring the cut. The signal significance is calculated and the second cut is place. This cycle continues until the remaining possible cuts becomes insignificant.

9.5 Systematic uncertainties

To place s realistic limit on the production cross section of R-Hadrons it is necessary to consider sources of systematical uncertainties. The estimated uncertainties used in this analysis is taken from our collaborative effort [8]. The systematic uncertainty on the signal is estimated to be 20% and the background uncertainty is estimated to be 30%. The background estimate is not strictly compatible with this analysis, as a data-driven approach is used in our note, while monte-carlo samples is used in this analysis. From comparison between the two methods and data in a side-band region, it is estimated that monte-carlo provides a less accurate estimate of the background than the data-driven method. Nevertheless it is beyond the scope of this work to implement the other method and the uncertainty is taken as an optimistic estimate of the overall uncertainty.

Estimator	Cut	λ
Pixel dE/dx	> 1.8	$+1$
Pixel dE/dx	< 1.8	-1
Tile β	< 0.9	$+1$
N Tile Calo dE/dx with $0.0 < dE/dx < 10.0$	> 1	$+1$
N LAr Calo dE/dx with $0.0 < dE/dx < 10.0$	> 1	$+1$
if LAr $N > 2$ AND Tile $N > 1$	—	$+1$

Table 9.2: Combinatorial discriminator. The maximum number of points possible is 5 with both LAr and Tile available.

Cutflow ($\int \mathcal{L}dt = 15.30$ pb)												
Cut	Data ($\sqrt{s} = 7$ TeV)	Background	$\tilde{g}$ 100 GeV	$\tilde{g}$ 200 GeV	$\tilde{g}$ 300 GeV	$\tilde{g}$ 400 GeV	$\tilde{g}$ 500 GeV	$\tilde{g}$ 600 GeV	$\tilde{g}$ 700 GeV	$\tilde{g}$ 800 GeV	$\tilde{g}$ 900 GeV	$\tilde{g}$ 1000 GeV
Observed/Expected	219676	175678.0	322819.5(99.5%)	9562.5(100.0%)	945.6(99.5%)	159.1(100.0%)	35.8(100.0%)	8.8(90.5%)	3.0(100.0%)	1.0(99.8%)	0.4(100.0%)	0.1(99.8%)
Passed GRL (data)	158222	175678.0	322819.5(99.5%)	9562.5(100.0%)	945.6(99.5%)	159.1(100.0%)	35.8(100.0%)	8.8(90.5%)	3.0(100.0%)	1.0(99.8%)	0.4(100.0%)	0.1(99.8%)
Passed Overlap (data)	157682	175678.0	322819.5(99.5%)	9562.5(100.0%)	945.6(99.5%)	159.1(100.0%)	35.8(100.0%)	8.8(90.5%)	3.0(100.0%)	1.0(99.8%)	0.4(100.0%)	0.1(99.8%)
Passed Trigger	71084	63926.9	49818.6(15.4%)	2375.2(24.8%)	302.1(31.8%)	56.4(35.4%)	13.8(38.5%)	3.6(37.5%)	1.3(43.9%)	0.4(44.8%)	0.2(45.6%)	0.1(47.3%)
Passed Preselection	69220	63922.5	49510.5(15.3%)	2367.9(24.8%)	301.2(31.7%)	56.2(35.3%)	13.7(38.4%)	3.6(37.4%)	1.3(43.9%)	0.4(44.7%)	0.2(45.5%)	0.1(47.2%)
$p_T > 50GeV$	48520	34464.8	38942.9(12.0%)	1931.9(20.2%)	254.0(26.7%)	47.8(30.0%)	11.8(33.0%)	3.1(32.4%)	1.1(38.0%)	0.4(38.7%)	0.1(39.1%)	0.1(41.1%)
$\Delta R_{jet} > 0.5$	39327	21871.4	36231.7(11.2%)	1810.2(18.9%)	236.7(24.9%)	44.2(27.8%)	10.9(30.3%)	2.9(29.7%)	1.0(34.8%)	0.4(35.2%)	0.1(35.4%)	0.0(37.5%)
$disc > 1$	206	291.1	15034.9(4.6%)	957.3(10.0%)	145.8(15.3%)	29.5(18.5%)	7.6(21.3%)	2.0(21.0%)	0.7(24.7%)	0.3(25.6%)	0.1(26.2%)	0.0(28.4%)
Mass σ_m	69	57.1	13956.6(4.3%)	911.0(9.5%)	138.9(14.6%)	28.2(17.8%)	7.3(20.3%)	1.9(19.8%)	0.7(23.4%)	0.2(23.5%)	0.1(24.0%)	0.0(25.4%)

Table 9.3: Cutflow. The last (mass) cut listed for the background estimate and data is assuming the $2\sigma_{mass}$ window around the 100 GeV R-Hadron hypothesis. A similar estimate for each mass hypothesis have been calculated and used in the counting process for the final limit.

9.6 Limit

Considering the counting results from the previous section, no signal is expected in the observation. Instead an upper limit on the R-Hadron production cross section by gluino-gluino pairs is estimated.

The methodology behind the limit setting is explained in appendix A.2, but the specific method applied is as follows.

The limit is calculated by counting the number of events that passes the selection in section 9.4. For data the number is obviously an integer value, we either observe an event or not. For the expected background the number of events is scaled to fit the integrated luminosity of the observed data. If the observed number of data and background events matches we naively conclude that the signal absent. This method is flawed for many reasons, firstly we need to account for fluctuations in the background expectation, and the systematical uncertainties have not been folded into the assumption.

To handle the possibility of background fluctuations we assume that the events are poissonian distributed so if we expect to observe n_b background events the probability of observing n_0 or more due to fluctuations is given by

$$\alpha = \sum_{i=n_0}^{\infty} \frac{n_b^i e^{-n_b}}{i!}, \tag{9.10}$$

where α is the statistical significance. If $\alpha \to 0$ it would imply a significant deviation from the background expectation. In particle physics this deviation is typically measured in terms of the quantile of the normal distribution (A.7) and the misused tradition has it that 5σ deviations is a discovery of something new, while 3σ is said to be evidence of something.

Returning to limits, the connection between the number of observations is related to the process cross section by

$$\sigma = \frac{N}{\varepsilon \mathcal{L}} \tag{9.11}$$

Where N is the number of observations (or in this case the upper limit on the number of counts), ε is the selection efficiency ($\varepsilon = \frac{n_{\text{observed}}}{n_{\text{produced}}}$) and $\mathcal{L}$ is the integrated luminosity in which the N observations have been made.

The limit is calculated by inverting the range in (9.10) and ask, how many signal events (s) could be contained within the combined signal and background expectation (b) given the observation of n events, with the significance less than some value. This exact formulation calls for the maximisation of s in (9.12) with a fixed value of α,

$$CL_{s+b} = 1 - \alpha = \sum_{i=0}^{n} e^{-(s+b)} \frac{(s+b)^i}{i!} \tag{9.12}$$

The confidence level CL is traditionally fixed at either 95% or 90%, meaning that we calculate the largest possible value of s possible while assuming that the probability of it being due to a signal under fluctuation is less than $\alpha = 5\%$. [16].

Relying on (9.12) can be dangerous if we expect down-fluctuations in background expectations, as it will inadvertently affect the signal expectations. Instead the method used seek to neutralise the problem of background fluctuations by introducing a likelihood ratio between the signal plus background hypothesis and a background only hypothesis. This method is called the CL_s method (9.13) [40],

$$CL_s = \frac{CL_{s+b}}{CL_b} = 1 - \alpha = \frac{\sum_{i=0}^{n} \frac{(s+b)^i}{i!} e^{-(s+b)}}{\sum_{i=0}^{n} \frac{b^i}{i!} e^{-b}}. \tag{9.13}$$

Including systematical uncertainties is done by smearing b and s by a gaussian with the mean at the expected background and signal values and the width defined by the uncertainties [3]. The signal is then maximised with some specific result from the smearing. This is repeated a large number of times for difference samplings from the smearing distribution. The final upper limit is then the mean of the result from each smearing-maximisation cycle. Combining (9.10) with this smearing method, we end up with

$$CL_s = 1 - \alpha = \frac{\sum_{i=0}^{n} \frac{(\mathcal{L}\sigma_{\tilde{g}} sig_{eff_{smeared}} + b_{smeared})^i}{i!} e^{-(\mathcal{L}\sigma_{\tilde{g}} sig_{eff_{smeared}} + b_{smeared})}}{\sum_{i=0}^{n} \frac{b^i_{smeared}}{i!} e^{-b_{smeared}}}. \tag{9.14}$$

Which we maximise for $\sigma_{\tilde{g}}$ with the requirement that $\alpha = 0.05$. The final result is plotted along with the predicted gluino production cross section, calculated with PROSPINO in figure 9.11.

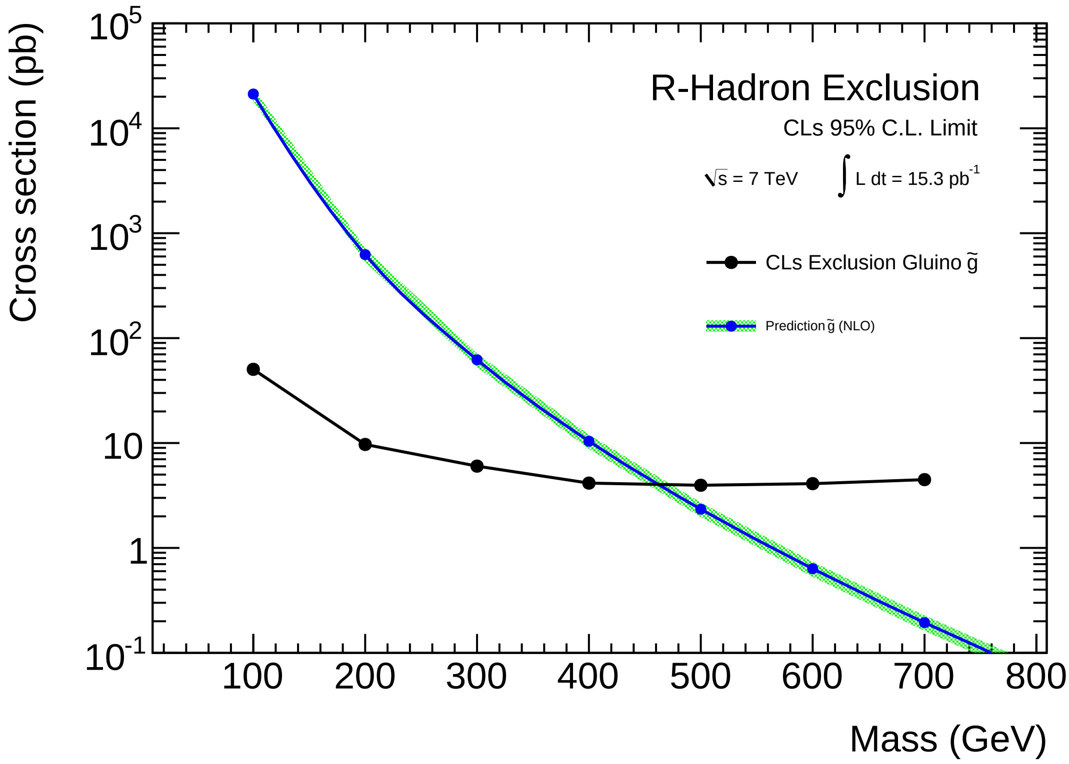

Figure 9.11: The final limit based on the method described in section 9.4.

10

Conclusion

In this thesis I have developed a method for extracting dE/dx estimates from the ATLAS calorimeters. I have shown that the dE/dx measurements of R-Hadrons from the calorimeters are similar to those of slow moving Standard Model particles in less dense detectors, clearly discriminating them from Standard Model particles, as they would either be stopped or minimum ionising in the same environment. This method have potential applications in further searches for penetrating charged particles at other experiments. I have developed a mass estimation method based on dE/dx measurements. The mass estimation calibration can in principle be used to calibrate to other functions than the one used in this analysis, as it simply provides a robust 2D fitting method. I have applied the mass estimation method to collision data, showing recognisable mass peaks for low momentum kaons, protons and deuterons. The calorimeter dE/dx estimators and the mass estimates have been used in a search for stable gluinos, hadronising into R-Hadrons. The search have placed an upper limit on gluino production at $\sqrt{s} = 7$ TeV with 15.3 pb^{-1} data. In comparison with the Split-SUSY scenario the limit corresponds to an exclusion of stable gluinos with masses less than 450 GeV.

Perspectives

In parallel to the writing of my personal analysis, I have taken part in the official ATLAS search for heavy long lived hadronising particles. In this forum I have contributed with a pixel based mass estimator (chapter 8) currently serving as one of the two main estimators in the analysis. I have been responsible for calculating the theoretical expectations with the PROSPINO application (chapter 3.3). Lastly I have performed the final limit setting with the methods described in chapter 9.6.

With the 34 pb^{-1} data accumulated during 2010, we are preparing an article for publication moving the upper limit on stable gluino, stop and sbottom production below 1 pb for masses in excess of 200 GeV. The preliminary limits from this analysis is presented in figure 10.1.

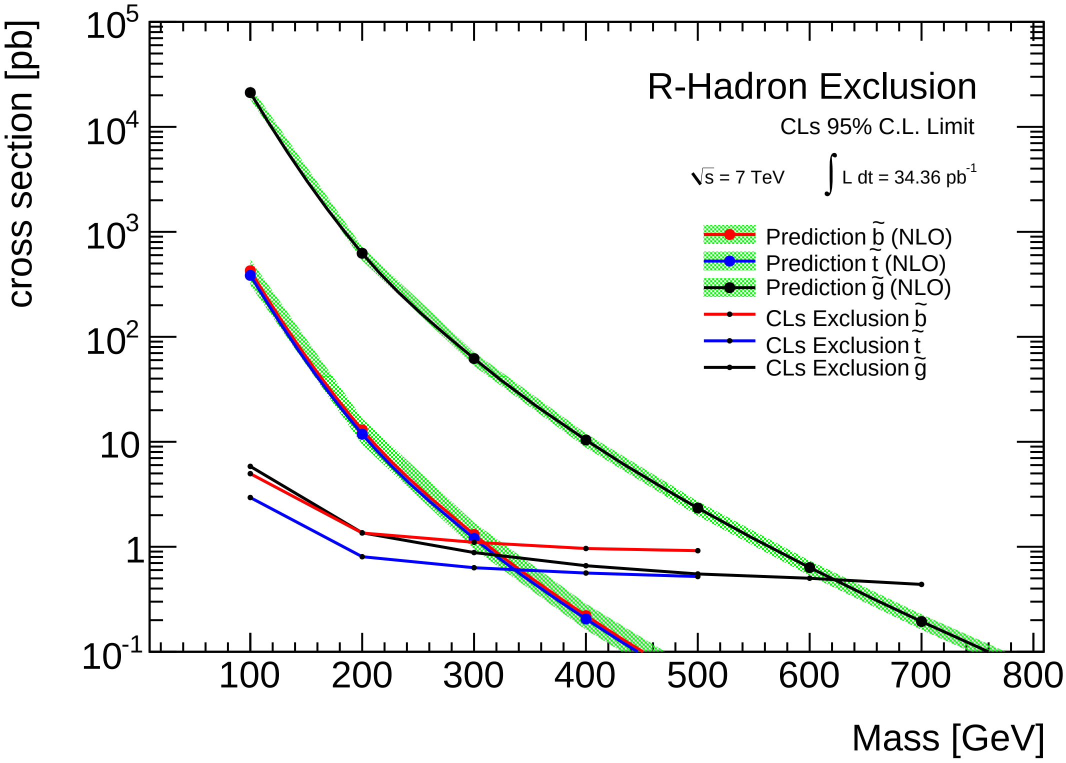

Figure 10.1: Preliminary limits for the official ATLAS analysis (Work in progress).

Part V

Appendices

A

Statistical methods

Due to the methodology of particle physics, each measurement, or event is in itself an experiment, with a probabilistic outcome. Given a theory, the goal is to either discover or exclude it's existence, based on statistical evidence arising from variations in distributions of observables.

This chapter describes the statistical techniques used in our analysis, in relation to preparing observables, selection and defining exclusion limits.

A.1 Basic definitions

The number of observed events N given a specific process with the cross-section σ and the integrated luminosity $\mathcal{L}$ is defined as:

$$N = \varepsilon \mathcal{L} \sigma, \tag{A.1}$$

where ε is the selection efficiency,

$$\varepsilon = \frac{\text{signal events surviving selection cuts}}{\text{signal events created}} \tag{A.2}$$

Hypothesis testing

The baseline for all scientific studies is the "scientific method", with which we compare a theory with observation in order to falsify [39] the hypothesis. If the comparison stand, the theory is said to be a valid description of the observed phenomenon. Statistically [13, p. 48], we can represent a theory as a multi-dimensional probability density function (p.d.f.), if a sample of observations falls within the theoretically predicted p.d.f. the theory is said to describe the observations.

In particle physics it is customary to compare observations with the standing theory; "The Standard Model" as well as a competing model representing new physics. Let us denote the standard model as H_0 and refer to it as the "null hypothesis" and the alternative model H_1 as the "signal hypothesis", both described by some multi-dimensional p.d.f. $f(\mathbf{x})$ of random variables $\mathbf{x}$.

In order to test which of these hypothesises best describes the observed phenomenon specified by n measured values[1] $\mathbf{x} = x_1, ..., x_n$, we can construct a simplified representation

[1] these could correspond to a single measurement of n dimensions, or simply n repeated measurements of the same variable, or some combination

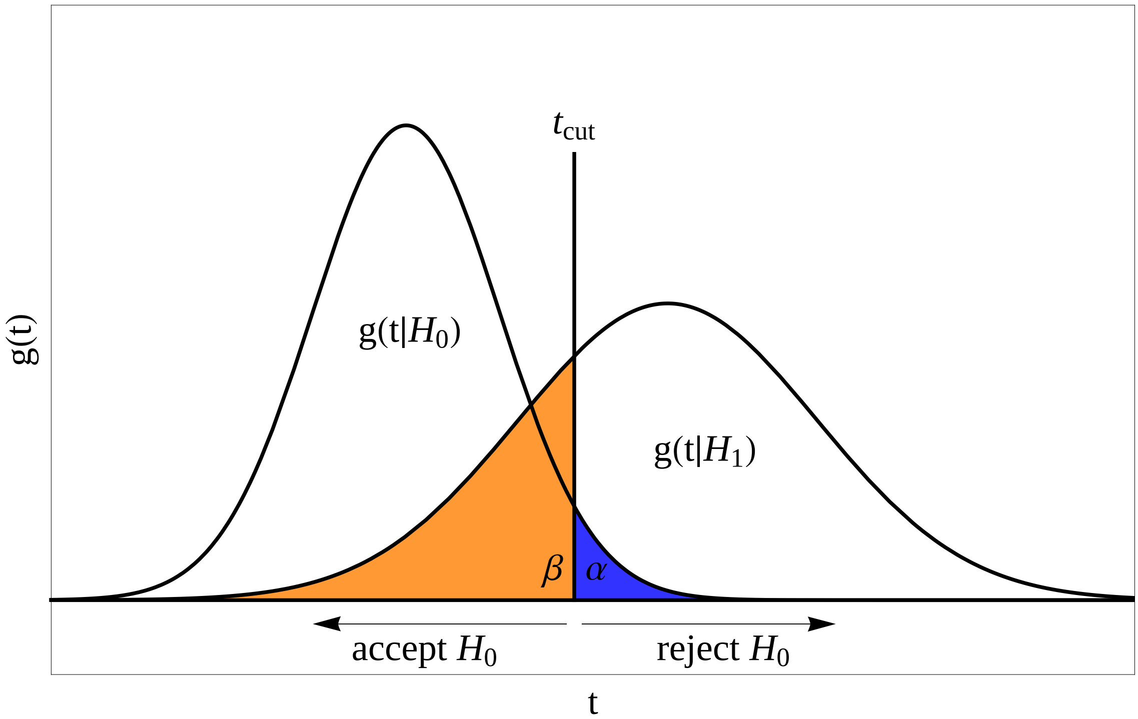

Figure A.1: **Hypothesis test**, α region: probability of observing the null hypothesis in the alternative hypothesis region (known as the significance and the type I error), β region: probability of observing the signal in the null hypothesis region (type II error).

of the measured variables called a test statistic $t(\mathbf{x})$. Each of the hypothesises is then represented by a function of t: $g(t|H_0)$ and $g(t|H_1)$.

We could use all the measured variables as a test statistic rather than a subset, the idea is lowering the dimensionally of the problem without loss of discrimination power.

If the test statistic is simply defined by a scalar function $t(\mathbf{x})$ with the p.d.f. $g(t|H_0)$ if the null hypothesis is true or $g(t|H_1)$ of the alternative hypothesis is true, we have a situation as illustrated in fig. A.1.

In order to select between the two hypothesises we must be able to discriminate whether the observed data best describes the null hypothesis or the alternative. This is done by specifying a critical region, or "cut" t_{cut} where if the measurements fall within the region H_0 is rejected otherwise it is accepted. The compliment to the critical region is called the "acceptance region" for the null hypothesis.

The probability of observing H_0 in the critical region is,

$$\alpha = \int_{t_{cut}}^{\infty} g(t|H_0)\ \mathrm{d}t \tag{A.3}$$

called the significance of the test, and is known as the error of the first kind since it is the probability of rejecting the H_0 hypothesis if its true.

While the probability of observing the alternative hypothesis in the acceptance region is,

$$\beta = \int_{-\infty}^{t_{cut}} g(t|H_1)\ \mathrm{d}t \tag{A.4}$$

where $1-\beta$ is known as the error of the second kind as it is the probability of rejecting the H_1 hypothesis if its true it is also the power to discriminate against the alternative hypothesis H_1 of the test.

A.2 Counting experiments

The typical way of conducting a measurement in particle physics is by counting the number of events collected in some region defined by a series of selection cuts. If the number of events exceed the number of expected counts from known physics (i.e. background) by some significant value a discovery can be claimed. If on the other hand, the observed count is comparable to the expected background count (including statistical fluctuations and systematical errors) one can place an upper limit on the expected but unobserved signal process, i.e. lowering its observed cross-section. If the observed upper limit on a given process falls below the theoretically predicted value, one can exclude the theory.

If the number of expected events in the acceptance region is large, the count follow a Gaussian distribution. In the case of a small number of expected events, we should instead expect a Poissonian distribution. As the subject of this thesis is a search for rare events, we assume a Poissonian description.

Poisson statistics

If the number of expected counts is low, the probability of observing n counts given an expected number of counts ν is described by a Poisson distribution

$$P(n|\nu) = \frac{\nu^n}{n!}e^{-\nu}. \tag{A.5}$$

If n_b background counts is expected, then due to possible fluctuations the probability of observing n_0 or more events with the statistical significance α is given by:

$$\alpha = \sum_{i=n_0}^{\infty} \frac{n_b^i e^{-n_b}}{i!} \tag{A.6}$$

The statistical significance can be described as the probability of observing the number of events n_0 by background fluctuations alone. The smaller an α value the more certain one can be that a statistically significant signal is observed.

Usually α is quoted in $n\sigma$ or the quantile of the normal distribution,

$$\alpha = \int_{n\sigma}^{\infty} \frac{1}{\sqrt{2\pi}} e^{-x^2/2}\,\mathrm{d}x = 1 - \frac{1}{2}\mathrm{erf}\left(\frac{n}{\sqrt{2}}\right) \tag{A.7}$$

Where a value of 5σ corresponds to a “discovery” and 3σ is “evidence of”.

In searches for new physics, the likelihood of discovering a signal is on the whole rather remote. If no significant deviation from the expected background can be found, an exclusion limit on the hypothetical signal can be placed instead.

Exclusion limits

Assume we want to investigate a signal process on top of a background process. After applying event selection maximising the significance ($S = \frac{n_{obs}-n_b}{\sqrt{n_b}} = \frac{n_s}{\sqrt{n_b}}$, see chapter 9.3) we are left with two cases, signal and signal+background. In order to compare the two scenarios with data, we scale them the to observed luminosity and count the number of signal events n_s and background events n_b, along with the expected number of counts s and b.

These counts should be poisson distributed, so we have the count probability given by:

$$p(n_s|s) = \frac{s^{n_s}e^{-s}}{n_s!}, \quad p(n_b|b) = \frac{b^{n_b}e^{-b}}{n_b!} \tag{A.8}$$

If we are unable to discriminate between signal and background counts we observe $n = n_s + n_b$ where the p.d.f. is given simply by the sum:

$$p(n_s + n_b|s, b) = \frac{s^{n_s}e^{-s}}{n_s!} + \frac{b^{n_b}e^{-b}}{n_b!} \tag{A.9}$$

$$p(n|s, b) = \frac{(b+s)^n e^{-(s+b)}}{n!} \tag{A.10}$$

A.3 Combining correlated estimates

If a measurement of some quantity, the length of a table, the temperature of a fluid etc. can be done in more than one way, one have the problem of estimating the best value by the set of estimates available. If for instance we had three rulers of different brands and measured the long side of a table with these, could we just take the geometric average $\left(\hat{y} = \frac{y_1+y_2+y_3}{3}\right)$ and assume that would be the best value? If the three rulers had zero in common (i.e. uncorrelated) and they used the same length-scale (unbiased) the average would not be too bad an idea, but what if two of the rulers where made of the same material, and the last one was made with the same machine as one of the first? Correlations introduced between measurements can lead to less powerful estimates if not handled correctly.

Weighted mean

For uncorrelated measurements the normal way of combining different estimates are by weighting each of them by their variance:

The mean value is thus given by:

$$\hat{y} = \sum \left(y_i/\sigma_i^2\right) / \sum \left(1/\sigma_i^2\right) \tag{A.11}$$

And its variance by:

$$1/\sigma^2 = \sum \left(1/\sigma_i^2\right) \tag{A.12}$$

This method accounts for the variations in measurement resolution, but assumes that one measurement is strictly unaffected by the methodology of all the rest.

Correlated mean

For correlated measurements we should account for the covariance between each estimator, this is done by using the Error Matrix (also known as the Covariance Matrix) where the off-diagonal elements correspond to the covariance between any two variables and the diagonals are the single value variances.

$$\mathbf{E} = \begin{bmatrix} \mathrm{var}(X_1) & \mathrm{cov}(X_1, X_2) & \cdots & \mathrm{cov}(X_1, X_n) \\ \mathrm{cov}(X_2, X_1) & \mathrm{var}(X_2) & \cdots & \mathrm{cov}(X_2, X_n) \\ \vdots & \vdots & \ddots & \vdots \\ \mathrm{cov}(X_n, X_1) & \mathrm{cov}(X_n, X_2) & \cdots & \mathrm{var}(X_n) \end{bmatrix} \quad \text{(A.13)}$$

By using the relationships between the different estimators described by the Error Matrix, it is possible to calculate a set of coefficients α_i that describe how much each estimator should contribute to the best estimate in order to minimise variance based on correlations.

The best estimate can then be expressed as a simple linear sum:

$$\hat{y} = \sum \alpha_i \; y_i \quad \text{(A.14)}$$

where we require the coefficients to be normalised,

$$\sum \alpha_i = 1. \quad \text{(A.15)}$$

Using matrix notation the best estimate variance is given by:

$$\sigma^2 = \alpha^T \; \mathbf{E} \; \alpha \quad \text{(A.16)}$$

Calculating the coefficients can be done in many ways (Ref. [31]) but using Lagrange Multipliers we get to a fairly simple expression:

$$\alpha = \mathbf{E^{-1}}\mathrm{U}/(\mathrm{U^T} \; \mathbf{E^{-1}} \; \mathrm{U}) \quad \text{(A.17)}$$

Here $\mathbf{E^{-1}}$ is the inverse of the Error Matrix, and U is a vector with n unitary components, where n is the number of estimators used.

B

Distributions

This chapter contains distributions for each signal sample, and background type as well as data.

B.1 Signal Samples

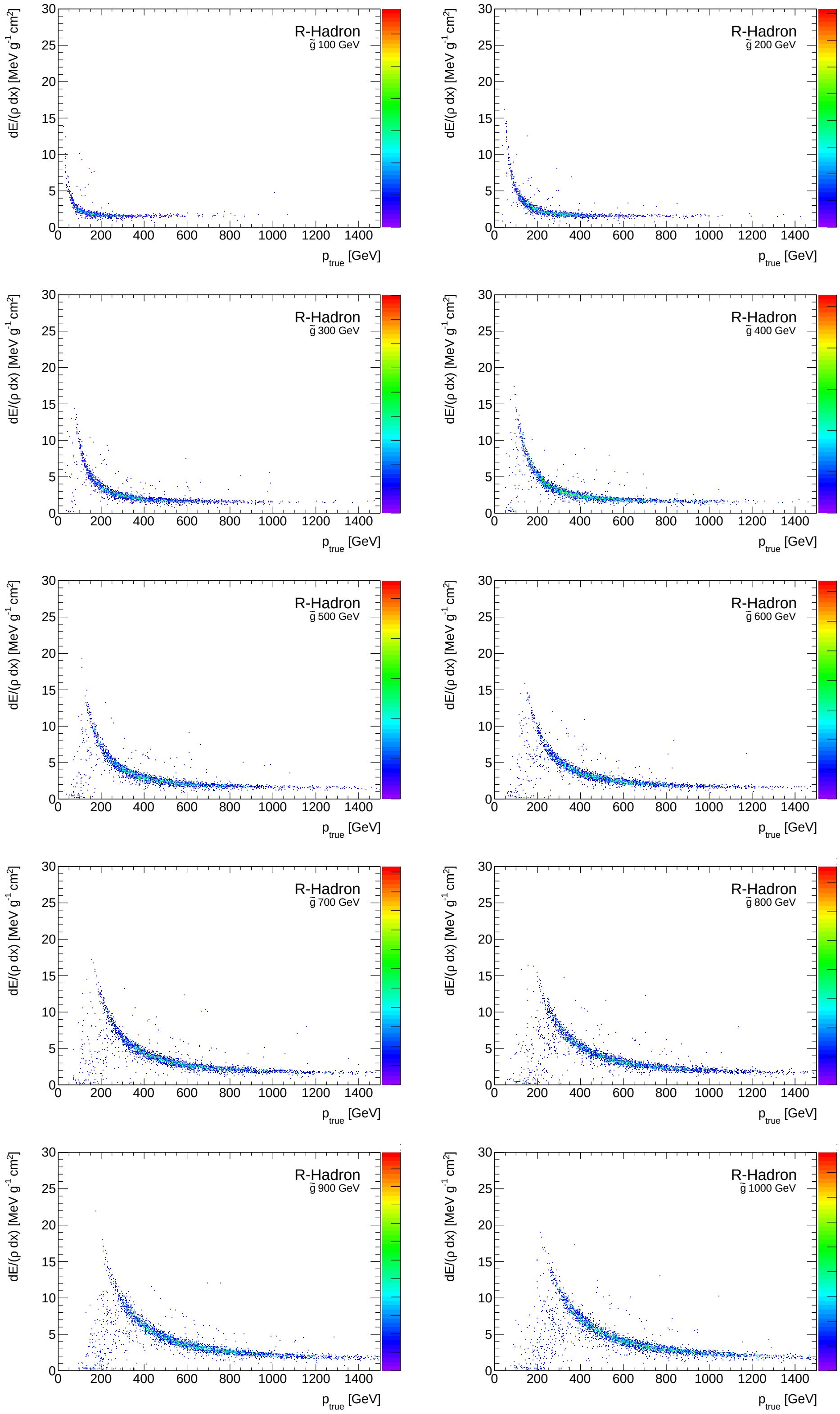

Figure B.1: Pixel, dE/dx for signal samples.

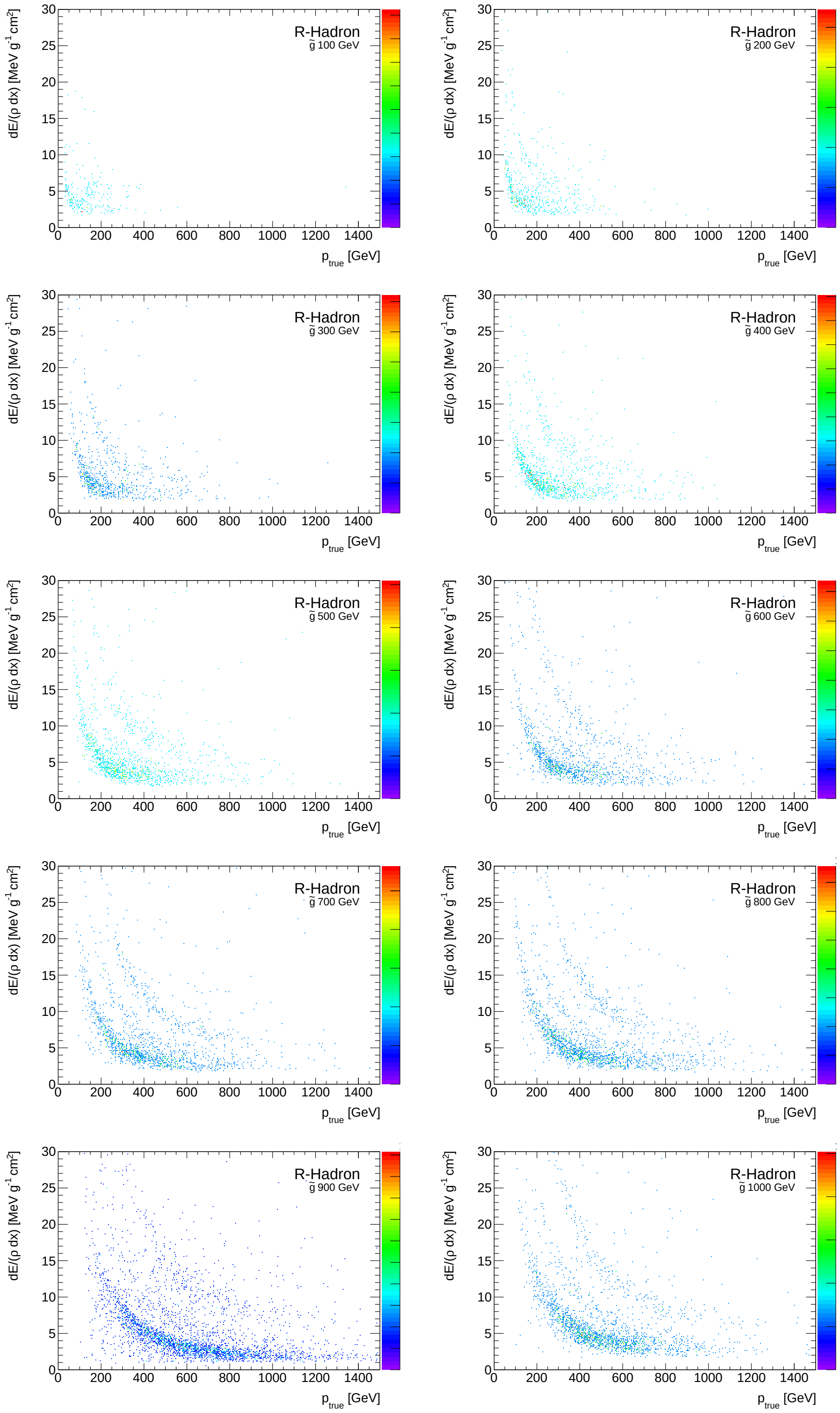

Figure B.2: Electromagnetic calorimeter barrel, Presampler, dE/dx for signal samples.

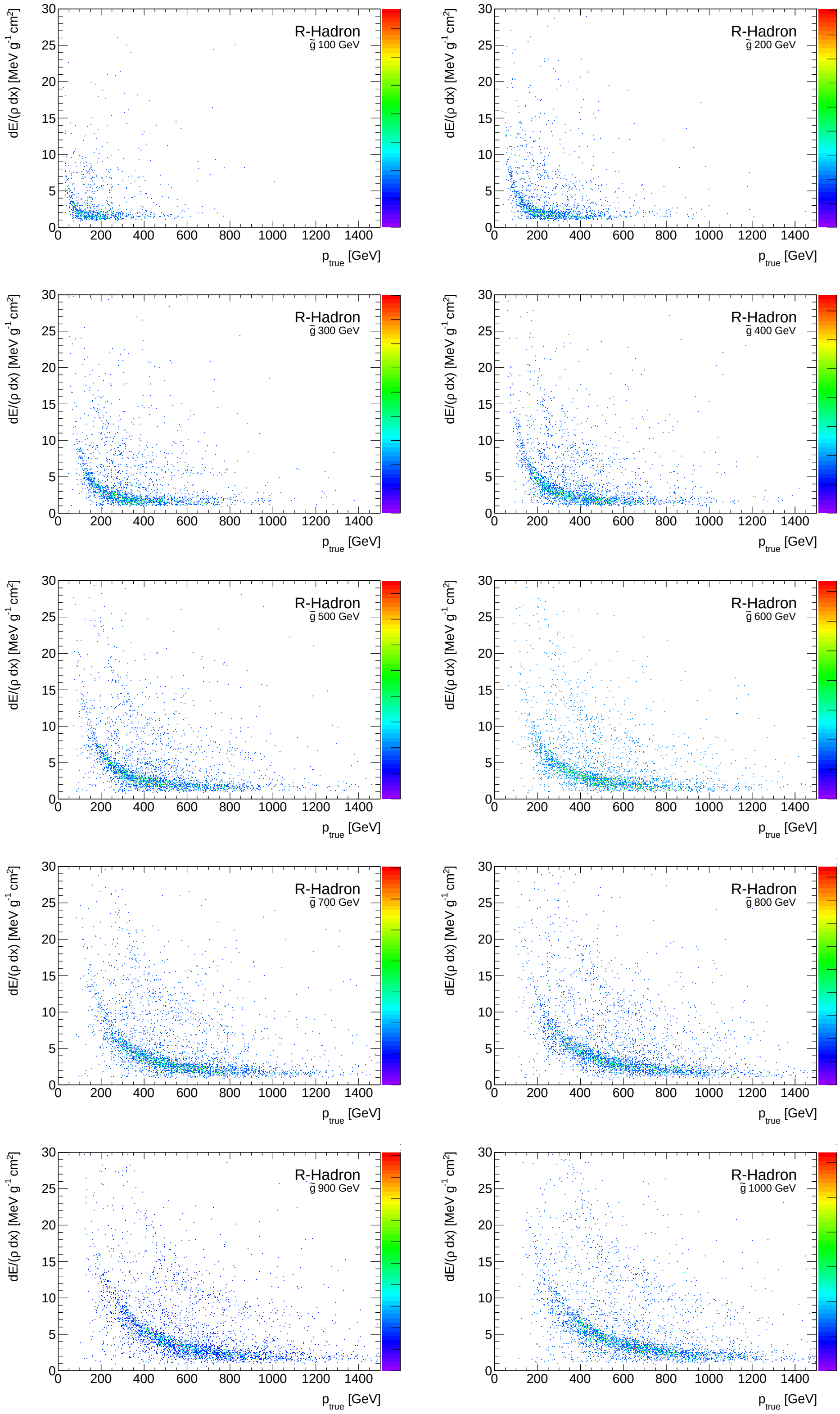

Figure B.3: Electromagnetic calorimeter barrel, layer 1, dE/dx for signal samples.

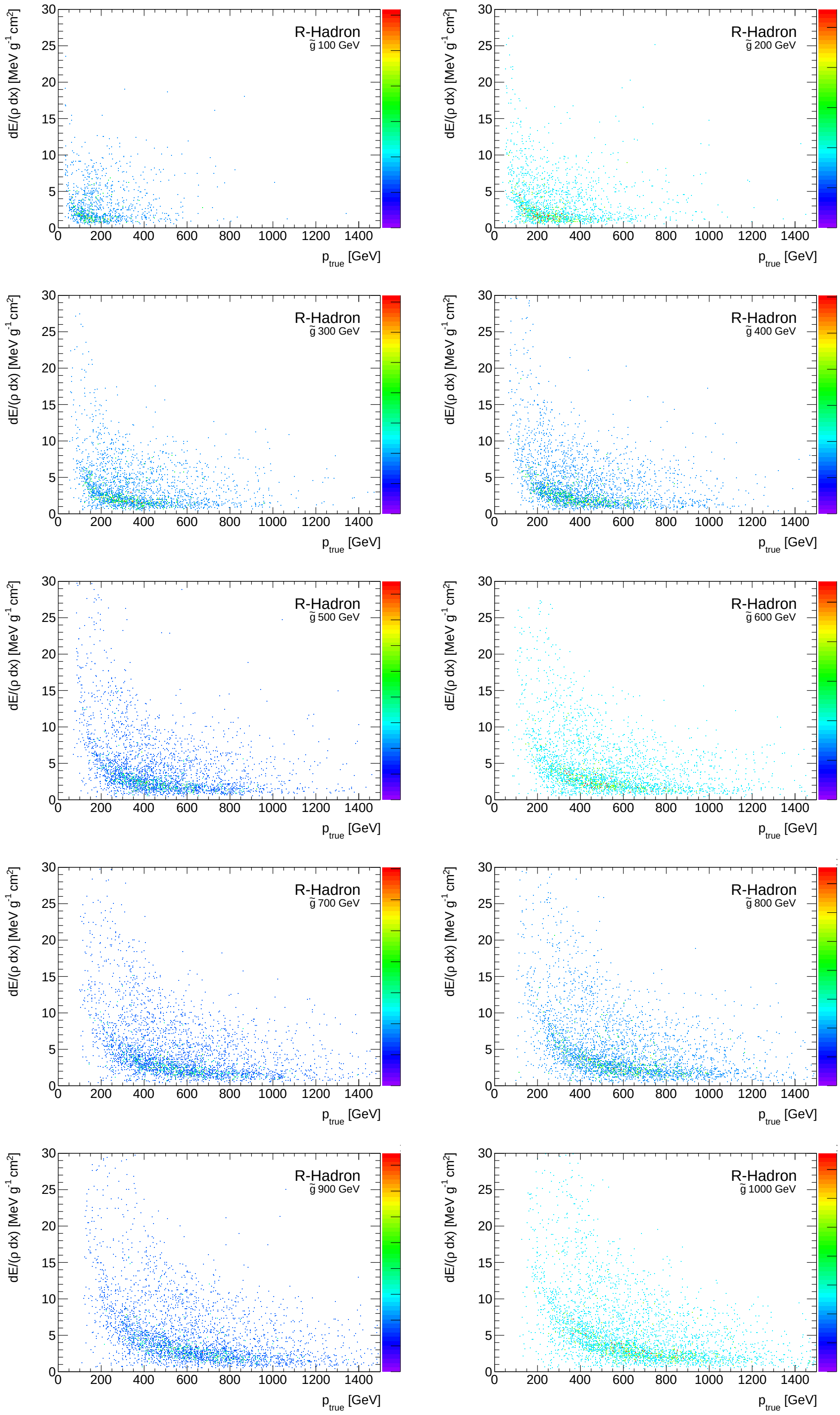

Figure B.4: Electromagnetic calorimeter barrel, layer 2, dE/dx for signal samples.

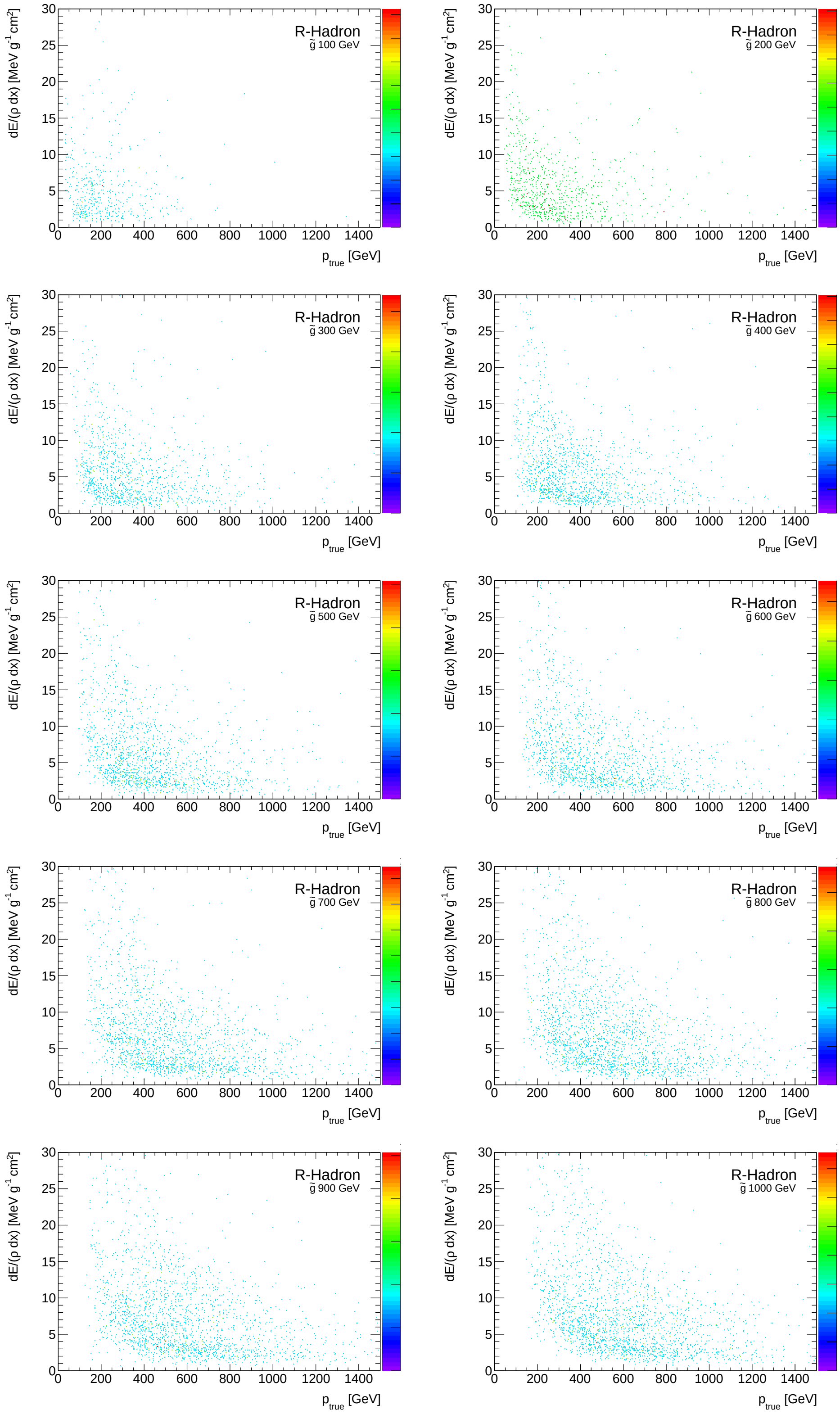

Figure B.5: Electromagnetic caloPlots barrel $|\eta| < 3.x$ layer 3, dE/dx for signal samples.

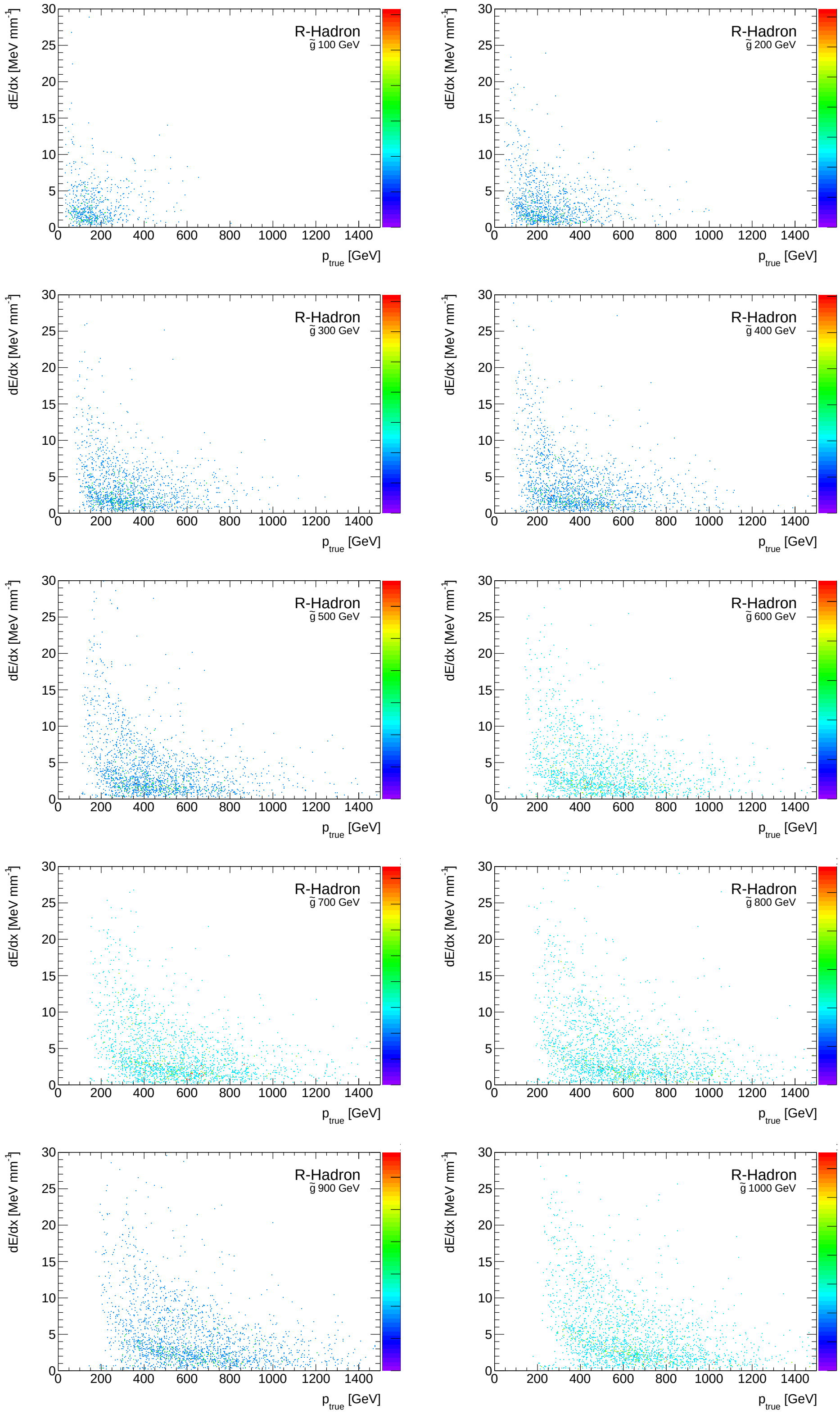

Figure B.6: Tile layer 1, dE/dx for signal samples.

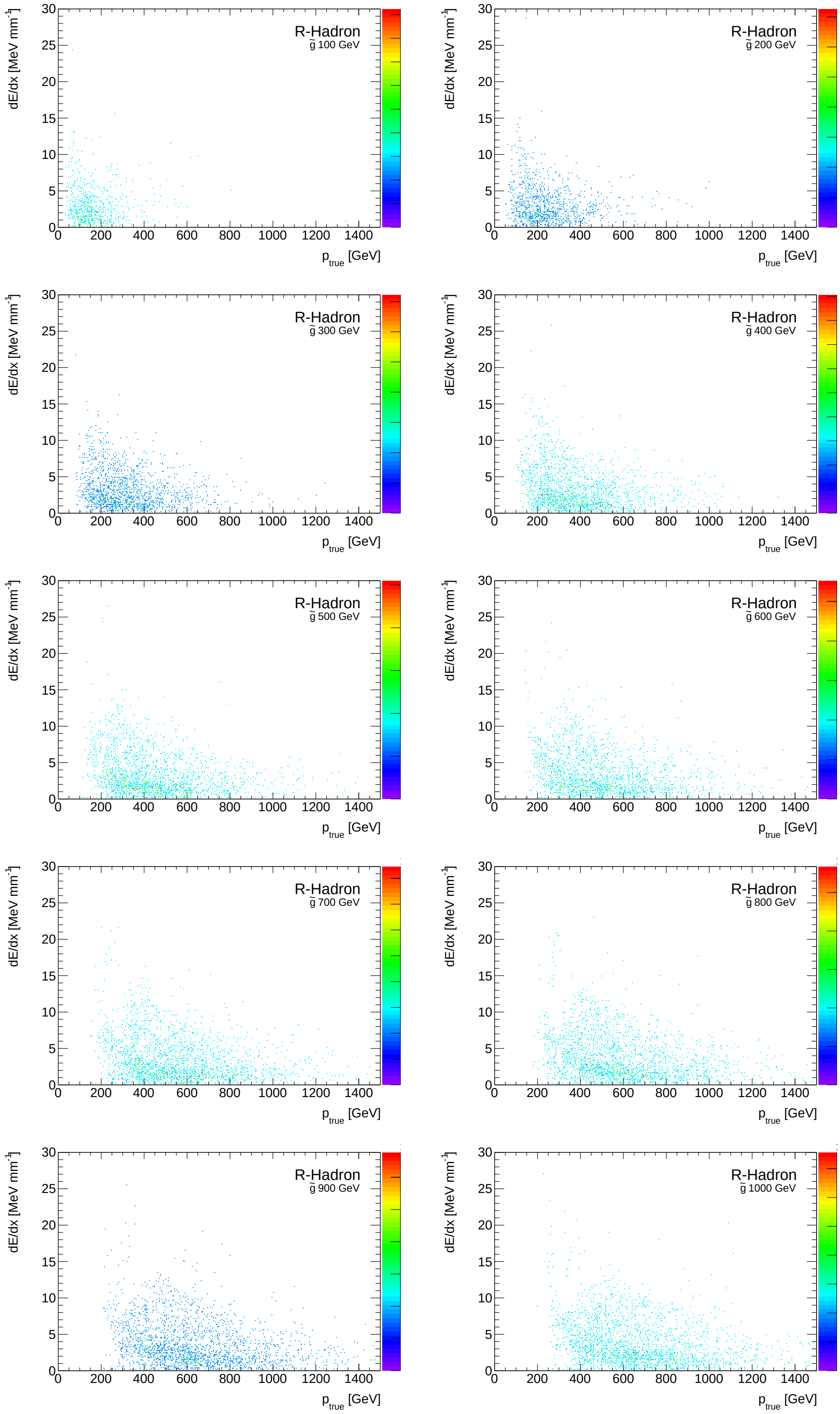

Figure B.7: Tile layer 2, dE/dx for signal samples.

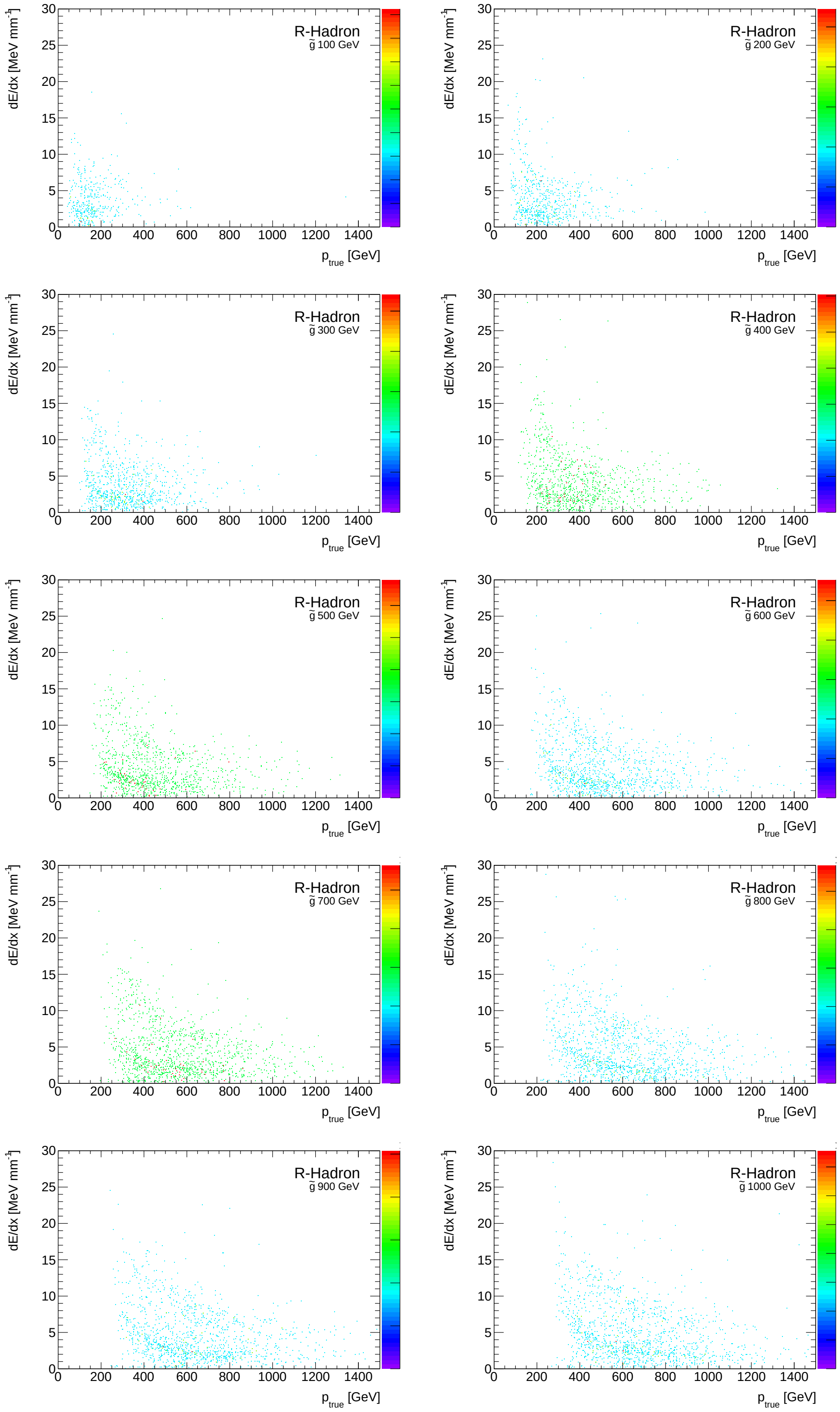

Figure B.8: Tile layer 3, dE/dx for signal samples.

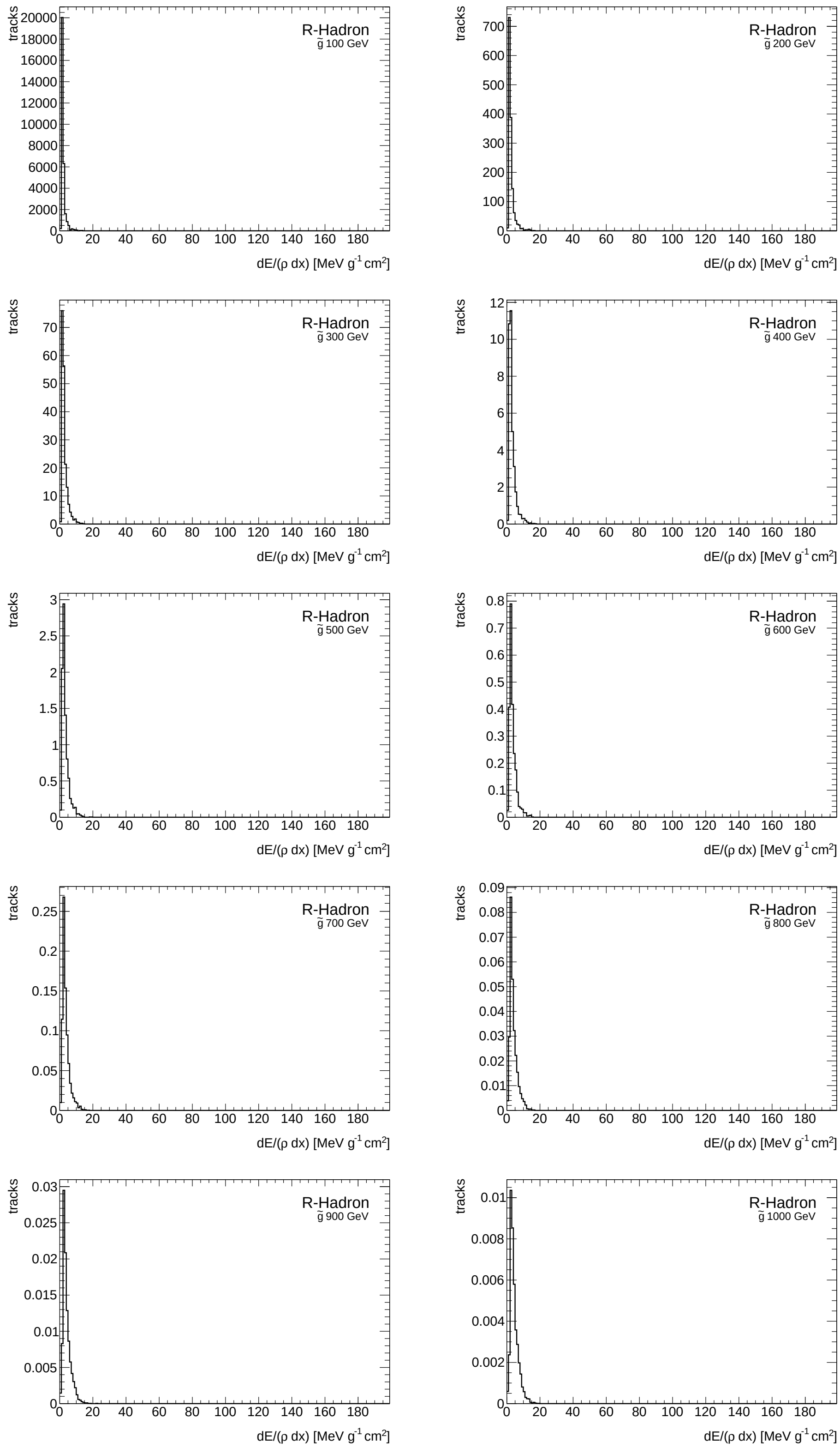

Figure B.9: Pixel, dE/dx for signal samples.

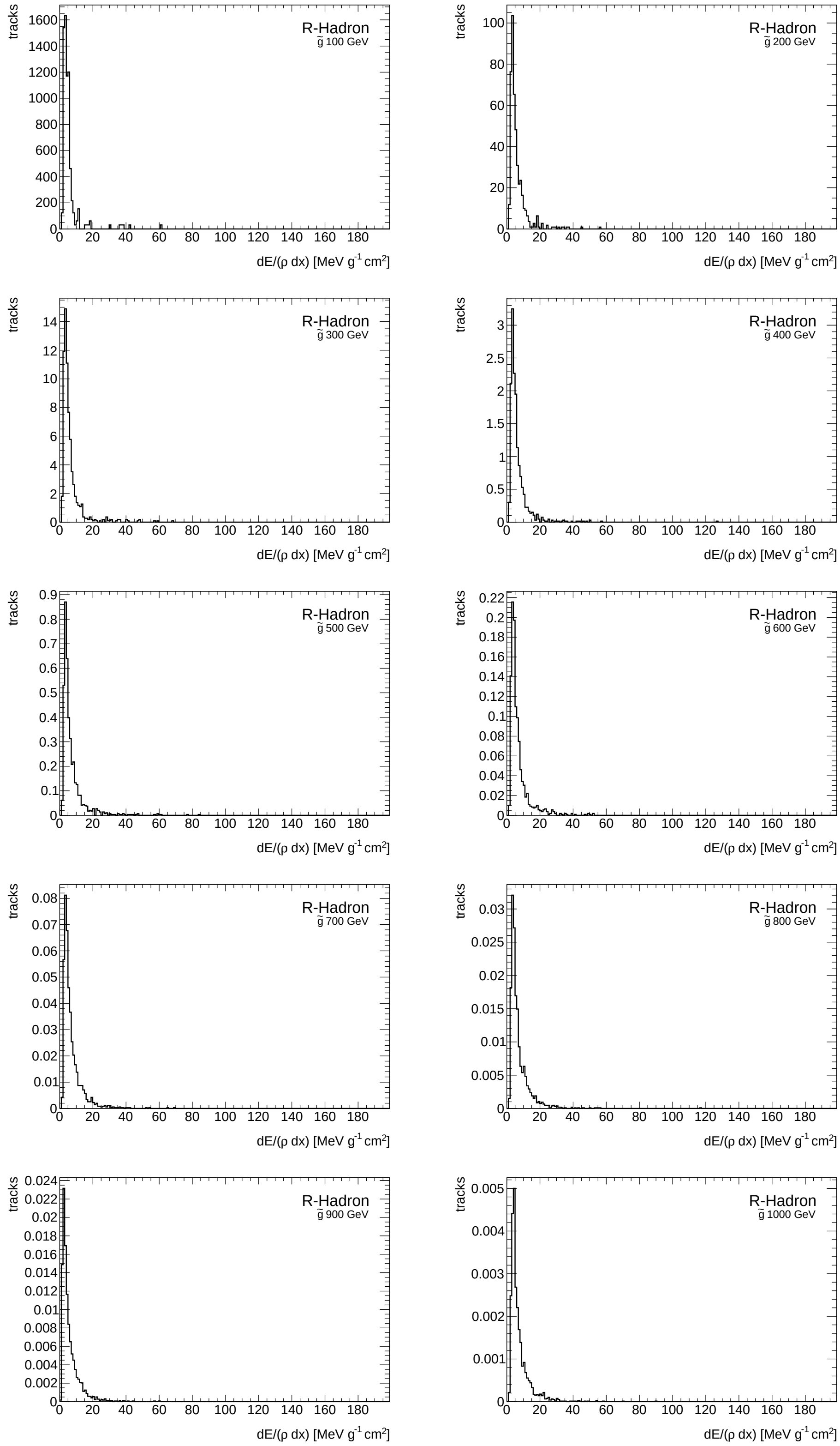

Figure B.10: Electromagnetic calorimeter barrel, Presampler, dE/dx for signal samples.

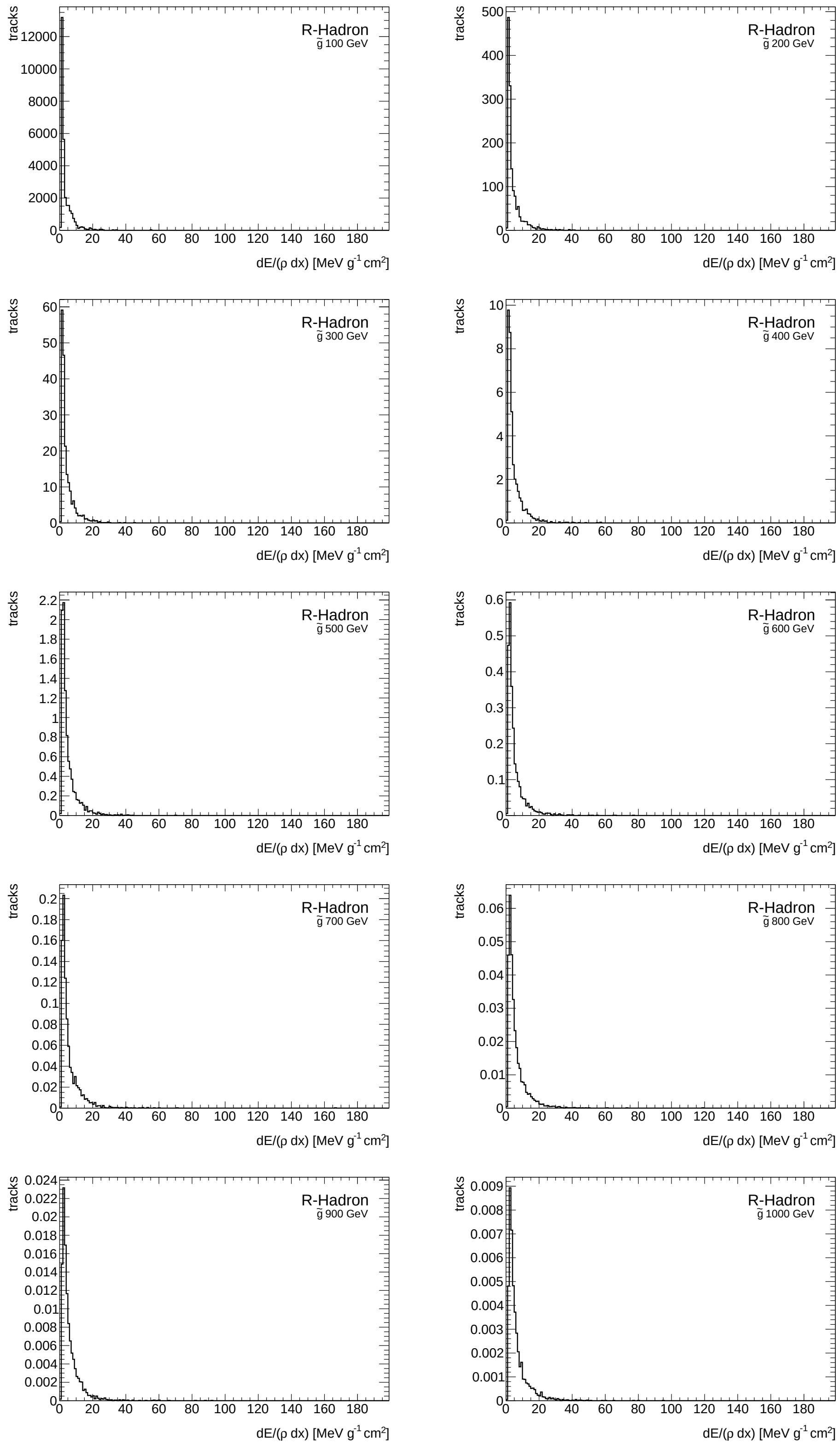

Figure B.11: Electromagnetic calorimeter barrel, layer 1, dE/dx for signal samples.

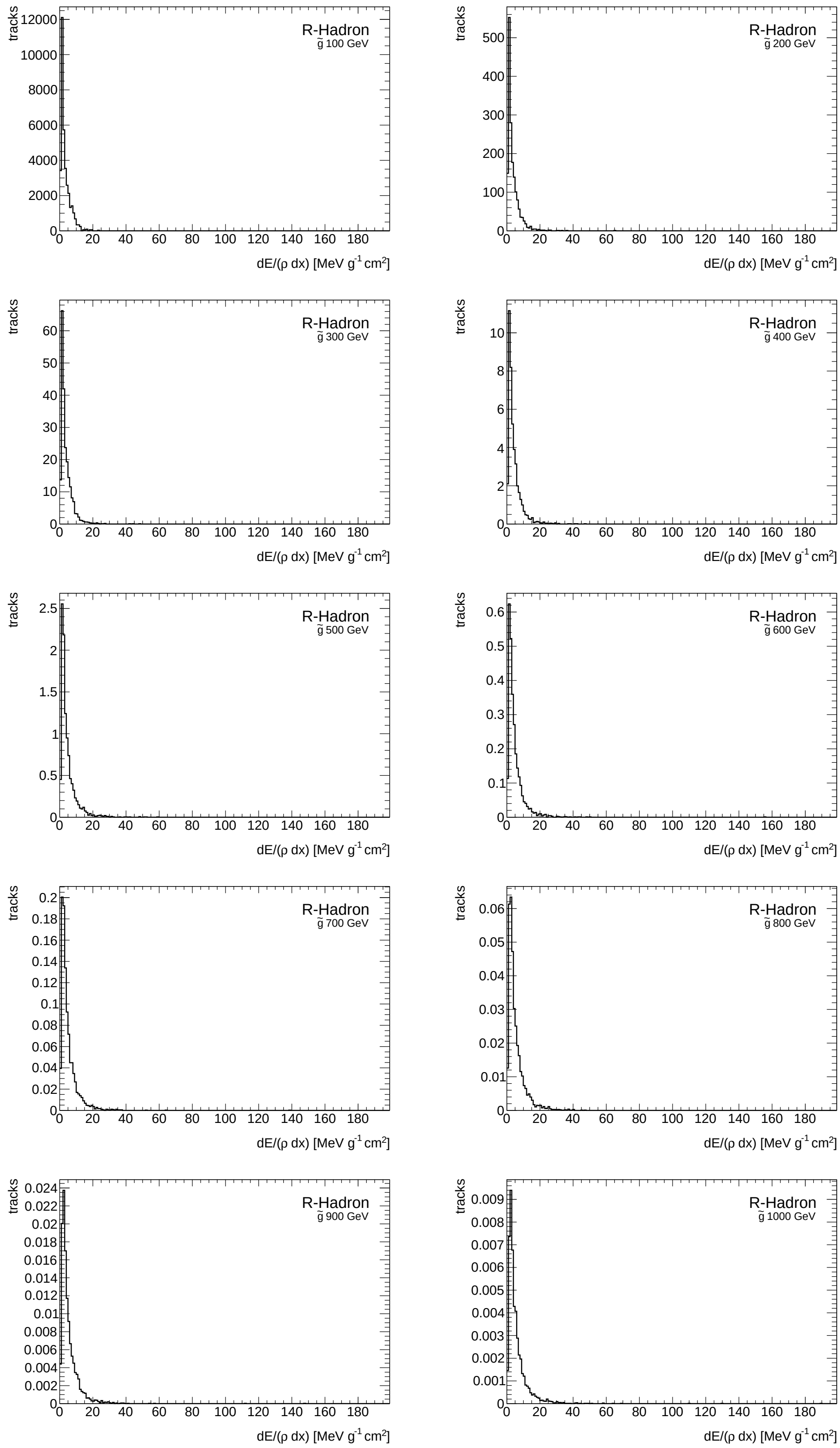

Figure B.12: Electromagnetic calorimeter barrel, layer 2, dE/dx for signal samples.

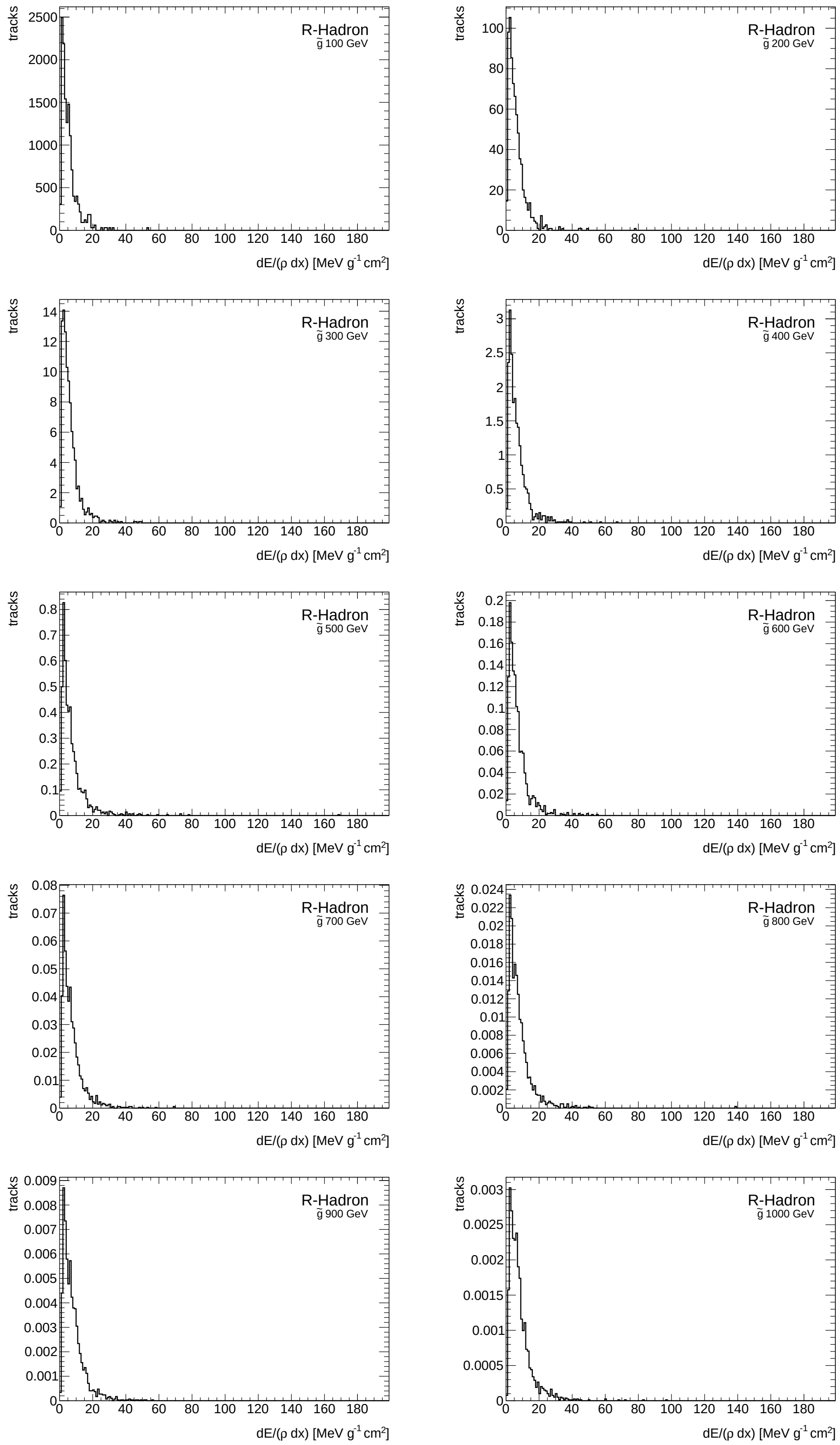

Figure B.13: Electromagnetic caloPlots barrel $|\eta| < 3.x$ layer 3, dE/dx for signal samples.

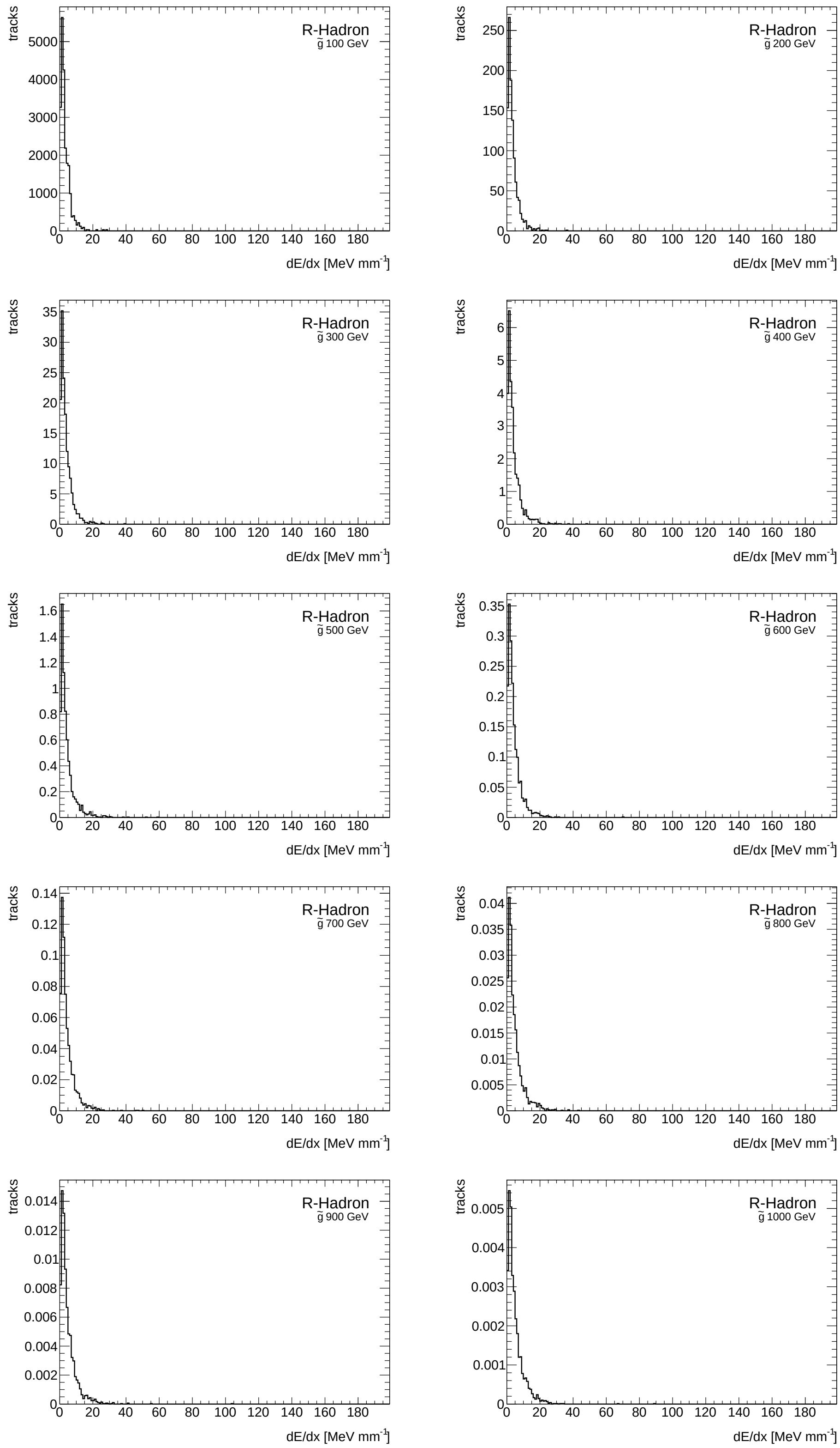

Figure B.14: Tile layer 1, dE/dx for signal samples.

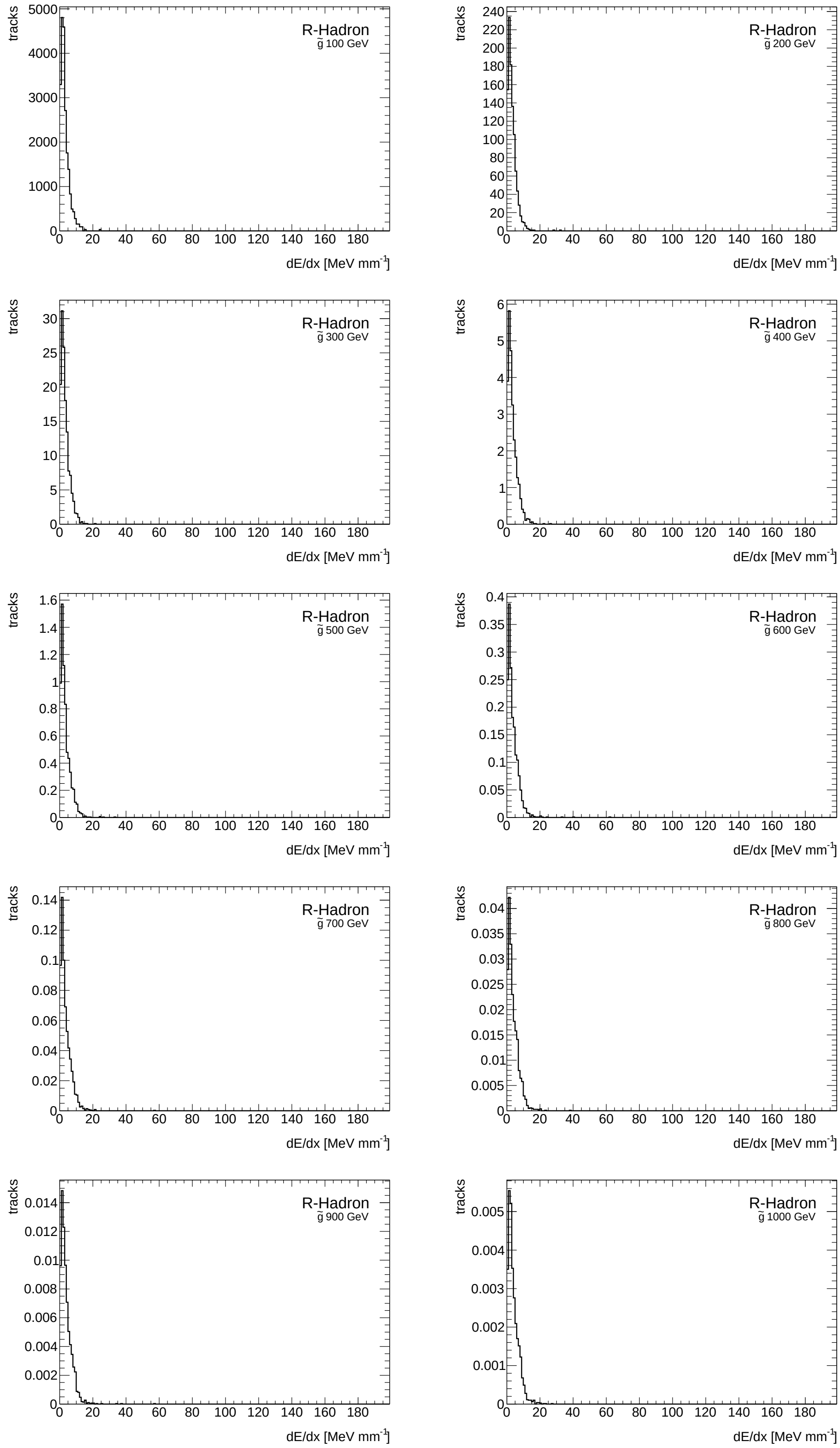

Figure B.15: Tile layer 2, dE/dx for signal samples.

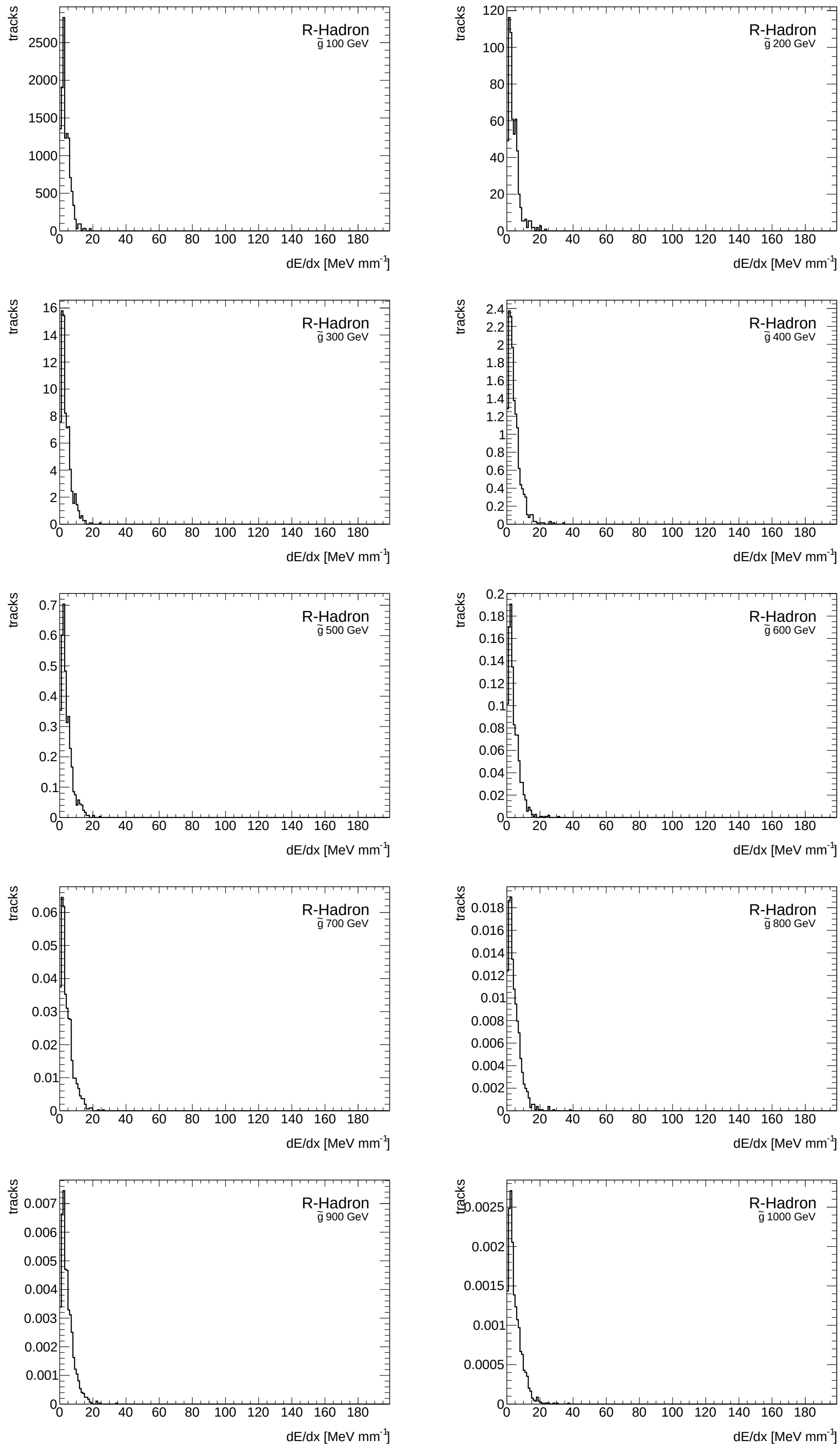

Figure B.16: Tile layer 3, dE/dx for signal samples.

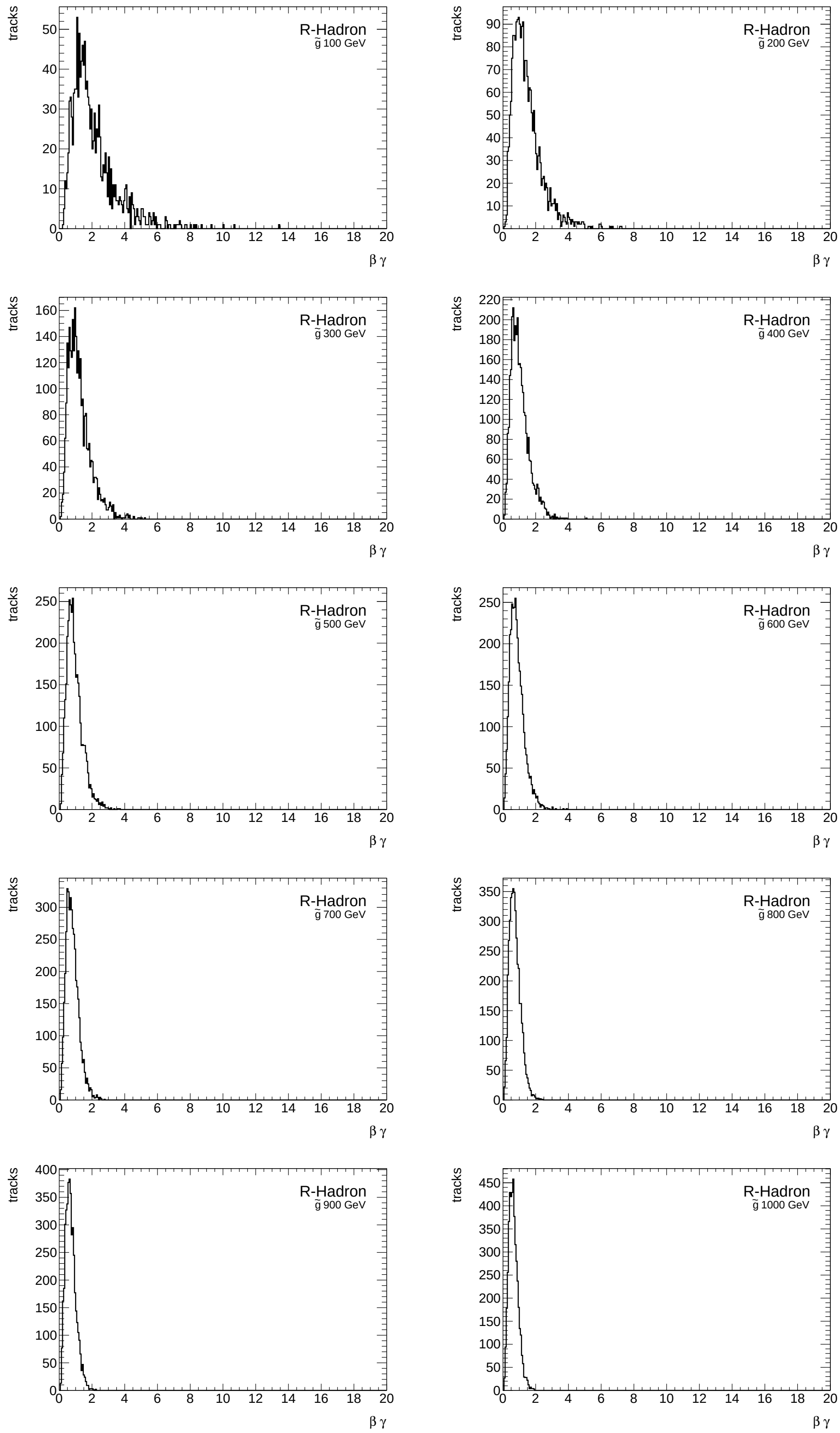

Figure B.17: True $\beta\gamma$

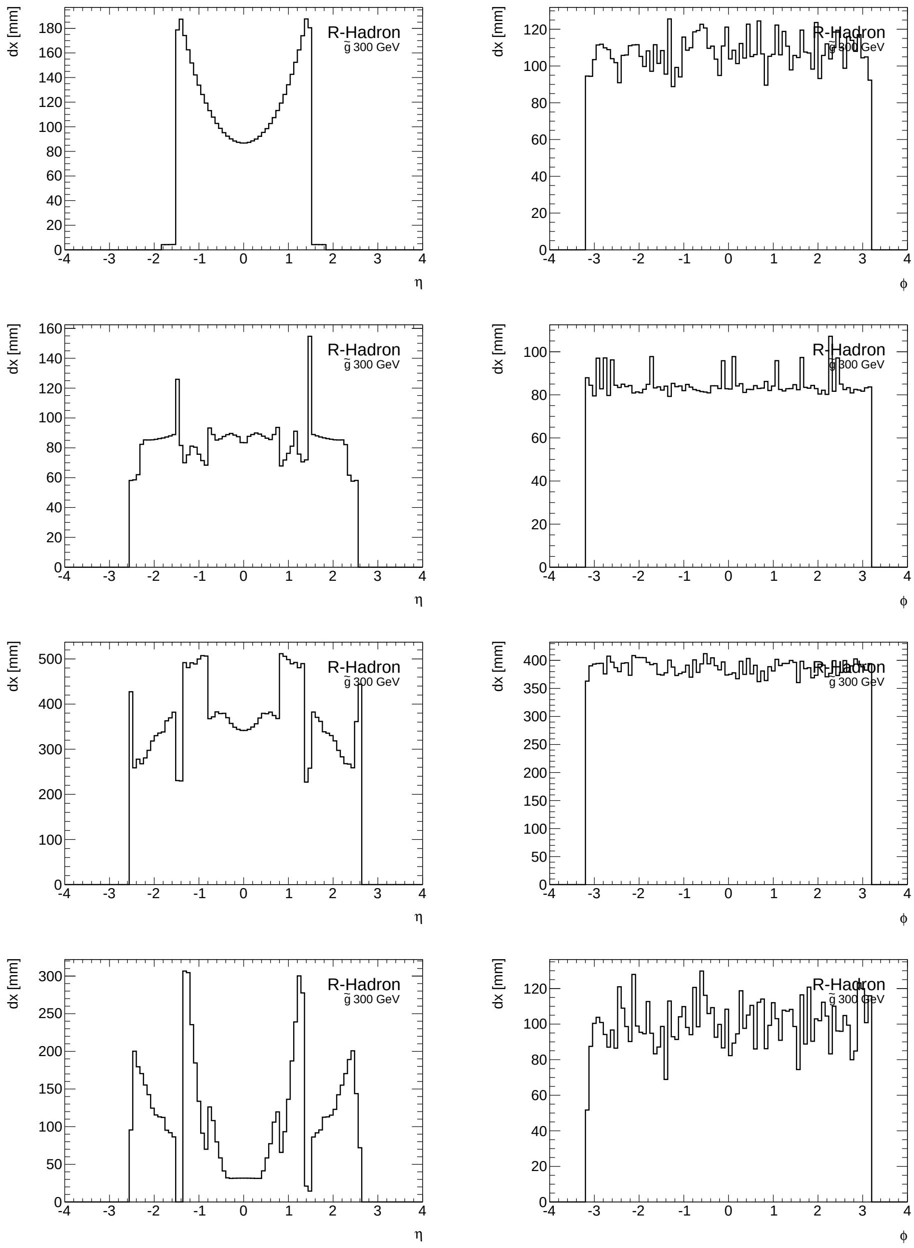

Figure B.18: Electromagnetic Calorimeter dl vs η

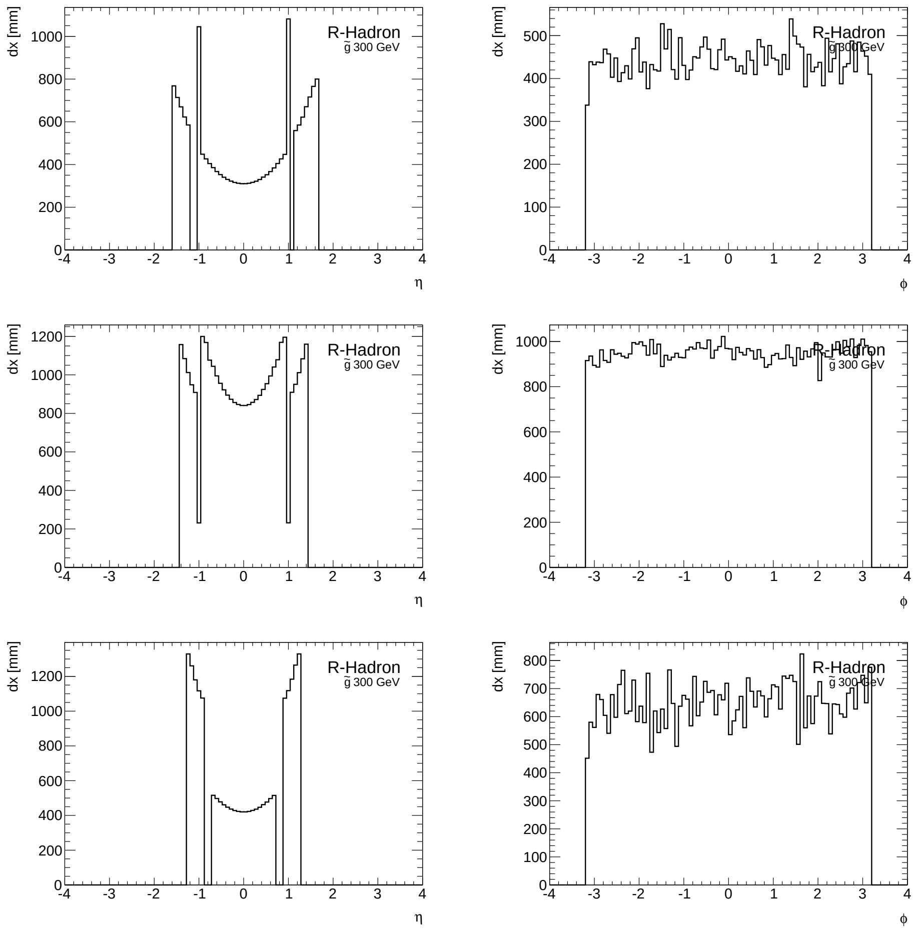

Figure B.19: Tile Calorimeter dl vs η

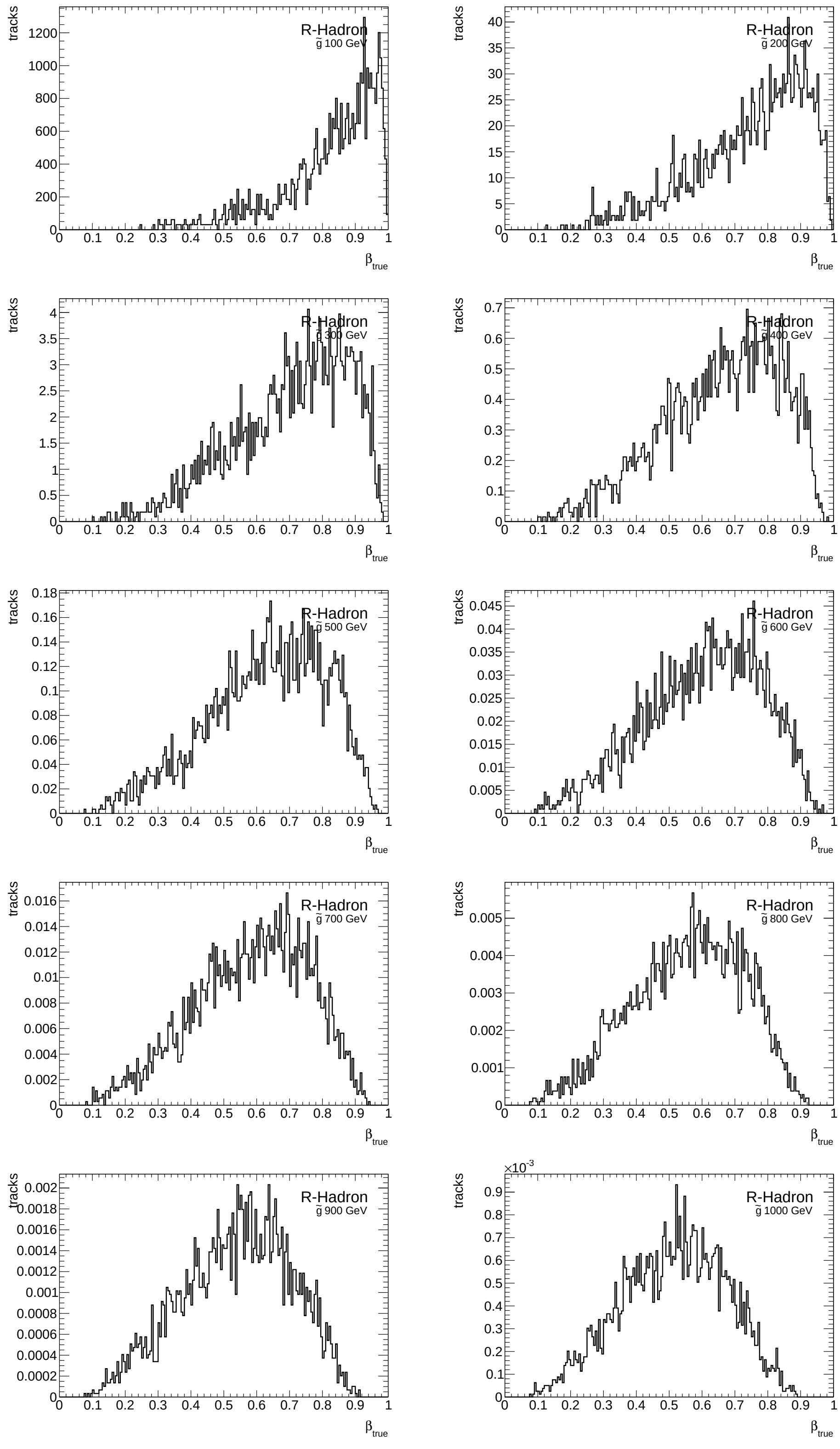

Figure B.20: True β

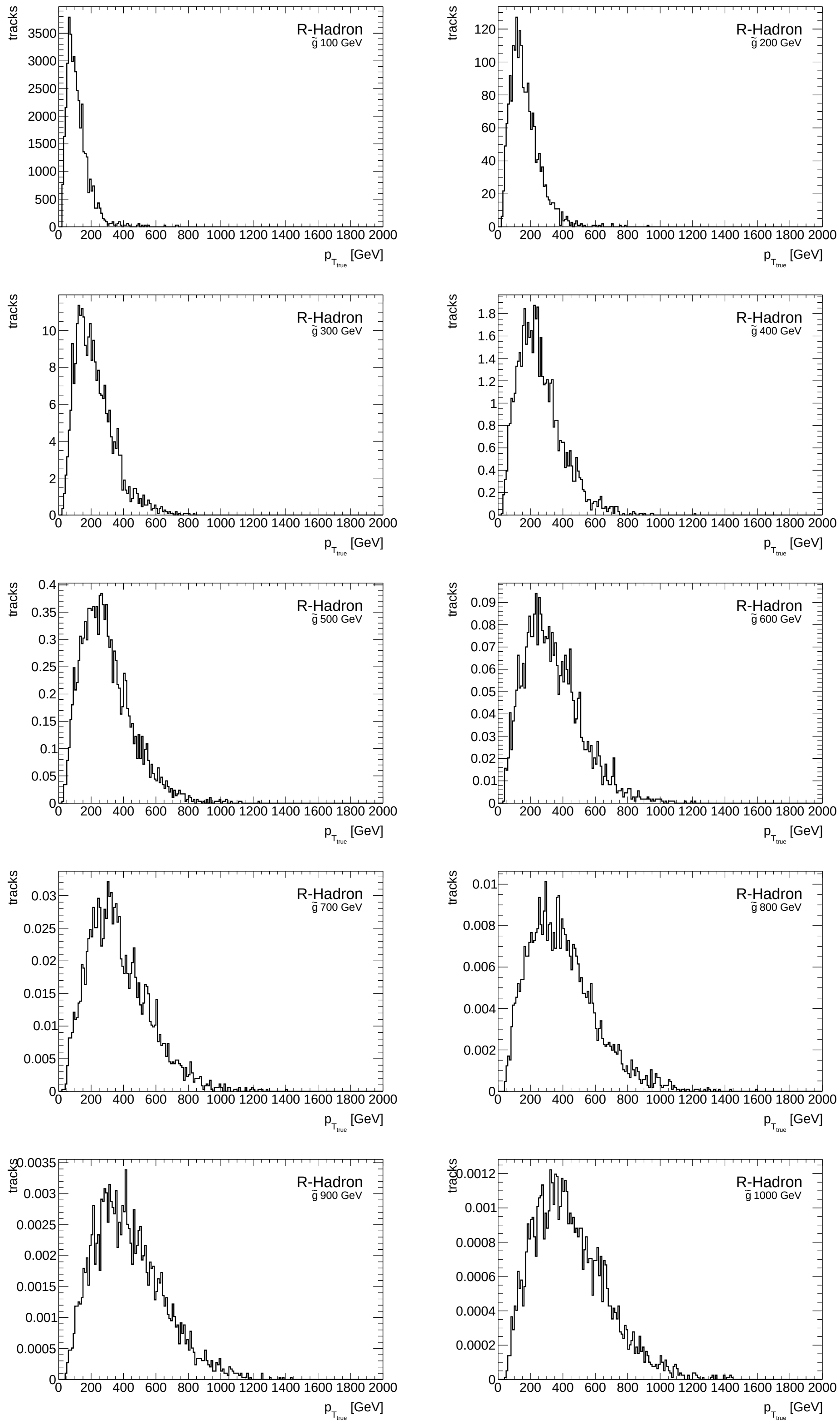

Figure B.21: True p_T

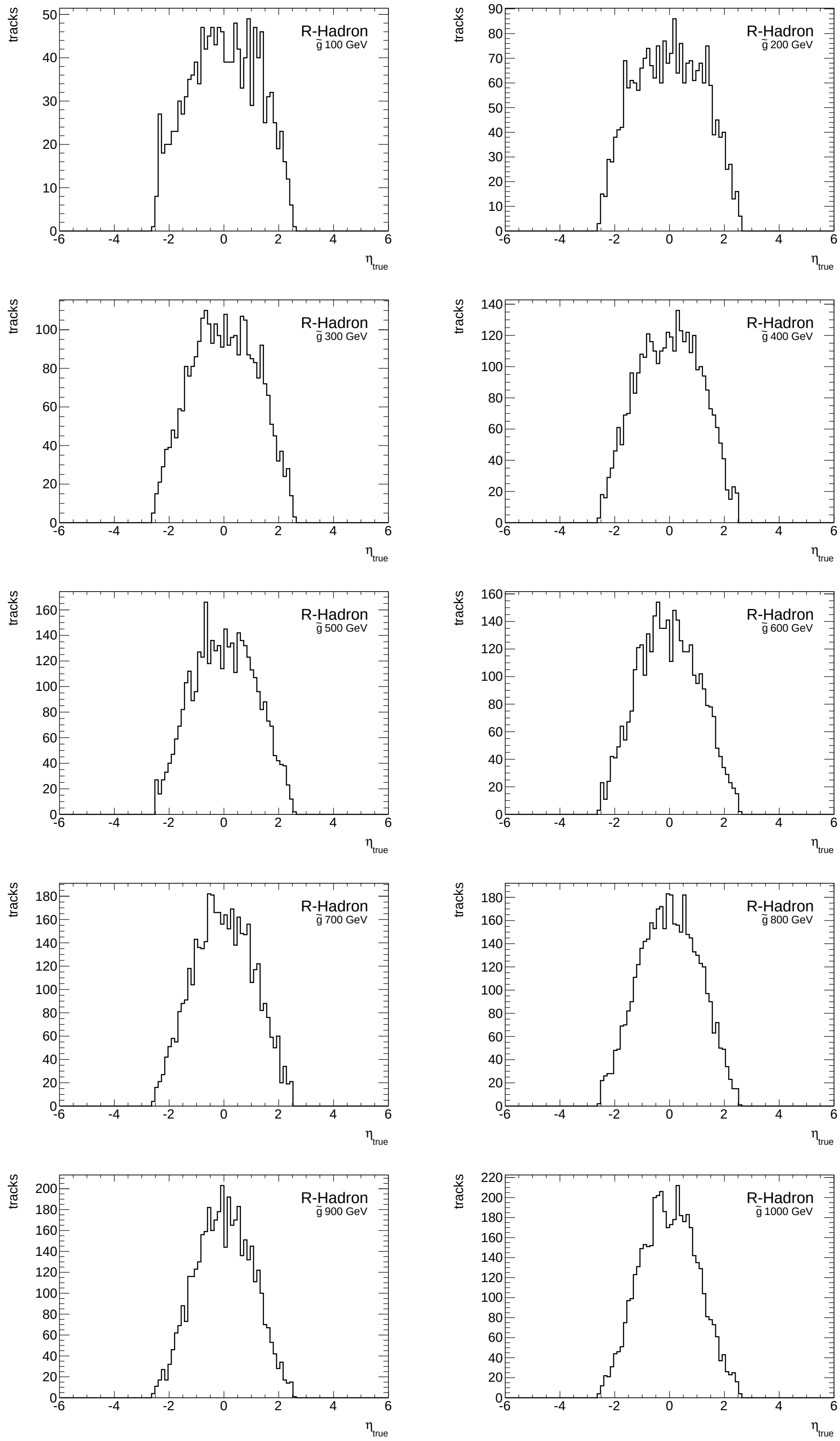

Figure B.22: True η

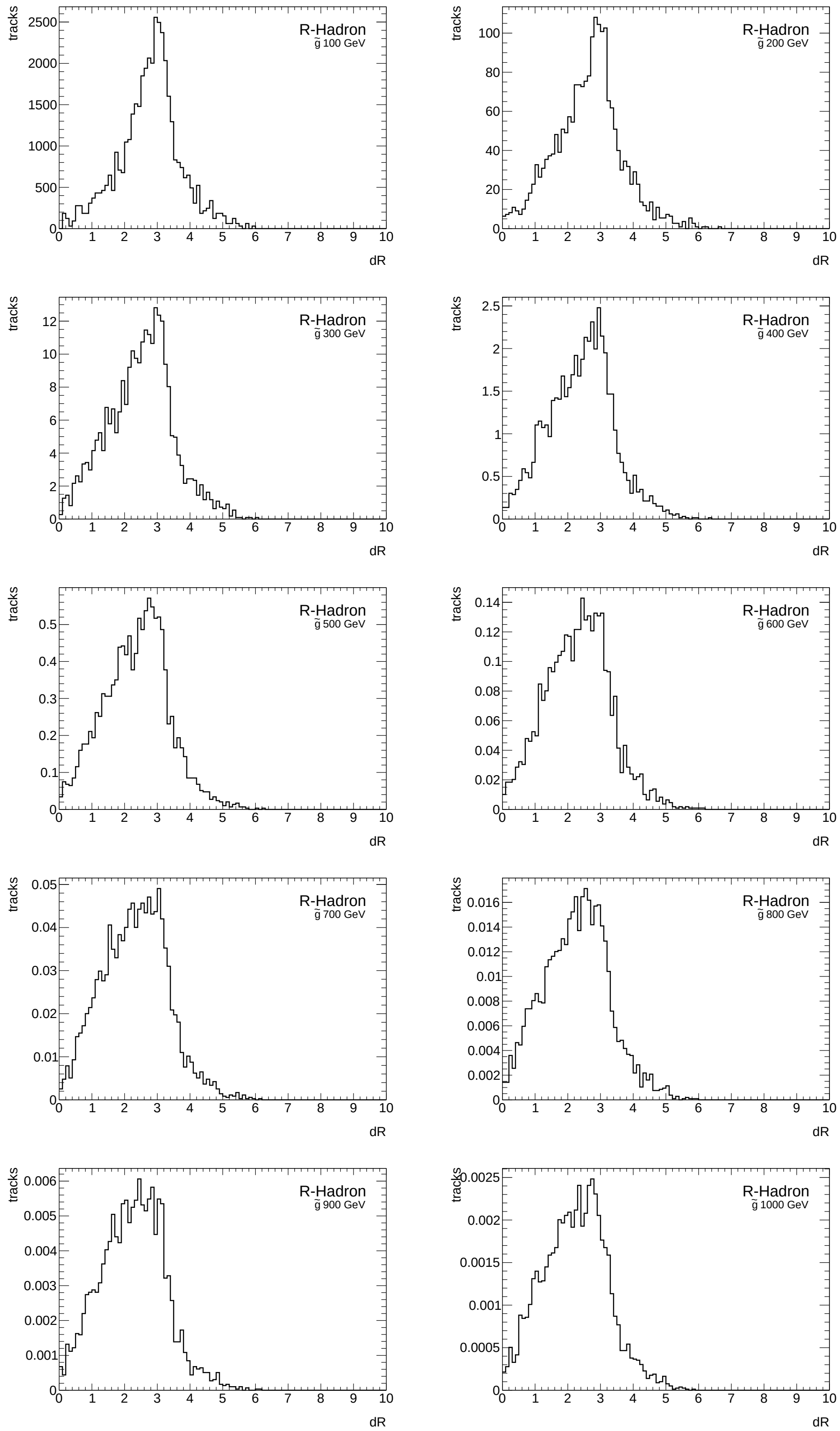

Figure B.23: Distance to nearest jet ΔR_{jet}

C

ATLAS datasets

Production of data samples in the ATLAS framework involves many layers of software, with frequent changes in versions. The data samples used in this analysis have been centrally produced by the SMP group, with the following settings:

- Pythia version: 6.4
- ATLAS Release: 15.6.12.7
- ALTAS Geometry version: GEO-10-00-01

It is possible to do an analysis within the ATLAS framework, but due to the large overhead involved, it is usually favourable to distil the data samples to a simple standalone format readable outside the ALTAS framework. These files are called ntuples, as they only contain simple data structures such as numbers and arrays of numbers, and no abstract data structures. The SMP group have codeveloped a tool for making these ntuples from ATLAS data formats, called SYNTMaker (Stockholm Yale Ntuple Maker). The calorimeter dE/dx algorithms are part of this tool, as they require access to ATLAS geometry data and track extrapolation mechanisms.

C.1 Datasets

15.6.12.7.reco.SYNTr158_SMP_skimmed

Monte carlo signal samples

mc10.114760.Pythia_R-Hadron_generic_gluino_100GeV
mc10.114761.Pythia_R-Hadron_generic_gluino_200GeV
mc10.114762.Pythia_R-Hadron_generic_gluino_300GeV
mc10.114763.Pythia_R-Hadron_generic_gluino_400GeV
mc10.114764.Pythia_R-Hadron_generic_gluino_500GeV
mc10.114765.Pythia_R-Hadron_generic_gluino_600GeV
mc10.114766.Pythia_R-Hadron_generic_gluino_700GeV
mc10.114767.Pythia_R-Hadron_generic_gluino_800GeV
mc10.114768.Pythia_R-Hadron_generic_gluino_900GeV
mc10.114769.Pythia_R-Hadron_generic_gluino_1000GeV

Data samples (Period C - E)

data10_7TeV.periodC.debugrec_hltacc.PhysCont.ESD.t0pro04_v01
data10_7TeV.periodC.physics_L1Calo.PhysCont.ESD.t0pro04_v01
data10_7TeV.periodC.physics_MuonswBeam.PhysCont.ESD.t0pro04_v01
data10_7TeV.periodD.debugrec_hltacc.PhysCont.ESD.t0pro04_v01
data10_7TeV.periodD.physics_L1Calo.PhysCont.ESD.t0pro04_v01
data10_7TeV.periodD.physics_MuonswBeam.PhysCont.ESD.t0pro04_v01
data10_7TeV.periodE1.debugrec_hltacc.PhysCont.ESD.t0pro04_v01
data10_7TeV.periodE1.physics_JetTauEtmiss.PhysCont.ESD.t0pro04_v01
data10_7TeV.periodE1.physics_Muons.PhysCont.ESD.t0pro04_v01
data10_7TeV.periodE2.debugrec_hltacc.PhysCont.ESD.t0pro04_v01
data10_7TeV.periodE2.physics_JetTauEtmiss.PhysCont.ESD.t0pro04_v01
data10_7TeV.periodE2.physics_Muons.PhysCont.ESD.t0pro04_v01
data10_7TeV.periodE3.debugrec_hltacc.PhysCont.ESD.t0pro04_v01
data10_7TeV.periodE3.physics_JetTauEtmiss.PhysCont.ESD.t0pro04_v01
data10_7TeV.periodE3.physics_Muons.PhysCont.ESD.t0pro04_v01
data10_7TeV.periodE4.debugrec_hltacc.PhysCont.ESD.t0pro04_v01
data10_7TeV.periodE4.physics_JetTauEtmiss.PhysCont.ESD.t0pro04_v01
data10_7TeV.periodE4.physics_Muons.PhysCont.ESD.t0pro04_v01
data10_7TeV.periodE5.debugrec_hltacc.PhysCont.ESD.t0pro04_v01
data10_7TeV.periodE5.physics_JetTauEtmiss.PhysCont.ESD.t0pro04_v01
data10_7TeV.periodE5.physics_Muons.PhysCont.ESD.t0pro04_v01
data10_7TeV.periodE6.debugrec_hltacc.PhysCont.ESD.t0pro04_v01
data10_7TeV.periodE6.physics_JetTauEtmiss.PhysCont.ESD.t0pro04_v01
data10_7TeV.periodE6.physics_Muons.PhysCont.ESD.t0pro04_v01
data10_7TeV.periodE7.debugrec_hltacc.PhysCont.ESD.t0pro04_v01
data10_7TeV.periodE7.physics_JetTauEtmiss.PhysCont.ESD.t0pro04_v01
data10_7TeV.periodE7.physics_Muons.PhysCont.ESD.t0pro04_v01

Background samples

```
mc09_7TeV.105009.J0_pythia_jetjet.recon.ESD.e468_s766_s767_r1303
mc09_7TeV.105010.J1_pythia_jetjet.recon.ESD.e468_s766_s767_r1303
mc09_7TeV.105011.J2_pythia_jetjet.recon.ESD.e468_s766_s767_r1303
mc09_7TeV.105012.J3_pythia_jetjet.recon.ESD.e468_s766_s767_r1303
mc09_7TeV.105013.J4_pythia_jetjet.recon.ESD.e468_s766_s767_r1303
mc09_7TeV.105014.J5_pythia_jetjet.recon.ESD.e468_s766_s767_r1303
mc09_7TeV.105015.J6_pythia_jetjet.recon.ESD.e468_s766_s767_r1303
mc09_7TeV.105200.T1_McAtNlo_Jimmy.recon.ESD.e510_s765_s767_r1302
mc09_7TeV.106022.PythiaWtaunu_1Lepton.recon.ESD.e468_s765_s767_r1302
mc09_7TeV.106044.PythiaWmunu_no_filter.recon.ESD.e468_s765_s767_r1302
mc09_7TeV.106047.PythiaZmumu_no_filter.recon.ESD.e468_s765_s767_r1302
mc09_7TeV.106052.PythiaZtautau.recon.ESD.e468_s765_s767_r1302
mc09_7TeV.106418.Pythia_R-Hadron1_gluino_300GeV.recon.ESD.e532_s810_s767_r1310
mc09_7TeV.106419.Pythia_R-Hadron2_gluino_600GeV.recon.ESD.e540_s815_s767_r1311
mc09_7TeV.108340.st_tchan_enu_McAtNlo_Jimmy.recon.ESD.e508_s765_s767_r1302
mc09_7TeV.108341.st_tchan_munu_McAtNlo_Jimmy.recon.ESD.e508_s765_s767_r1302
mc09_7TeV.108342.st_tchan_taunu_McAtNlo_Jimmy.recon.ESD.e508_s765_s767_r1302
mc09_7TeV.108343.st_schan_enu_McAtNlo_Jimmy.recon.ESD.e534_s765_s767_r1302
mc09_7TeV.108344.st_schan_munu_McAtNlo_Jimmy.recon.ESD.e534_s765_s767_r1302
mc09_7TeV.108345.st_schan_taunu_McAtNlo_Jimmy.recon.ESD.e534_s765_s767_r1302
mc09_7TeV.108346.st_Wt_McAtNlo_Jimmy.recon.ESD.e508_s765_s767_r1302
```

C.2 Pythia setup

```
# pT cut at 18 GeV
pysubs ckin 3 18.
# Old shower/multiple-interaction model
# (new model is not compatible with R-hadron fragmentation)
pypars mstp 81 1
# Set longitudinal fragmentation function to Pythia default
pydat1 mstj 11 4
# General MSSM simulation
pymssm imss 1 1
# Tell Pythia that rmss 3 below should be interpreted as the gluino pole mass
pymssm imss 3 1
# Set stop, sbottom and stau masses and mixing by hand (26-28 for mixing not set!)
pymssm imss 5 1

pymssm rmss 1 4000.0     # Photino mass
pymssm rmss 2 4000.0     # Wino/Zino mass
pymssm rmss 7 4000.0     # Right slepton mass
pymssm rmss 8 4000.0     # Left squark mass
pymssm rmss 9 4000.0     # Right squark mass
pymssm rmss 10 4000.0    # stop2 mass
```

```
pymssm rmss 11 4000.0    # sbottom1 mass
pymssm rmss 12 4000.0    # stop1 mass
pymssm rmss 4 4000.0     # Higgsino mass parameter

# Turn off all processes
pysubs msel 0

# Turn off master switch for fragmentation and decay
pypars mstp 111 0
pyinit pylistf 3
pystat 2

pymssm rmss 3 "mass of gluino".0    # gluino pole mass
pysubs msub 244 1           # Turn on gg -> ~g~g
```

Bibliography

[1] G Aad, N Groot, F Filthaut, and D Froidevaux. The atlas experiment at the cern large hadron collider. *http://hdl. handle. net/ . . .*, Jan 2008.

[2] Nima Arkani-Hamed, Savas Dimopoulos, and Gia Dvali. The hierarchy problem and new dimensions at a millimeter. *arXiv*, hep-ph, Mar 1998.

[3] Yannick Arnoud. 95% confidence level limits, Jan 2011. http://lpsc.in2p3.fr/d0/documentation/CL.html.

[4] M Aurousseau, R Caputo, J Hobbs, M Kado, S Laplace, D Tsybychev, J-B de Vivie de Regie, and A Yurkewicz. Uniformity of the response of the atlas electromagnetic calorimeter using cosmic muon signals. Technical Report ATL-COM-LARG-2009-052, CERN, Geneva, Oct 2009.

[5] M Baak, C Guyot, M Hauschild, R Hawkings, B Heinemann, A Höcker, M Martínez-Pérez, D Malon, P Onyisi, and E Torrence. Data quality status flags and good run lists for physics analysis in atlas. Technical Report ATL-COM-GEN-2009-015, CERN, Geneva, Mar 2009.

[6] W. Beenakker, R. Hopker, and M. Spira. PROSPINO (version 2.0). *Arxiv preprint hep-ph/9611232*.

[7] Christopher M Bishop. Pattern recognition and machine learning. pages 1–749, Apr 2007.

[8] D Casadei, T Cornelissen, C Gay, C Gemme, S Hellman, MD Joergensen, E Klinkby, C Marino, R Mackeprang, P Mermod, W Mills, D Milstead, C Ohm, H Ogren, T Petersen, A Pinder, L Rossi, and Zieminska D. Search for stable hadronising squarks and gluinos at the atlas experiment at the lhc. Technical Report ATL-COM-PHYS-2010-1065, CERN, Geneva, Dec 2010.

[9] S Coleman. . . . All possible symmetries of the s matrix. *Physical Review*, Jan 1967.

[10] The ATLAS Collaboration. Drift time measurement in the atlas liquid argon electromagnetic calorimeter using cosmic muons. *The European Physical Journal C - Particles and Fields*, 70:755–785, 2010. 10.1140/epjc/s10052-010-1403-6.

[11] The ATLAS Collaboration. Search for stable hadronising squarks and gluinos with the atlas experiment at the lhc. *Physics Letters B*, 701(1):1 – 19, 2011.

[12] The CMS Collaboration. Search for heavy stable charged particles in pp collisions at $\sqrt{s} = 7$ TeV. *Journal of High Energy Physics*. Submitted.

[13] Glen Cowan. *Statistical Data Analysis*. Oxford University Press, Oxford, 1998.

[14] A Einstein. On the electrodynamics of moving bodies. *Annalen der Physik*, Jan 1905.

[15] S. Agostinelli et. al. G4–a simulation toolkit. *Nuclear Instruments and Methods in Physics Research Section A: Accelerators, Spectrometers, Detectors and Associated Equipment*, 506(3):250 – 303, 2003.

[16] K. Nakamura et al. (Particle Data Group). The review of particle physics. *J. Phys. G*, 37, 2010.

[17] Lyndon Evans and Philip Bryant. Lhc machine. *Journal of Instrumentation*, 3(08):S08001, 2008.

[18] M Fairbairn, A. C Kraan, D. A Milstead, T Sjostrand, P Skands, and T Sloan. Stable massive particles at colliders. *arXiv*, hep-ph, Jan 2006.

[19] European Organization for Nuclear Research (Ginebra). *ATLAS detector and physics performance: Technical Design Report*. CERN, 1999.

[20] Gordon Fraser. The particle century. page 232, Jan 1998.

[21] Dan Green. *The Physics of Particle Detectors*. Cambridge University Press, 2000.

[22] Dan Green. *High P_T Physics at Hadron Colliders*. Cambridge University Press, 2005.

[23] S Hellman, M Johansen, R Mackeprang, P Mermod, D Milstead, C Ohm, and A Solodkov. Measuring time-of-flight and identifying exotic stable massive particles with the atlas tile calorimeter. Technical Report ATL-TILECAL-INT-2010-006, CERN, Geneva, Sep 2010.

[24] JoAnne L Hewett, Ben Lillie, Manuel Masip, and Thomas G Rizzo. Signatures of long-lived gluinos in split supersymmetry. *arXiv*, hep-ph, Aug 2004.

[25] F. James. *Statistical methods in experimental physics*. World Scientific Pub Co Inc, 2006.

[26] D. I Kazakov. Beyond the standard model (in search of supersymmetry). *arXiv*, hep-ph, Dec 2000.

[27] J. Kepler and W.H. Donahue. *New astronomy*. Cambridge University Press, 1992.

[28] Aafke Christine Kraan. *Interactions and Detection of R-Hadrons*. PhD thesis, Copenhagen University, Niels Bohr Institute, Nov 2004.

[29] B Lenzi, R Nicolaidou, and S Hassani. Trackincalotools: A package for measuring muon energy loss and calorimetric isolation in atlas. *Journal of Physics: Conference Series*, 219(3):032049, 2010.

[30] Bruno Lenzi, Claude Guyot, and Rosy Nicolaidou. *Search for the Higgs boson decaying to four leptons in the ATLAS detector at LHC and studies of muon isolation and energy loss. oai:cds.cern.ch:1301521*. PhD thesis, France, Université Paris Sud Orsay, France, 2010. Presented on 17 Sep 2010.

[31] Louis Lyons, Duncan Gibaut, and Peter Clifford. How to combine correlated estimates of a single physical quantity. *Nuclear Instruments and Methods in Physics Research Section A: Accelerators, Spectrometers, Detectors and Associated Equipment*, 270(1):110 – 117, 1988.

[32] R. Mackeprang and D. Milstead. An updated description of heavy-hadron interactions in geant-4. *The European Physical Journal C - Particles and Fields*, 66:493–501, 2010. 10.1140/epjc/s10052-010-1262-1.

[33] Rasmus Mackeprang. *Stable Heavy Hadrons in ATLAS*. PhD thesis, Niels Bohr Institute, 2007.

[34] AD Martin, WJ Stirling, RS Thorne, and G. Watt. Parton distributions for the LHC. *The European Physical Journal C-Particles and Fields*, 63(2):189–285, 2009.

[35] J Maxwell. A dynamical theory of the electromagnetic field. *Philosophical Transactions of the Royal Society of . . .*, Jan 1865.

[36] P.M. Nadolsky, HL Lai, QH Cao, J. Huston, J. Pumplin, D. Stump, WK Tung, and CP Yuan. CTEQ Collaboration. *Phys. Rev. D*, 78:013004, 2008.

[37] Sir Isaac Newton, Thomas Leseur, and François Jacquier. Philosophiæ naturalis principia mathematica, volumes 1-2. Jan 1822.

[38] Roger Penrose. The road to reality: A complete guide to the laws of the universe. page 1099, Jan 2007.

[39] Karl Popper. *The Logic of Scientific Discovery*. Routledge publishers, London, 1959.

[40] AL Read. Modified frequentist analysis of search results (The CLs method), 2000. *CERN report*, 5, 2000.

[41] V Rossetti. Commissioning of the atlas tile hadronic calorimeter with cosmic muons, single beams and first collisions. May 2010.

[42] Torbjorn Sjostrand, Stephen Mrenna, and Peter Skands. Pythia 6.4 physics and manual. *Journal of High Energy Physics*, 2006(05):026, 2006.

[43] S Weinberg. A model of leptons. *Phys. Rev. Lett.*, Jan 1967.

[44] Wikipedia. Crystal ball function — wikipedia, the free encyclopedia, 2010. [Online; accessed 14-January-2011].